DYNAMIC MODELING AND CONTROL OF TRANSCRITICAL VAPOR COMPRESSION SYSTEM FOR BATTERY ELECTRIC VEHICLE THERMAL MANAGEMENT

BY

SARAH GRACE GARROW

THESIS

Submitted in partial fulfillment of the requirements
for the degree of Master of Science in Mechanical Engineering
in the Graduate College of the
University of Illinois at Urbana-Champaign, 2018

Urbana, Illinois

Adviser:

Professor Andrew Alleyne

Abstract

Electrification is an increasing trend among vehicle systems such as aircrafts, heavy machinery, and civilian transportation. Battery electric vehicles (BEVs) are one such development that use a battery pack to generate electrical energy used to propel the vehicle and power its auxiliaries. However, the battery pack also generates thermal energy as a byproduct which affects the electrical performance of the battery pack. The inherent coupling between electrical and thermal performance creates a challenge in design and control of these complex systems. Furthermore, phase-out of common refrigerants drives interest in CO_2 refrigerant, an environmentally friendly and safe alternative. However, these vapor compression systems operate transcritical, thus requiring novel control techniques. This thesis develops a framework for architecture and control design of BEV subsystems. The foundation of this process is the development of multi-domain models.

Models for the transcritical vapor compression system and the vehicle cabin are derived from a first principles analysis. A model for a battery pack is derived from an equivalent circuit electrical model and a conservation of energy thermal model. All of the models capture dynamic, nonlinear behaviors important for control development and understanding of coupling between variables. Additionally, the models are scalable and able to be parameterized in order to represent many variations of system architectures.

An air-cooled cabin and air-cooled battery pack configuration is demonstrated in open-loop and closed-loop simulations. For closed loop simulation, a model predictive controller (MPC) is compared to baseline decentralized, proportional-integral controllers. The model predictive control makes control decisions based on the minimization of a cost function that weights the regulation of specific variables (such as temperature of the battery pack and cabin) and power consumption of the actuators. It will be shown that the MPC, in the face of disturbances, is able to maintain outputs within their bounds while consuming less energy than baseline controllers.

Acknowledgements

I would like to first and foremost thank my advisor, Dr. Andrew Alleyne for his support and guidance. Beyond research, he offered encouragement and perspective at times when I was struggling with career decisions, and showed an invested interest in my general happiness and well-being. I am grateful to have been mentored by such an upstanding role model.

Second, I am grateful for the outstanding culture of inclusion that I experienced in my lab group. To the senior members, Justin, Matt, Herschel, and Bryan, thank you for your encouragement and for always being available to help and teach. To Nate, Oyuna, Pamela, Spencer K., Ashley and Malia, thank you for your moral and academic support, and positive energy. A special appreciation goes to Malia for all of the extra things she did to encourage an inclusive, healthy, and fun lab dynamic, and for being a good friend. To Spencer I., Sunny, Chris and Donald, thank you for being balanced individuals, showing determination and inquisitiveness while remaining relaxed and light-hearted.

Third, I would like to thank my family. My parents and brother have always been my motivators. They show passion in the work that they do and continually encourage me to pursue the things that I enjoy. Their love and support has been tremendous.

Next, I want to thank my friends Sunny, Nicole and Kelsey for their emotional support and consolation as I worked through self-doubts, imposter syndrome and perfectionism. Graduate school was challenging in many ways, but they were always by my side to offer advice and provide a laugh to help me through.

Finally, I would like to acknowledge the financial support from the University of Illinois at Urbana-Champaign Graduate College Fellowship Program, and the Engineering Research Center for Power Optimization of Electro-Thermal Systems (POETS) with cooperative agreement EEC-1449548. Their support has allowed me to pursue research that inspires me and has meaningful value.

Dedicated to Mom, Dad, Nate, and Amber

Table of Contents

List of Figures

List of Tables

Nomenclature

Symbol	Description	Units
A	Area	m^2
c	Drag/rolling resistance	-
C	Thermal capacitance	J/K
$\bar{C}$	Electrical capacitance	F
c_p	Specific heat	kJ/(kg K)
d	Disturbance	
F	Force	N
g	Gravity	m/s^2
h	Enthalpy	kJ/kg
$\bar{I}$	Current	A
k	Thermal conductivity	W/(m K)
L	Length	m
$\dot{m}$	Mass flow rate	kg/s
n	Number of Volumes	-
N_p	Prediction Horizon	-
$\bar{N}_p$	Number of cells in parallel	-
$\bar{N}_s$	Number of cells in series	-
N_u	Control horizon	-
p	Perimeter	m
P	Pressure	kPa
$\bar{P}$	Power	W
q	Specific cooling capacity	kJ/kg
q''	Heat flux	W/m^2
Q	Heat transfer rate	W

R	Thermal resistance	K/W
$\bar{R}$	Electrical resistance	Ohm
SOC	State of Charge	-
t	Time	s
T	Temperature	°C
T_s	Sample time	s
u_{fan}^{batt}	Battery fan command	%
u_{fan}^{evap}	Evaporator fan command	%
u_v	Valve command	%
v	Velocity	m/s
V	Volume	m^3
V_{ocv}	Open-circuit voltage	V
$\bar{V}$	Voltage	V
w	Specific work	kJ/kg
x	Position	m
z	Aperture	%
$\tilde{\alpha}$	Thermal diffusivity	m^2/s
α	Heat transfer coefficient	$W/(m^2\ K)$
$\bar{\alpha}$	Absorptivity	-
$\bar{\beta}$	Cell capacity	Ah
ζ	Normalized HX zone length	-
ε	Emissivity	-
γ	Radiative heat loss [0 1]	-
$\bar{\gamma}$	Mean void fraction	-
η_k	Isentropic efficiency	-
η_v	Volumetric efficiency	-
θ	Angle	degrees
ρ	Density	kg/m^3
σ	Stefan-Boltzmann constant	$W/(m^2K^4)$

τ	Time constant	s^{-1}
$\bar{\tau}$	Transmittance	-
ω	Rotational velocity	RPM
ω_k	Compressor speed	RPM

Subscript	**Description**
a	Air
batt	Battery
c	Core
cab	Cabin
comp	Compressor
cr	Critical
cs	Cross-sectional
cv	Control volume
d	Discrete
ent	Entropic
evap	Evaporator
ext	External
f	Saturated liquid
fl	Fluid
gc	Gas Cooler
gen	Generated
HP	High pressure
i	Control volume index
in	Into control volume
int	Internal/interior
LP	Low pressure
m	Mean
out	Out of control volume
r	Refrigerant
s	Saturation

SC	Sub-cooled
sh	Shell
SH	Superheated
sp	Setpoint
surf	Surface
TP	Two-phase zone
u	Convective
v	Saturated vapor
w	Wall

Chapter 1 Introduction

This thesis investigates the impact of multi-domain modeling of battery electric vehicle (BEV) thermal and electrical systems on architecture and control design to improve vehicle performance. Electrification of vehicle systems is an increasing trend and traditional design approaches are no longer suitable for achieving vehicle performance and battery longevity requirements. Traditional approaches design electrical systems first and then sequentially a thermal management system. This sequential approach results in mismanaged thermal behavior, thereby causing inefficiencies and failure of systems. Therefore, it is important to integrate the electrical and thermal system design to understand the coupling between the two domains and to develop robust controllers for thermal management. This thesis will explore how multiple subsystems of a BEV can be modeled with compatible frameworks such that they can be simulated together to capture the dominant system dynamics. Additionally, the performance of a decentralized control approach for thermal management of two significant loads in a BEV is compared to a centralized model predictive control (MPC) approach. It will be shown that the MPC controller can achieve thermal regulation with respect to disturbances, while also consuming less power.

1.1 Motivation

Green-house gas emissions have been shown to impact climate, ecosystems and society in many ways including more severe weather patterns, increased ocean acidity, and changes in crop growing seasons [1]. The Center for Climate and Energy Solutions provided that in 2008 the transportation sector contributed 27% of US greenhouse gas emissions (90% of which is CO_2). Light-, medium- and heavy-duty vehicles are the largest contributor to these emissions, generating 78% of the total transportation sectors' CO_2 emissions [2]. The U.S. Environmental Protection

Agency regulations are requiring multi-phase improvements in vehicle fuel economy in order to reduce fossil fuel consumption, reduce green-house gas emissions and reduce fuel prices [3]. This has resulted in the transition from internal combustion engine vehicles to hybrid electric vehicles and to battery electric vehicles. Furthermore, many governments are incentivizing battery electric vehicles more than hybrids with tax waivers, subsidies, rebates, etc. to further push for zero-emission vehicles [4]. Due to these governmental regulations and incentives, the battery electric vehicle market has been growing faster than the hybrid electric vehicle market, as supported by Figure 1.2. In fact, the battery electric vehicle car stock is increasing at an increasing rate in the U.S. and globally. This thesis will focus on battery electric vehicles because they are foreseen to dominate the electric vehicle market.

Additionally, refrigerants used in vapor compression cycles for air conditioning and thermal management contribute to greenhouse gas emissions. Hydrofluorocarbon R134a is a common vehicle refrigerant, but has high global warming potential (GWP). GWP is a relative measure of the amount of heat trapped by a gas in the atmosphere, compared to carbon dioxide. Since the concentration of different gases decay at different rates, the measure of GWP is in terms of time span (commonly a 100-year time span is considered). R134a has a GWP of 1430 (factor by which it is more harmful than CO2) over 100 years. By 2021, R134a will not be permitted in newly produced vehicles in the U.S. [5]. CO_2 refrigerant (R744) is a strong candidate because its global warming potential is 1 (by definition) and it is safe, natural, economic and sustainable.

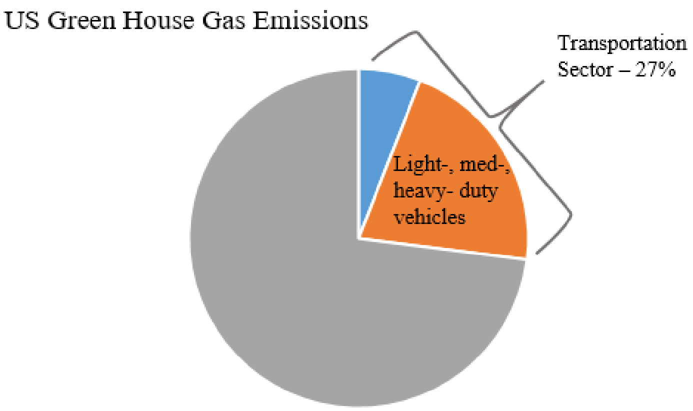

Figure 1.1 Portion of US green-house gas emissions generated by the transportation sector and the portion within that percentage that is generated by light-, medium, and heavy-duty vehicles

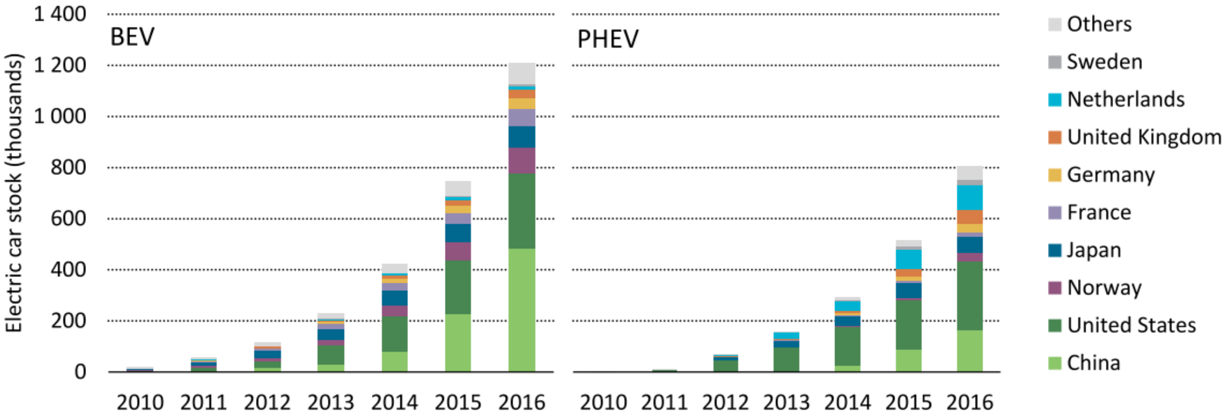

Figure 1.2 Battery electric vehicle and plug-in hybrid electric vehicle stock for 2010-2016 [4]. © OECD/IEA 2017 *Global EV Outlook 2017*, IEA Publishing, License: www.iea.org/t&c

1.1.1 BEV Range Challenges and Opportunities

Battery electric vehicle range (distance between charging) is an important performance metric for market acceptability. The range is impacted by two major factors: 1) the battery capacity, which limits its capable range, and 2) power consumption of auxiliaries. Battery chemistry and size constraints (i.e. dimensional and weight constraints) are examples of factors that limit the battery capacity. However, another significant variable that influences the available capacity is the operating temperature, which will be further described in the next section. Additionally, the available capacity for propulsion is reduced by the power consumption of auxiliary units. The heating, ventilation and air conditioning (HVAC) unit has the potential to consume the most and have a significant impact on range.

1.1.1.1 Battery Operating Temperature Range

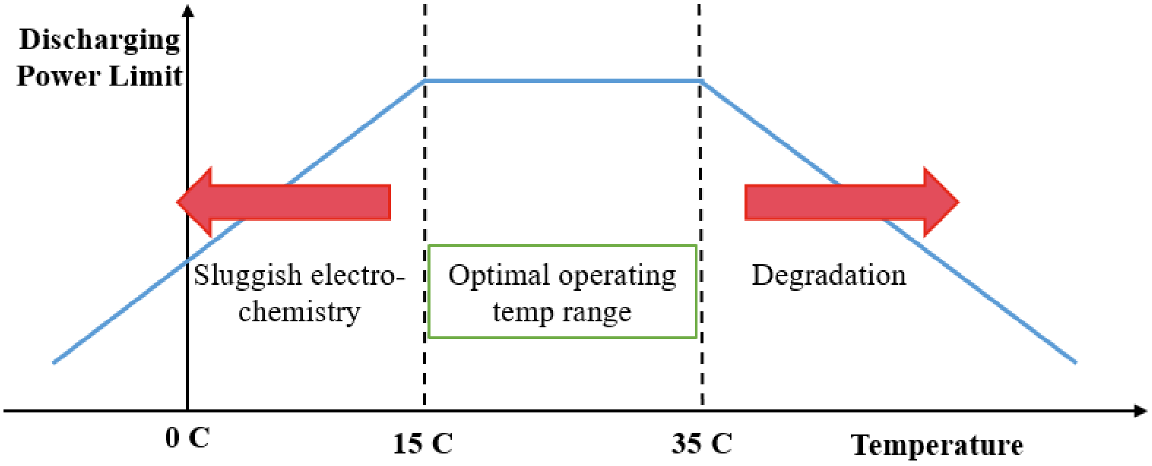

Figure 1.3 Effects of operating temperature on battery power limit during discharge of Li-Ion battery. Adapted from [6].

The performance and life of a battery pack is dependent on operating temperature. Figure 1.3 shows that the power limit of the battery during discharge is maximized between 15-35 C. Below this temperature range, the battery exhibits sluggish electro-chemistry due to the increase in internal resistance of each cell. The increase in internal resistance limits the battery power capability. Additionally, above 35 C, the battery experiences degradation that significantly affects the life of the battery. [6] compared battery power loss with respect to climate and showed that Phoenix (average temperature: 24 C), experiences approximately 50% power loss over 15 years, in contrast with Minneapolis (average temperature: 8 C) which experiences ~30% power loss over the same period. These temperature effects on capacity determine the frequency in which the user has to recharge their battery and replace their battery pack.

The main ageing mechanisms below 25 C are due to Lithium plating, when metallic Lithium forms on the negative electrode. Above 25 C, the dominant ageing mechanism is reactions between the electrode and electrolyte, leading to the formation of solid electrolyte interphase (SEI) layers, and dissolution from the cathodes [7]. References [7], [8] provide more detail about temperature dependent ageing mechanisms. From this evidence, it is clear that thermal management of the battery pack is essential in electric vehicles.

1.1.1.2 Power Consumption of Heating and Cooling

The HVAC unit consumes 1-5 kW of power, relative to traction motors that require 20-47 kW [9]. Furthermore, urban driving often entails frequent periods of idle in which the heating/cooling may be running continuously and discharging the battery even when the traction motor is not drawing current. Reference [10] investigated energy consumption with consideration to topography, infrastructure, traffic and climate and found that topography and climate have the greatest impact on energy consumption. Energy efficient HVAC systems would benefit the range of BEVs.

1.1.2 CO_2 Refrigerant Challenges and Opportunities

Due to the low critical temperature of CO_2 and high critical pressure, the vapor compression system will operate transcritical and at high pressures. The evaporator pressures are typically between 4-6,000 kPa and gas cooler pressure between 9-12,000 kPa. These pressures are 5-10 times greater than the operating pressure of an R134a system [11]. Therefore, the same components for an R134a system cannot be used for a CO_2 system because they are not designed to withstand that high pressure. However, CO_2 has comparatively greater volumetric refrigeration capacity, which provides the benefit of smaller VCS components. Although CO_2 refrigerant does not have the benefit of being a ‘drop-in’ refrigerant for existing R134a systems, the system components will be more compact, thus using less space in the vehicle.

Table 1.1 R-134a and R-744 refrigerant properties [11]

	R-134a	**R-744 (CO_2)**
GWP (-)	1430	1 (by definition)
Critical Pressure (MPa)	4.07	7.38
Critical Temperature (C)	101.1	31.1
Refrigeration Capacity (kJ/m^3)	2868	22545

CO_2 refrigerant has demonstrated comparable performance to traditional R134a systems. Tests carried out for a compact VCS using R134a and CO_2, providing the same cooling capacity, showed that the CO_2 system had better coefficient of performance (cycle efficiency) by 40% at ambient temperatures below 40 C. Above 40 C, the coefficient of performance (COP) was 10% below the R134a baseline [12]. Additionally, the properties of CO_2 make it suitable for high capacity heat pump operation [13][14], which would be more energy efficient than electric heaters [15]. Compared to traditional refrigerants, CO_2 is an alternative that provides the opportunity for a smaller VCS, with high performance cooling and heating, and low global warming potential.

1.2 Transcritical Vapor Compression System

Due to the thermodynamic properties of CO_2 (R744), a vapor compression system (VCS) using this refrigerant will often operate above the critical temperature and pressure of the fluid and therefore is considered a transcritical VCS. In a subcritical VCS there are four standard components: the evaporator, condenser, compressor and expansion device. The low pressure, low temperature fluid absorbs heat from the secondary fluid (air) of the cooled space, and then the compressor elevates the fluid to a high pressure and high temperature. Through the condenser, heat is rejected to the ambient air and then the pressure is reduced through the expansion device. In transcritical systems, the condenser is referred to as a gas cooler because the fluid through the heat exchanger is single-phase supercritical fluid. CO_2 cycles often operate transcritical because the critical temperature of CO_2 is 31.1 C (87.98 F). In a cooling cycle, the heat is rejected to the ambient air, which can easily exceed this critical temperature. Figure 1.4 shows a comparison of the subcritical cycle of R134a and the transcritical cycle of CO_2 with the four standard components.

An internal heat exchanger is typically used for the CO_2 cycle to improve the coefficient of performance (COP), or efficiency, while maintaining safer operating conditions including a lower heat rejection pressure and superheated fluid entering the compressor [16]. The internal heat exchanger allows the refrigerant exiting the gas cooler and evaporator to exchange energy (Figure 1.5 and Figure 1.6). The COP improves because the refrigerant from the gas cooler is further cooled before the pressure is reduced through the expansion device, thereby increasing the cooling output of the evaporator.

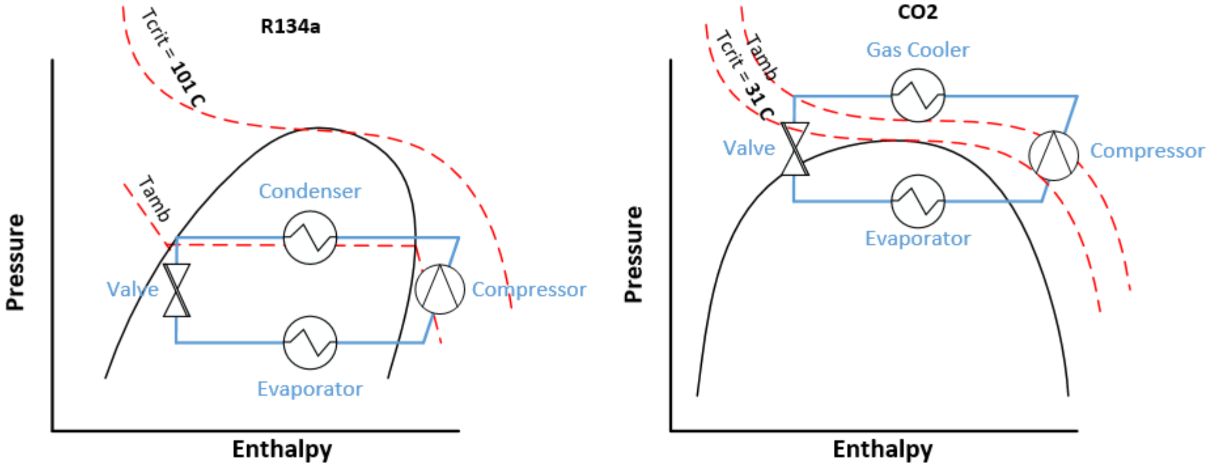

Figure 1.4 P-h diagrams of R134a subcritical vapor compression cycle and CO_2 transcritical vapor compression cycle, each with standard four components.

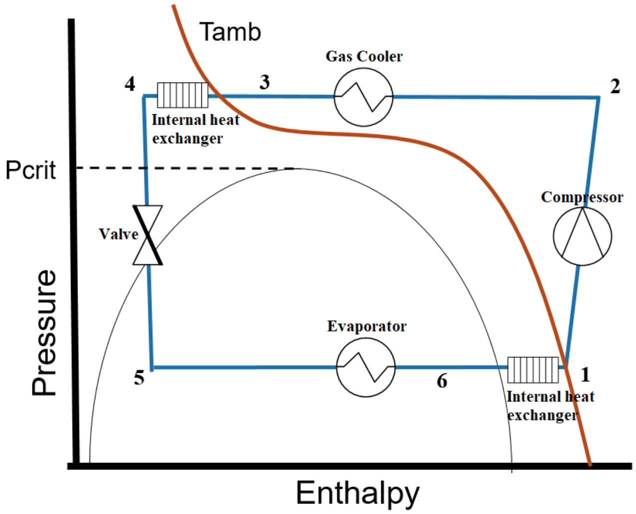

Figure 1.5 P-h diagram of CO_2 transcritical vapor compression cycle with internal heat exchanger.

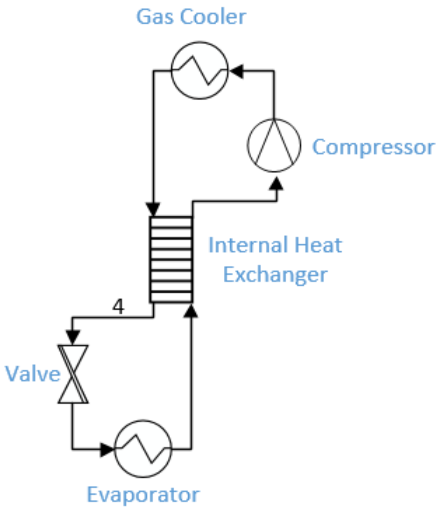

Figure 1.6 Diagram of a CO_2 transcritical vapor compression system components

1.2.1 Modeling

Extensive modeling efforts for subcritical systems are available in the literature [17]. The same approaches used for modeling subcritical components can also be used for transcritical cycles as detailed by Rasmussen et al. in [18]. However, Rasmussen uses a single control volume for the gas cooler and the internal heat exchanger, assuming lumped parameters for the entirety of the heat exchanger. This work improves upon this approach and discretizes the gas cooler and internal heat exchanger to achieve higher fidelity models. Additionally, the models of Rasmussen were validated for a relatively small range of inputs and outputs, whereas this work will study a larger range of inputs for control purposes.

1.2.2 Control

This section highlights the contributions of the available literature regarding control of CO_2 vapor compression systems. It has been reported that it is imperative to control the high side pressure because it has the most significant impact on the COP [19]–[24]. Reference [19] suggests a controller on only the high side pressure based on a correlation between optimum high side pressure and gas cooler outlet temperature. Reference [21] suggests a more detailed optimal high side pressure correlation that is a function of the gas cooler outlet temperature, the evaporator pressure and compressor efficiency. Both [19] and [21] recommend simultaneous control of the compressor speed and expansion valve aperture to achieve cooling load requirements and operate at the optimal heat rejection pressure. The results from [19] also suggests that increasing the evaporator air flow rate results in an increase of cooling capacity and COP, while compressor work remains almost constant.

Similarly, [24] suggests that their exists an optimal combination of EEV opening and compressor speed to achieve the optimal gas cooler pressure and COP. Reference [23] experimented with controlling the gas cooler pressure by regulating system charge, gas cooler fan speed and EEV opening. Of the controlled variables, it was found that the normalized charge had the greatest influence on the COP, followed by outdoor fan speed, and then the EEV opening.

Behr published the improvements they made in their control structure for a CO_2 system from first to second generation [25]. In the first generation (Figure 1.7), a variable displacement compressor is controlled to regulate the evaporator temperature via low side pressure and an electronic expansion valve regulates the high side pressure for COP. The first generation controller required three temperature sensors, two pressure sensors, and an electronic expansion valve. To reduce complexity and cost, Behr developed a second generation controller (Figure 1.8). In contrast, it utilizes two temperature sensors, one pressure sensor and a cheaper fixed orifice tube with bypass. The compressor regulates the evaporator temperature via the high side pressure (instead of the low side pressure in the first generation) and there is no COP control. The fixed orifice tube with bypass passively controls the high side pressure. Behr found the second generation control approach to provide good evaporator temperature reference tracking.

Reference [20] compared the performance of an adapted Behr first generation controller with their version of a simplified controller. The simplified configuration uses a two-stage orifice expansion valve that operates passively based on the pressure difference across the valve. The test controller uses one SISO loop to regulate the evaporator temperature by controlling the compressor. The COP is improved by use of the evaporator temperature set point, which is determined by a supervisory controller (Figure 1.9). However, it was found that with use of the controllable valve, the cycle COP was up to 15% better than with the passive valve.

Many of the works discussed have provided valuable suggestions of variables and actuators to control based on open-loop behavior, but have not extended these results in closed-loop. References [25] and [20] proposed controller structures but do not offer much transparency in the underlying formulations. Additionally, they do not include control of the evaporator fan, a third controllable actuator. This thesis intends to propose a few control strategies that control each of the available actuators: compressor, valve and evaporator fan. Details of each controller's structure and formulation will be provided, along with an assessment of performance tradeoffs.

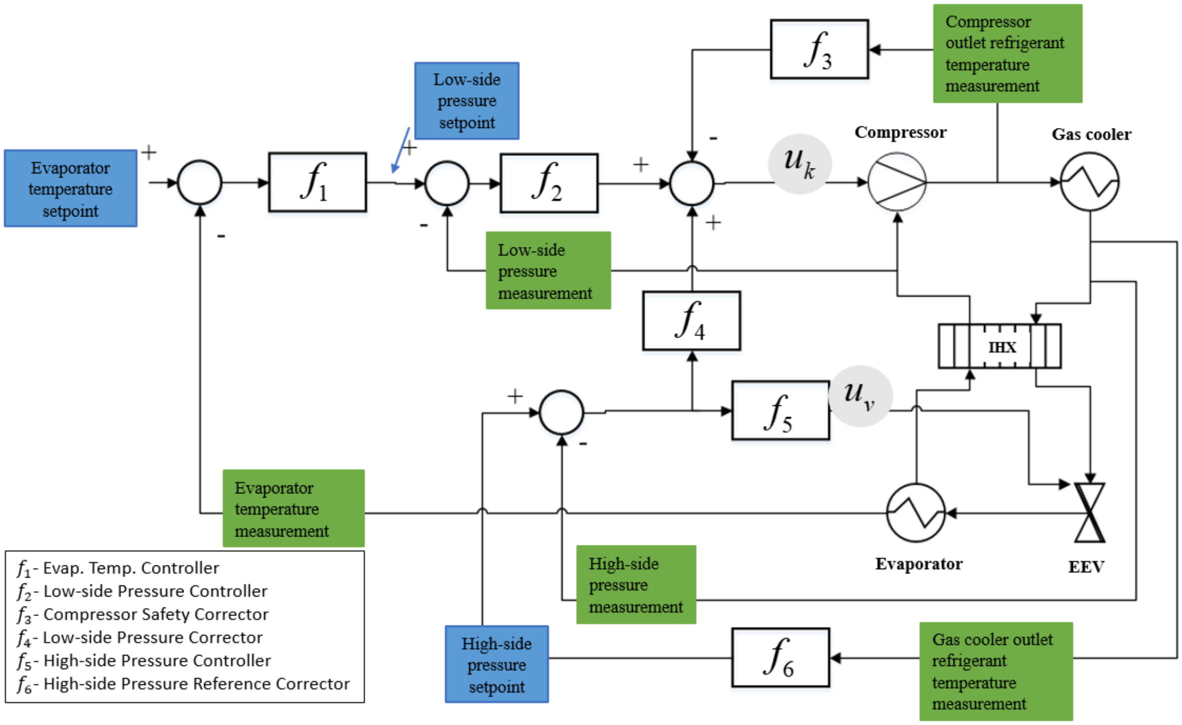

Figure 1.7 Behr first generation CO_2 vapor compression system control. Adapted from [25].

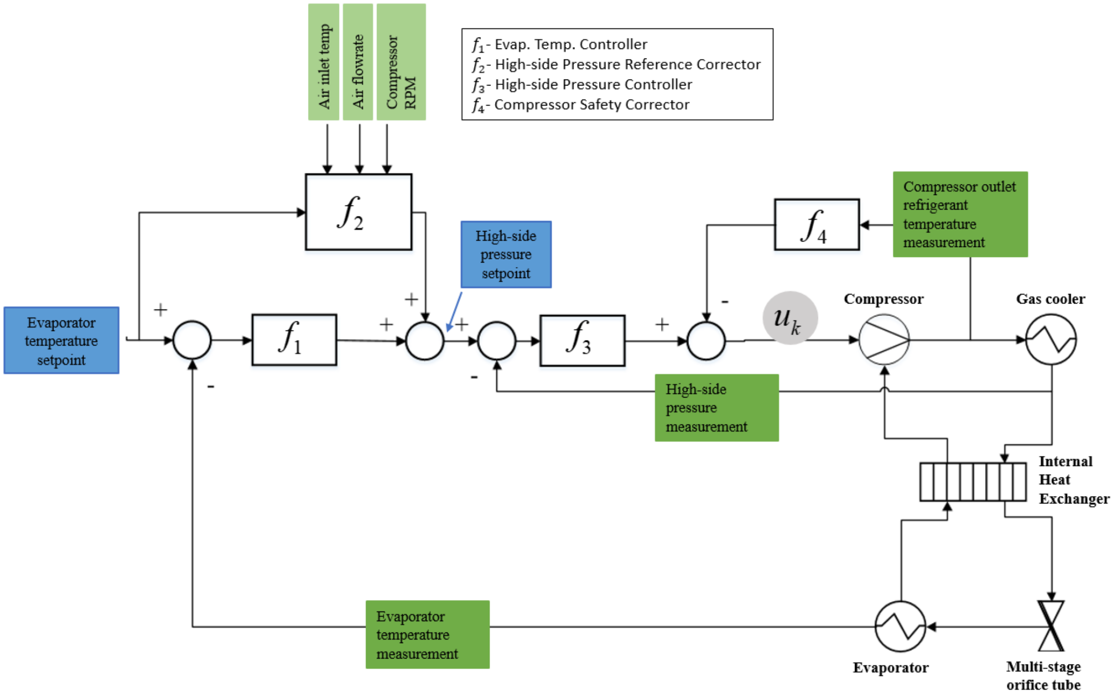

Figure 1.8 Behr second generation CO2 vapor compression system control. Adapted from [25].

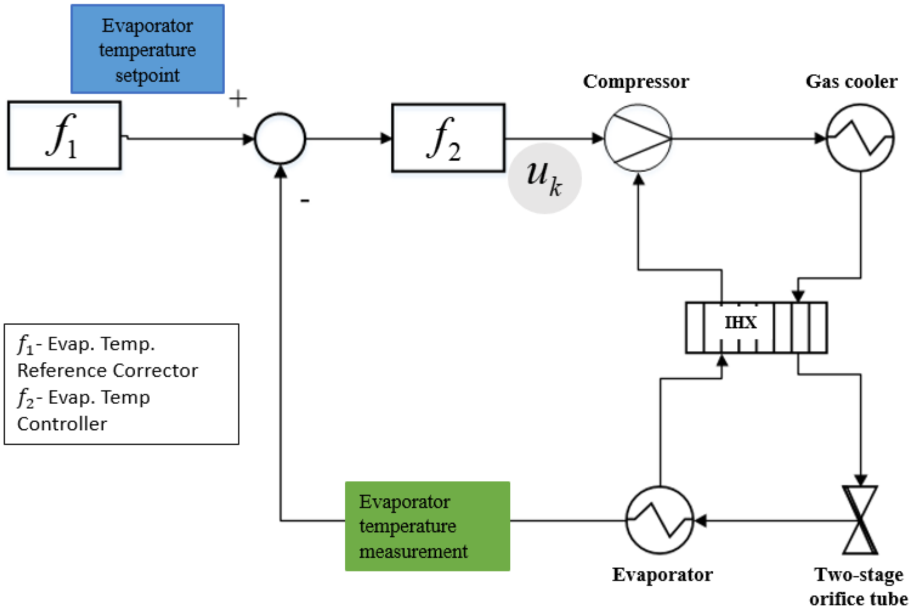

Figure 1.9 Control for transcritical VCS using two-stage orifice tube and supervisory controller for evaporator temperature set point to optimize cooling and COP. Adapted from [20].

1.3 Objectives

The objective of this research is to improve the range of battery electric vehicles. To achieve this goal, this work aims to: 1) develop a modeling framework for cooling architecture and control design, and 2) develop advanced controllers to manage thermal constraints of the battery pack and cabin while minimizing power consumption.

Integrate-able models are developed for a CO_2 transcritical vapor compression system, battery pack and cabin. The models are modular and scalable, allowing for design of various system architectures by dragging and dropping components into a graphical user environment. Furthermore, models capture electrical and thermal behavior in order to analyze the coupling of the systems and develop robust controllers.

Controllers are designed to manage the cabin and battery pack thermal loads simultaneously and minimize power consumption. This will improve the range of BEVs by maintaining the battery in the optimal temperature range and reducing power consumption of the cooling system. Baseline controllers using decoupled control loops are compared to a more advanced model predictive control method.

1.4 Organization of Thesis

The remainder of this thesis is organized as follows. Chapter 2 presents the mathematical modeling of the battery electric vehicle subsystems and open-loop responses of each subsystem. Chapter 3 demonstrates the capabilities to parameterize and combine subsystems to create a variety of system designs. Open-loop simulation results are provided for an air-cooled cabin, air-cooled battery pack system and an air-cooled cabin, liquid-cooled battery pack system. Chapter 4 introduces decentralized baseline controllers for cabin and battery pack temperature regulation. Chapter 5 provides the introduction to model predictive control and its implementation on the air-cooled cabin, air-cooled battery pack system. It also includes the process for system identification of linear models for the subsystems. The chapter demonstrates the benefits of MPC through illustrative simulation case studies. Chapter 6 presents conclusions and areas for future work.

Chapter 2 System Modeling

This section details the dynamic modeling for each subsystem: 1) transcritical vapor compression system, 2) battery pack, and 3) cabin. The models are developed to be modular and scalable for ease of system architecture design. Open-loop behavior of each subsystem is provided for model verification. The reader should note that the models have not been validated with physical data. As such, the results presented throughout the thesis should be considered for their qualitative input. Due to the modeling approaches used, it is expected that the models capture the dominant behaviors. However, determining system specific results would necessitate extensive subsystem and system validation. This validation work falls within the next steps as described in Chapter 6.

2.1 Transcritical Vapor Compression System

The models included in this work can be found in the Thermosys Toolbox [26] that was developed by the University of Illinois at Urbana-Champaign (UIUC) and CU Aerospace. Each component (heat exchanger, compressor, etc.) is modeled individually, but each is modular and able to be connected with other components to create various VCS configurations. This modeling framework consists of flow devices and pressure devices. Flow devices include compressors and valves; they receive a pressure signal from the upstream and downstream component (typically a heat exchanger) and transmit a mass flow rate signal to those adjacent components. The pressure devices include heat exchangers; they receive a mass flowrate signal from the upstream and downstream component (typically a compressor, pump or valve) and transmit a pressure signal to those adjacent components. In this section, the modeling approaches for transcritical VCS components are described. The dynamics of the actuating components, i.e. compressor and expansion valve are fast in comparison to the dynamics of the heat exchangers; therefore, these components are modeled with algebraic relationships, whereas the heat exchangers are modeled dynamically with governing differential equations [18].

2.1.1 Compressor

A variable speed, fixed displacement compressor is modeled with pressure inputs from adjacent components. The model outputs a refrigerant mass flow rate and enthalpy. User defined volumetric and isentropic efficiency maps that are a function of compressor speed and pressure ratio account for losses.

$$\dot{m} = \omega V \rho \eta_v \tag{2.1}$$

$$h_{out}^{static} = \frac{1}{\eta_k}\left[h_{out,isen} + h_{in}\left(\eta_k - 1\right)\right] \tag{2.2}$$

A first order filter on the enthalpy improves the accuracy of the enthalpy due to the large thermal capacitance of the compressor shell that is unaccounted for otherwise [27].

$$\frac{dh_{out}}{dt} = \frac{1}{\tau}\left(h_{out}^{static} - h_{out}\right) \tag{2.3}$$

where τ is determined experimentally or estimated.

2.1.2 Electronic expansion valve

An electronic expansion valve (EEV) model is developed based on a correlation fit to Bernoulli’s equations with an expansion factor [28].

$$\dot{m} = c_D A Y \sqrt{2\rho_{in,s} P_{in} X} \tag{2.4}$$

where c_D is the mass flow coefficient determined empirically, Y an expansion factor, and X the pressure differential ratio. The expansion factor accounts for changes in density as the fluid moves through the expansion device [29] and the pressure differential ratio accounts for flow patterns.

$$Y = 1 - X / \left(3\Delta P_{cr} / P_{in}\right) \tag{2.5}$$

$$X = \begin{cases} \dfrac{P_{in} - P_{out}}{P_{in}}, & \text{if } P_{in} - P_{out} < \Delta P_{cr} \\ \dfrac{\Delta P_{cr}}{P_{in}}, & \text{if } P_{in} - P_{out} \geq \Delta P_{cr} \end{cases} \tag{2.6}$$

where ΔP_{cr} is the pressure differential that corresponds to the critical mass flow rate (flow is choked). The mass flow coefficient was determined empirically by [28] to be

$$c_D = 1.1075 z^{0.4436} \left(\frac{\rho_{in}}{\rho_{in,s}} \right)^{-1.4971} \left(\frac{P_{in} - P_{in,s}}{XP_{in}} \right)^{0.0131} \tag{2.7}$$

2.1.3 Heat Exchangers

Heat exchangers are modeled using conservation equations and simplifying assumptions [18], [27], [30]:

1. The refrigerant flows through a long, thin, uniform horizontal tube
2. Refrigerant flows only in the longitudinal direction
3. Axial conduction is negligible
4. Momentum change and viscous friction in the refrigerant are negligible (the heat exchanger is isobaric)

As a result, conservation of refrigerant mass, refrigerant energy and wall energy can be applied to each control volume of the heat exchanger, Equations 2.8-2.10 respectively.

$$A_{cs,r} \frac{\partial \rho_r}{\partial t} + \frac{\partial \dot{m}_r}{\partial x} = 0 \tag{2.8}$$

$$A_{cs,r} \frac{\partial \left(\rho h - P \right)_r}{\partial t} + \frac{\partial \left(\dot{m} h \right)_r}{\partial x} = p \alpha_r \left(T_w - T_r \right) \tag{2.9}$$

$$\left(A_{cs} \rho c_p \right)_w \frac{\partial T_w}{\partial t} = p \alpha_r \left(T_r - T_w \right) + p \alpha_a \left(T_a - T_w \right) \tag{2.10}$$

There are two common methods in the literature to discretize heat exchangers into distinct control volumes: moving boundary (MB) and finite volume (FV) lumped parameter methods. The moving boundary method can decrease computational cost while maintaining high accuracy in multi-phase heat exchangers, such as evaporators and condensers, because the heat exchanger can be divided into control volumes based on the number of fluid phases present in the heat exchanger at each time step. The length of each control volume changes with time and average properties are used for each volume. However, for single-phase heat exchangers, such as the gas cooler and internal heat exchanger, the MB method would result in only one volume with lumped parameters. This would be very inaccurate in the case of supercritical fluid because the pressure and temperature are independent properties. For example, the temperature of the refrigerant will have a large gradient over the length of a gas cooler compared to a condenser that is operating completely within two-phase, where the temperature is at saturation across the length. Therefore, the FV approach is preferred for single-phase heat exchangers. For these reasons, the evaporator and liquid-to-liquid heat exchanger models use the MB approach and the gas cooler and internal heat exchanger use the FV approach. The general approach is to convert the partial differential equations (PDEs) of (2.8-2.10) to ordinary differential equations (ODEs) by integrating over the length of each control volume.

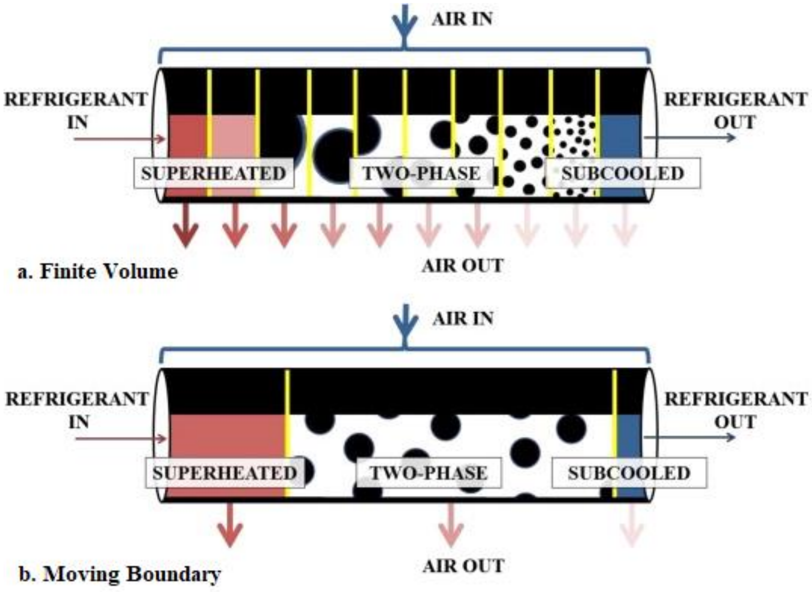

Figure 2.1 Heat exchanger tube discretization for (a) finite volume approach, (b) moving boundary approach [30]

2.1.3.1 Moving Boundary Approach

With use of the moving boundary approach, the length of control volumes are states. In order to integrate over changing lengths, Leibniz's rule (2.11), rearranged in (2.12), provides the formulation for the integral of a PDE with time dependent limits. This is applied to the PDEs (2.8-2.10).

$$\frac{d}{dt}\left(\int_{x_1(t)}^{x_2(t)} f(x,t)dx\right) = f\left(x,x_2(t)\right)*\frac{d}{dt}\left(x_2(t)\right) - f\left(x,x_1(t)\right)*\frac{d}{dt}\left(x_1(t)\right) + \int_{x_1(t)}^{x_2(t)} \frac{\partial f(x,t)}{\partial t}dx \tag{2.11}$$

$$\int_{x_1(t)}^{x_2(t)} \tfrac{\partial f(x,t)}{\partial t}\,dx = \tfrac{d}{dt}\left(\int_{x_1(t)}^{x_2(t)} f(x,t)dx\right) - f\left(x, x_2(t)\right) * \tfrac{d}{dt}\left(x_2(t)\right) + f\left(x, x_1(t)\right) * \tfrac{d}{dt}\left(x_1(t)\right) \tag{2.12}$$

To fully describe the heat exchanger requires the wall temperature of each fluid region, two refrigerant properties for each region (pressure of the heat exchanger, assumed constant, is one of the two properties of the refrigerant for each region), and the length of each region (although one region can be determined algebraically). If a superheat or subcooled region exists, the refrigerant property states chosen are pressure and enthalpy. If a two-phase region exists, the refrigerant property states chosen are the pressure and mean void fraction. Mean void fraction provides a simplifying estimation of the ratio of vapor to liquid in the two-phase region in order to determine lumped parameters for that volume [27], [30]. Given all three fluid regions are considered, then there exists 9 states: $\begin{bmatrix} P_r & T_{w,1} & T_{w,2} & T_{w,3} & \zeta_1 & \zeta_2 & h_{SC} & \gamma_{TP} & h_{SH} \end{bmatrix}$ and $\zeta_3 = 1 - \zeta_1 - \zeta_2$. To implement this approach requires switching logic to determine which phases are present in the heat exchanger and use the correct set of equations. This will be described in more detail in the evaporator modeling section.

2.1.3.1.1 Evaporator

In the case of an evaporative heat exchanger, it is assumed to operate in three modes: entirely two-phase, entirely superheated, or two-phase and superheated fluid. This results in 6 states $\begin{bmatrix} P_r & T_{w,1} & T_{w,2} & \zeta_1 & \gamma_{TP} & h_{SH} \end{bmatrix}$ and $\zeta_2 = 1 - \zeta_1$.

Table 2.1 Evaporator states for three modes of operation

	TP+SH	TP	SH
Evaporator	$\begin{bmatrix} P_r & T_{w,1} & T_{w,2} & \zeta_1 & \gamma_{TP} & h_{SH} \end{bmatrix}$ $\zeta_2 = 1 - \zeta_1$ $T_w = \zeta_1 T_{w,1} + \zeta_2 T_{w,2}$	$\begin{bmatrix} P_r & T_{w,1} & \gamma_{TP} \end{bmatrix}$ $\zeta_1 = 1$ $T_w = T_{w,1}$	$\begin{bmatrix} P_r & T_{w,2} & h_{SH} \end{bmatrix}$ $\zeta_2 = 1$ $T_w = T_{w,2}$

<u>Mode 1: 2 Zones</u>

This section will derive the equations for 2 zone operation of the evaporator based on the conservation equations (2.8-2.10). First, each equation is integrated spatially over the length of each zone.

Conservation of Refrigerant Mass

$$\int_0^{L_1}\left[\frac{\partial(\rho A_{cs})}{\partial t}+\frac{\partial \dot{m}}{\partial x}\right]dx=0 \tag{2.13}$$

$$\int_{L_1}^{L_{total}}\left[\frac{\partial(\rho A_{cs})}{\partial t}+\frac{\partial \dot{m}}{\partial x}\right]dx=0 \tag{2.14}$$

Conservation of Refrigerant Energy

$$\int_0^{L_1}\left[\frac{\partial(\rho A_{cs}h-PA_{cs})}{\partial t}+\frac{\partial(\dot{m}h)}{\partial x}\right]dx=\int_0^{L_1}\left[p\alpha_r(T_w-T_r)\right]dx \tag{2.15}$$

$$\int_{L_1}^{L_{total}}\left[\frac{\partial(\rho A_{cs}h-PA_{cs})}{\partial t}+\frac{\partial(\dot{m}h)}{\partial x}\right]dx=\int_{L_1}^{L_{total}}\left[p\alpha_r(T_w-T_r)\right]dx \tag{2.16}$$

Conservation of Wall Energy

$$\int_0^{L_1}\tfrac{\partial(\rho A_{cs}c_pT_w)}{\partial t}\,dx=\int_0^{L_1}\left[p\alpha_r(T_r-T_w)+p\alpha_a(T_a-T_w)\right]dx \tag{2.17}$$

$$\int_{L_1}^{L_{total}}\tfrac{\partial(\rho A_{cs}c_pT_w)}{\partial t}\,dx=\int_{L_1}^{L_{total}}\left[p\alpha_r(T_r-T_w)+p\alpha_a(T_a-T_w)\right]dx \tag{2.18}$$

Then Equation 2.12 is applied to the first term of Equations 2.13-2.18.

Conservation of Refrigerant Mass

$$A_{cs}\left[\tfrac{d}{dt}\left[\int_0^{L_1}\rho dx\right]-\rho\Big|_{L_1}\tfrac{dL_1}{dt}\right]+\dot{m}_{TP-SH}-\dot{m}_{r,in}=0 \tag{2.19}$$

$$A_{cs}\left[\tfrac{d}{dt}\left[\int_{L_1}^{L_{total}}\rho dx\right]+\rho\Big|_{L_1}\tfrac{dL_1}{dt}\right]+\dot{m}_{r,out}-\dot{m}_{TP-SH}=0 \tag{2.20}$$

Conservation of Refrigerant Energy

$$A_{cs}\left[\tfrac{d}{dt}\left[\int_0^{L_1}\left(\rho h-P\right)dx\right]-\left(\rho h-P\right)\Big|_{L_1}\tfrac{dL_1}{dt}\right]+\dot{m}_{TP-SH}h_v-\dot{m}_{r,in}h_{r,in}=pL_1\alpha_{r,1}(T_{w,1}-T_{r,1}) \tag{2.21}$$

$$A_{cs}\left[\tfrac{d}{dt}\left[\int_{L_1}^{L_1+L_2}\left(\rho h-P\right)dx\right]+\left(\rho h-P\right)\Big|_{L_1}\tfrac{dL_1}{dt}\right]+\dot{m}_{r,out}h_{r,out}-\dot{m}_{TP-SH}h_v=p\left(L_{total}-L_1\right)\alpha_{r,2}\left(T_{w,2}-T_{r,2}\right) \tag{2.22}$$

Conservation of Wall Energy

$$\rho A_{cs} c_p \left[\tfrac{d}{dt}\left[\int_0^{L_1} T_w \right] - T_w\Big|_{L_1} \tfrac{dL_1}{dt} \right] = pL_1 \alpha_{r,1}(T_{r,1} - T_{w,1}) + pL_1 \alpha_a (T_a - T_{w,1}) \tag{2.23}$$

$$\rho A_{cs} c_p \left[\tfrac{d}{dt}\left[\int_{L_1}^{L_1+L_2} T_w \right] + T_w\Big|_{L_1} \tfrac{dL_1}{dt} \right] = p(L_{total} - L_1)\alpha_{r,2}(T_{r,2} - T_{w,2}) + p(L_{total} - L_1)\alpha_a (T_a - T_{w,2}) \tag{2.24}$$

Recall, that for each volume we are assuming lumped parameters and that at the boundary, $\rho\big|_{L_1} = \rho_v$ and $h\big|_{L_1} = h_v$, the density and enthalpy of saturated vapor. Integrating and using the product rule on the first term of Equations 2.19-2.24 results in Equations 2.25-2.30. Note that $L_{total} = L_1 + L_2$ and $\frac{d(L_{total})}{dt} = 0 = \dot{L}_1 + \dot{L}_2$ i.e. $\dot{L}_1 = -\dot{L}_2$.

Conservation of Refrigerant Mass

$$L_1 \frac{d\rho_1}{dt} + (\rho_1 - \rho_v)\frac{dL_1}{dt} = \frac{\dot{m}_{r,in} - \dot{m}_{TP-SH}}{A_{cs}} \tag{2.25}$$

$$(L_{total} - L_1)\frac{d\rho_2}{dt} + (\rho_v - \rho_2)\frac{dL_1}{dt} = \frac{\dot{m}_{TP-SH} - \dot{m}_{r,out}}{A_{cs}} \tag{2.26}$$

Conservation of Refrigerant Energy

$$L_1 \frac{d(\rho_1 h_1 - P)}{dt} + (\rho_1 h_1 - \rho_v h_v)\frac{dL_1}{dt} = \frac{\dot{m}_{r,in} h_{r,in} - \dot{m}_{TP-SH} h_v + A_{surf}\zeta_1 \alpha_{r,1}(T_{w,1} - T_{r,1})}{A_{cs}} \tag{2.27}$$

$$(L_{total} - L_1)\frac{d(\rho_2 h_2 - P)}{dt} + (\rho_v h_v - \rho_2 h_2)\frac{dL_1}{dt} = \frac{\dot{m}_{TP-SH} h_v - \dot{m}_{r,out} h_{r,out} + A_{surf}(1-\zeta_1)\alpha_{r,2}(T_{w,2} - T_{r,2})}{A_{cs}} \tag{2.28}$$

Conservation of Wall Energy

$$L_1 \frac{dT_{w,1}}{dt} + \left[T_{w,1} - T_w\big|_{L_1} \right]\frac{dL_1}{dt} = \frac{A_{surf}\zeta_1 \left[\alpha_{r,1}(T_{r,1} - T_{w,1}) + \alpha_a (T_a - T_{w,1}) \right]}{\rho A_{cs} c_p} \tag{2.29}$$

$$(L_{total} - L_1)\frac{dT_{w,2}}{dt} + \left[T_w\big|_{L_1} - T_{w,2} \right]\frac{dL_1}{dt} = \frac{A_{surf}(1-\zeta_1)\left[\alpha_{r,2}(T_{r,2} - T_{w,2}) + \alpha_a (T_a - T_{w,2}) \right]}{\rho A_{cs} c_p} \tag{2.30}$$

Lastly, Equations 2.25-2.30 are normalized by the total length of the heat exchanger, $\frac{L_1}{L_{total}} = \zeta_1$.

Conservation of Refrigerant Mass

$$\zeta_1 \frac{d\rho_1}{dt} + \left(\rho_1 - \rho_v\right)\frac{d\zeta_1}{dt} = \frac{\dot{m}_{r,in} - \dot{m}_{TP-SH}}{V_{total}} \tag{2.31}$$

$$\left(1-\zeta_1\right)\frac{d\rho_2}{dt} + \left(\rho_v - \rho_2\right)\frac{d\zeta_1}{dt} = \frac{\dot{m}_{TP-SH} - \dot{m}_{r,out}}{V_{total}} \tag{2.32}$$

Conservation of Refrigerant Energy

$$\zeta_1 \frac{d\left(\rho_1 h_1 - P\right)}{dt} + \left(\rho_1 h_1 - \rho_v h_v\right)\frac{d\zeta_1}{dt} = \frac{\dot{m}_{r,in} h_{r,in} - \dot{m}_{TP-SH} h_v + A_{surf}\zeta_1 \alpha_{r,1}(T_{w,1} - T_{r,1})}{V_{total}} \tag{2.33}$$

$$\left(1-\zeta_1\right)\frac{d\left(\rho_2 h_2 - P\right)}{dt} + \left(\rho_v h_v - \rho_2 h_2\right)\frac{d\zeta_1}{dt} = \frac{\dot{m}_{TP-SH} h_v - \dot{m}_{r,out} h_{r,out} + A_{surf}(1-\zeta_1)\alpha_{r,2}(T_{w,2} - T_{r,2})}{V_{total}} \tag{2.34}$$

Conservation of Wall Energy

$$\zeta_1 \frac{dT_{w,1}}{dt} + \left[T_{w,1} - T_w\big|_{L_1}\right]\frac{d\zeta_1}{dt} = \frac{A_{surf}\zeta_1\left[\alpha_{r,1}(T_{r,1} - T_{w,1}) + \alpha_a(T_a - T_{w,1})\right]}{\rho V_{total} c_p} \tag{2.35}$$

$$\left(1-\zeta_1\right)\frac{dT_{w,2}}{dt} + \left[T_w\big|_{L_1} - T_{w,2}\right]\frac{d\zeta_1}{dt} = \frac{A_{surf}(1-\zeta_1)\left[\alpha_{r,2}(T_{r,2} - T_{w,2}) + \alpha_a(T_a - T_{w,2})\right]}{\rho V_{total} c_p} \tag{2.36}$$

Next, we will use Equation 2.31 (or 2.32) to solve for $\dot{m}_{TP-SH}$ and substitute into 2.32 (or 2.31), 2.33 and 2.34. This is because the intermediate mass flow rate is something that we can't measure on a physical system and it is challenging to calculate.

It is also important to simplify the equations to be in terms of the states that we desire (and could measure on a physical system). Refer back to Table 2.1 for the chosen states. Therefore, in the superheated equations, the density derivative will be re-written in terms of pressure and enthalpy (Equation 2.37).

$$\frac{d\rho_1}{dt} = \frac{d\rho_1}{dP}\bigg|_{h_1}\frac{dP}{dt} + \frac{d\rho_1}{dh_1}\bigg|_{P}\frac{dh_1}{dt} \tag{2.37}$$

And in the two phase zone the density and enthalpy derivatives, defined from mean void fraction (Equations 2.38-2.39), will be re-written in terms of pressure and mean void fraction (Equations 2.40-2.41).

$$\rho_2 = \bar{\gamma}\rho_v + (1-\bar{\gamma})\rho_f \tag{2.38}$$

$$h_2 = \frac{\bar{\gamma} h_v \rho_v + (1-\bar{\gamma}) h_f \rho_f}{\bar{\gamma}\rho_v + (1-\bar{\gamma})\rho_f} \tag{2.39}$$

$$\frac{d\rho_2}{dt} = \left.\frac{d\rho_2}{dP}\right|_{\bar{\gamma}} \frac{dP}{dt} + \left.\frac{d\rho_2}{d\bar{\gamma}}\right|_P \frac{d\bar{\gamma}}{dt} \tag{2.40}$$

$$\frac{dh_2}{dt} = \left.\frac{dh_2}{dP}\right|_{\bar{\gamma}} \frac{dP}{dt} + \left.\frac{dh_2}{d\bar{\gamma}}\right|_P \frac{d\bar{\gamma}}{dt} \tag{2.41}$$

With these substitutions, the six Equations 2.31-2.36 becomes the 5 Equations (2.42-2.46) (one less equation because of solving for the intermediate mass flow rate).

$$\left[\rho_1 - \rho_2\right]\frac{d\zeta_1}{dt} + \left[\zeta_1 \left.\frac{\partial\rho_1}{dP}\right|_{\bar{\gamma}} + \zeta_2 \left.\frac{\partial\rho_2}{dP}\right|_{h_2}\right]\frac{dP}{dt} + \left[\zeta_2 \left.\frac{\partial\rho_2}{dh_2}\right|_P\right]\frac{dh_2}{dt} + \left[\zeta_1 \left.\frac{\partial\rho_1}{d\bar{\gamma}}\right|_P\right]\frac{d\bar{\gamma}}{dt} = \frac{\dot{m}_{r,in} - \dot{m}_{r,out}}{V_{total}} \tag{2.42}$$

$$\left[\rho_1 h_1 - \rho_2 h_v\right]\frac{d\zeta_1}{dt} + \left[\zeta_1\left(h_1 \left.\frac{\partial\rho_1}{dP}\right|_{\bar{\gamma}} + \rho_1 \left.\frac{\partial h_1}{dP}\right|_{\bar{\gamma}} - 1\right) + \zeta_2 h_v \left.\frac{\partial\rho_2}{dP}\right|_{h_2}\right]\frac{dP}{dt} + \left[\zeta_2 h_v \left.\frac{\partial\rho_2}{dh_2}\right|_P\right]\frac{dh_2}{dt} + \left[\zeta_1\left(h_1 \left.\frac{\partial\rho_1}{d\bar{\gamma}}\right|_P + \rho_1 \left.\frac{\partial h_1}{d\bar{\gamma}}\right|_P\right)\right]\frac{d\bar{\gamma}}{dt} = \frac{\dot{m}_{r,in} h_{r,in} - \dot{m}_{r,out} h_v + A_{surf}\zeta_1\alpha_{r,1}(T_{w,1} - T_{r,1})}{V_{total}} \tag{2.43}$$

$$\left[\rho_2\left(h_v - h_2\right)\right]\frac{d\zeta_1}{dt} + \left[\zeta_2\left(\left(h_2 - h_v\right)\left.\frac{\partial\rho_2}{dP}\right|_{h_2} - 1\right)\right]\frac{dP}{dt} + \left[\zeta_2\left(\left(h_2 - h_v\right)\left.\frac{\partial\rho_2}{dh_2}\right|_P + \rho_2\right)\right]\frac{dh_2}{dt} = \frac{\dot{m}_{r,out}(h_v - h_{r,o}) + A_{surf}\zeta_2\alpha_{r,2}(T_{w,2} - T_{r,2})}{V_{total}} \tag{2.44}$$

$$\zeta_1 \frac{dT_{w,1}}{dt} + \left[T_{w,1} - \left.T_w\right|_{L_1}\right]\frac{d\zeta_1}{dt} = \frac{A_{surf}\zeta_1\left[\alpha_{r,1}(T_{r,1} - T_{w,1}) + \alpha_a(T_a - T_{w,1})\right]}{m_w c_p} \tag{2.45}$$

$$\zeta_2 \frac{dT_{w,2}}{dt} + \left[T_w\big|_{L_1} - T_{w,2} \right] \frac{d\zeta_1}{dt} = \frac{A_{surf}\zeta_2 \left[\alpha_{r,2}(T_{r,2} - T_{w,2}) + \alpha_a (T_a - T_{w,2}) \right]}{m_w c_p} \tag{2.46}$$

To provide the sixth equation to solve for all of the states, we define a dynamic mean void fraction state with the use of an error minimization equation, Equation 2.47, where k is chosen so that this dynamic is much faster than the other dynamics of the system. The dynamic mean void fraction is tracking the instantaneous mean void fraction. Mean void fraction and its equations are described in further detail in [27].

$$\frac{d\bar{\gamma}}{dt} - \frac{d\bar{\gamma}_{track}}{dt}\frac{dP}{dt} = k\left(\bar{\gamma}_{track} - \bar{\gamma}\right) \tag{2.47}$$

Finally, the air outlet temperature from the evaporator is calculated using the NTU-method. The NTU (Equation 2.48) is used to calculate the heat transferred from the heat exchanger wall to the air (Equation 2.49), and then the outlet air temperature is calculated by Equation 2.50.

$$NTU \equiv \frac{\alpha_a A_{surf}}{\dot{m}_{a,in} c_{p,a}} \tag{2.48}$$

$$Q_{a,i} = \dot{m}_{a,in} c_{p,a} (T_{a,in} - T_{w,i} - (T_{a,in} - T_{w,i}) \exp(-NTU))\zeta_i \tag{2.49}$$

$$T_{a,out} = \frac{-\sum_{j=1}^{n} Q_{a,i}}{\dot{m}_{a,in} c_{p,a}} + T_{a,in} \tag{2.50}$$

Similarly, state equations can be derived for the other two modes of operation, only two-phase or only superheat. These derivations are simpler because there are no intermediate mass flowrates; therefore, the three equations are used to solve for the three state variables. Furthermore, this approach can be extended to other multi-phase heat exchangers, such as a two-fluid plate evaporator (liquid-to-liquid heat exchanger).

2.1.3.2 Finite Volume Approach

The finite volume (FV) approach discretizes the heat exchanger into n equivalent sized volumes. Similar to the moving boundary approach, each volume considers conservation of refrigerant mass, conservation of refrigerant energy and conservation of wall energy. The steps for the FV approach are [30]:

1. Discretize the heat exchanger into n equal sized volumes, each with an average thermodynamic state at time t (Figure 2.1)

2. Integrate over the length of each n volume

3. Choose independent state variables and reduce the conservation equations

Each control volume assumes lumped parameters and an average state. Because the control volumes are not based on fluid phase, a volume can include two phases, but it will take on an average state that lies within one phase or the other. Consequently, computational issues can arise due to discontinuity of the heat transfer coefficient between fluid phases if a control volume is switching back and forth between phases. The discontinuity results from the use of different heat transfer correlations for each fluid phase. To remedy the issue, a 4th order look-up table is generated for heat transfer coefficients for a range of mass flow rates, pressures, inlet enthalpies, and enthalpy differences and then a smoothing function is applied to remove the discontinuity (Figures 2.2-2.3).

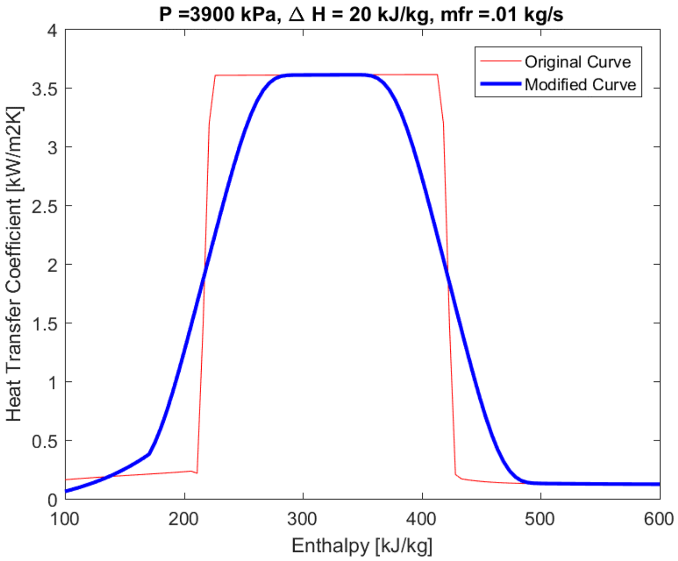

Figure 2.2 Original and modified evaporator heat transfer coefficient profile for CO_2 refrigerant P=3900 kPa, $\dot{m}$ =.01 kg/s and ΔH = 20 kJ/kg

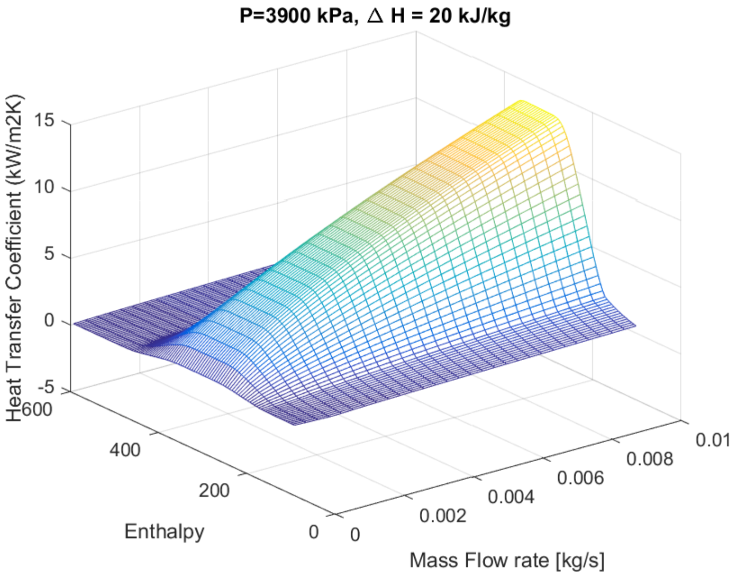

Figure 2.3 Evaporator heat transfer coefficient smoothed profile for a range of enthalpy and mass flow rate values, P=3900 kPa and ΔH =20 kJ/kg

2.1.3.2.1 Internal Heat Exchanger

This section will discuss how the finite volume (FV) approach can be applied for the internal heat exchanger. The internal heat exchanger operates in counter-flow. Furthermore, it is assumed the high pressure side is supercritical single phase fluid and that the low pressure side can be two-phase fluid, superheated fluid or both. The conservation of refrigerant mass and energy equations can be applied to the high-pressure and low-pressure fluid flows separately. First, the conservation equations (2.8-2.10) are integrated over the length of the control volume. Since the control volume lengths are not changing with time, the integration is simpler.

$$\dot{\rho}_{r,i} = \left(\left.\frac{\partial \rho}{\partial P}\right|_{h} \right)_{r,i} \dot{P}_r + \left(\left.\frac{\partial \rho}{\partial h}\right|_{P} \right)_{r,i} \dot{h}_{r,i} \tag{2.51}$$

Conservation of Refrigerant Energy

$$\int_{x_i}^{x_i+\Delta x} \left[\frac{\partial(\rho A_{cs})}{\partial t} + \frac{\partial \dot{m}}{\partial x} \right] dx = 0 \tag{2.52}$$

$$\frac{\partial \rho_{r,i}}{\partial t} A_{cs} \Delta x + \dot{m}_{r,i,out} - \dot{m}_{r,i,in} = 0 \tag{2.53}$$

Conservation of Refrigerant Mass

$$\int_{x_i}^{x_i+\Delta x}\left[\tfrac{\partial(\rho A_{cs}h-PA_{cs})}{\partial t}+\tfrac{\partial(\dot{m}h)}{\partial x}\right]dx=\int_{x_i}^{x_i+\Delta x}\left[p\alpha_r(T_w-T_r)\right]dx \tag{2.54}$$

$$\frac{\partial(\rho h-P)_{r,i}}{\partial t}A_{cs}\Delta x+\left(\dot{m}h\right)_{r,i,out}-\left(\dot{m}h\right)_{r,i,in}=\Delta xp\alpha_{r,i}(T_{w,i}-T_{r,i}) \tag{2.55}$$

Note: $A_{cs}\Delta x$ is the volume of the control volume, V_{cv}, and $\Delta x*p$ is the surface area of the refrigerant tube, $A_{s,cv}$. Choosing pressure and enthalpy as state variables the equations for each control volume are as follows:

Conservation of Refrigerant Energy

$$V_{cv}\left[\left(\left.\frac{\partial\rho}{\partial P}\right|_h\right)_{r,i}\dot{P}_r+\left(\left.\frac{\partial\rho}{\partial h}\right|_P\right)_{r,i}\dot{h}_{r,i}\right]=\dot{m}_{r,i,in}-\dot{m}_{r,i,out} \tag{2.56}$$

Conservation of Refrigerant Mass

$$\begin{aligned}&V_{cv}\left[\left(\left.\frac{\partial\rho}{\partial P}\right|_h\right)_{r,i}h_{r,i}-1\right]\dot{P}_r+V_{cv}\left[\left(\left.\frac{\partial\rho}{\partial h}\right|_P\right)_{r,i}h_{r,i}+\rho_{r,i}\right]\dot{h}_{r,i}\\&=\left(\dot{m}h\right)_{r,i_{in}}-\left(\dot{m}h\right)_{r,i_{out}}+A_{surf,cv}\alpha_{r,i}\left(T_{w,i}-T_{r,i}\right)\end{aligned} \tag{2.57}$$

Finally, conservation of wall energy is considered with heat transfer from each fluid flow. There is no secondary fluid (i.e. air) for an internal heat exchanger since each refrigerant side is exchanging energy with the wall.

Conservation of Wall Energy

$$\int_{x_i}^{x_i+\Delta x}\tfrac{\partial(\rho A_{cs}c_pT_w)}{\partial t}dx=\int_{x_i}^{x_i+\Delta x}\left[p\alpha_{r,LP}(T_{r,LP}-T_w)+p\alpha_{r,HP}(T_{r,HP}-T_w)\right]dx \tag{2.58}$$

$$\frac{\partial T_{w,i}}{\partial t}\left(\rho c_p\right)_w A_{cs}\Delta x=\Delta xp\alpha_{r,LP,i}\left(T_{r,LP,i}-T_{w,i}\right)+\Delta xp\alpha_{r,HP,i}\left(T_{r,HP,i}-T_{w,i}\right) \tag{2.59}$$

Note: $\rho A_{cs}\Delta x$ is the mass of wall for that control volume. Equation 2.59 is simplified to 2.60.

$$\left(mc_p\right)_{w,cv}\dot{T}_{w,i}=A_{surf,cv}\alpha_{r,LP,i}\left(T_{r,LP,i}-T_{w,i}\right)+A_{surf,cv}\alpha_{r,HP,i}\left(T_{r,HP,i}-T_{w,i}\right) \tag{2.60}$$

In order to extend this to multiple volumes, the intermediate mass flow rates become part of the state vector. With n volumes there will be $5n+2$ states that can be solved with three generalized equations:

$$\left(\dot{P}_{r,LP}\ \dot{h}_{r,LP,1}\ \cdots\ \dot{h}_{r,LP,N}\ \dot{m}_{r,1;2}\ \cdots\ \dot{m}_{r,N-1;N}\right)^T = A_{LP}^{-1} y_{LP}, \tag{2.61}$$

$$\left(\dot{P}_{r,HP}\ \dot{h}_{r,HP,1}\ \cdots\ \dot{h}_{r,HP,N}\ \dot{m}_{r,1;2}\ \cdots\ \dot{m}_{r,N-1;N}\right)^T = A_{HP}^{-1} y_{HP}, \tag{2.62}$$

$$\left(\dot{T}_{w,1}\ \cdots\ \dot{T}_{w,N}\right)^T = A_w^{-1} y_w, \tag{2.63}$$

A first order filter is placed upon the mass flow rate states to improve numerical robustness and speed of simulation.

$$\frac{d\dot{m}}{dt} = \frac{1}{\tau}\left(\dot{m}^{stat} - \dot{m}\right) \tag{2.64}$$

2.1.3.2.2 Gas Cooler

The derivation of the gas cooler is very similar to that of the internal heat exchanger, except that instead of two refrigerant fluid sides, there is only one refrigerant flow and the secondary fluid is air. The gas cooler refrigerant is assumed to always be supercritical fluid. The gas cooler conservation of refrigerant mass and energy are the same as the internal heat exchanger (Equations 2.14-2.15). The conservation of wall energy is modified to include the heat transfer from the air resulting in Equation 2.65.

$$\left(mc_p\right)_{w,cv} \dot{T}_{w,i} = A_{surf,cv}\alpha_{r,i}\left(T_{r,i} - T_{w,i}\right) + A_{surf,cv}\alpha_a\left(T_a - T_{w,i}\right) \tag{2.65}$$

The equations describing the heat transfer to the air were previously described with Equations 2.48-2.50.

2.1.4 System Performance

To build an entire vapor compression cycle in simulation, each component model is connected and refrigerant states are passed between adjacent components. The system behavior is verified by applying step inputs and step disturbances to the system.

First, the impact of increasing the compressor speed and valve opening (Figure 2.4) are verified. Dynamic outputs of interest are the pressures (evaporator and gas cooler), evaporator air outlet temperature, and cooling capacity. Compressor speed and valve opening are controllable inputs that directly impact the VCS pressures and the mass flow rate of the refrigerant through the cycle. The evaporator pressure and refrigerant flowrate both impact the evaporator air outlet temperature and cooling capacity. Evaporator pressure and refrigerant saturation temperature increase and decrease jointly. If the evaporator pressure and saturation temperature increase, then there is a smaller temperature differential between the air inlet temperature and the refrigerant temperature, thus having a decreasing effect on the cooling capacity. Additionally, increased refrigerant flowrate will increase cooling capacity and decreased flowrate will decrease cooling capacity. The results of the step change in compressor speed and valve opening are shown in Figure 2.5. When the valve is opened, the evaporator pressure increases (negative impact on cooling capacity), and simultaneously the refrigerant flow rate increases (positive impact on cooling capacity). In this case, the cooling capacity experiences a net increase. Next, the compressor speed increases, which increases the pressure ratio of the system, thereby decreasing the evaporator pressure (positive impact on cooling capacity) while increasing the refrigerant mass flow rate (positive impact on cooling capacity). As expected, the cooling capacity increases significantly and the evaporator air outlet temperature decreases. These results match the open- loop behavior of simulation results of [31] and experimental data from [32].

Second, the impact of increasing a disturbance is verified. The gas cooler inlet air temperature is stepped (Figure 2.6) and the dynamic responses of the pressure, evaporator air outlet temperature and cooling capacity are observed in Figure 2.7. The increase in gas cooler inlet air temperature shifts the pressures of the evaporator and gas cooler pressure in the positive direction. The increase in evaporator temperature has a negative impact on cooling capacity as previously discussed. Since there is no change in the refrigerant mass flow rate or flowrate of air across the evaporator, the net impact is a reduction in cooling capacity and increased evaporator air outlet temperature. The simulation results of the impact of the gas cooler inlet air temperature are supported by experimental data in [19].

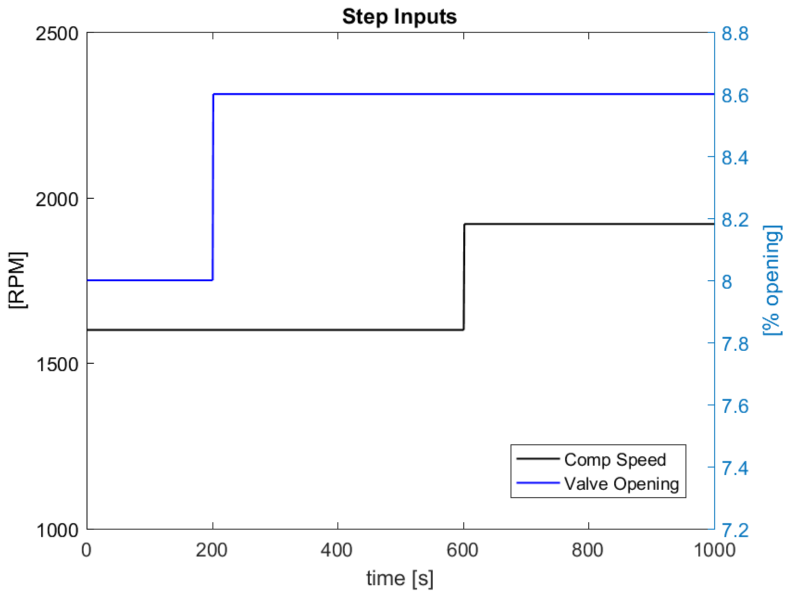

Figure 2.4 Step inputs to compressor and valve for open-loop verification of transcritical VCS

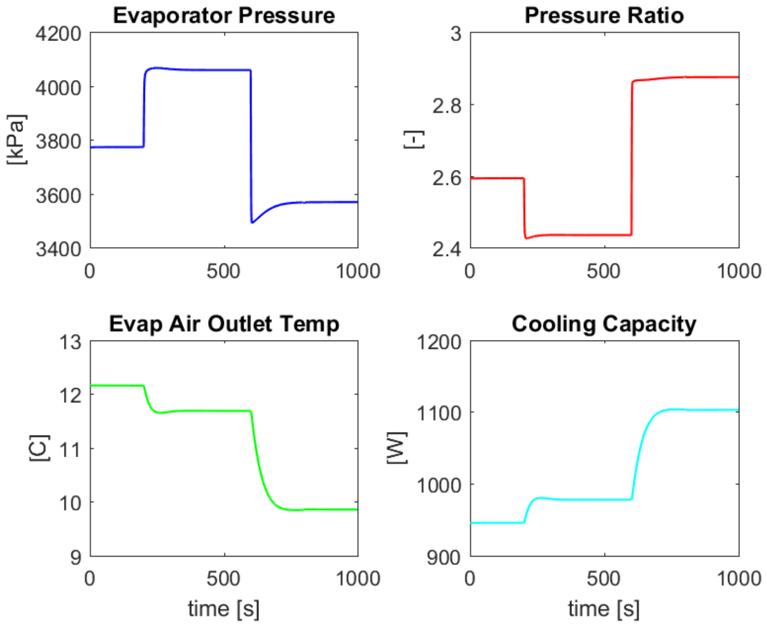

Figure 2.5 Selected VCS outputs’ dynamic responses to step inputs of Figure 2.4

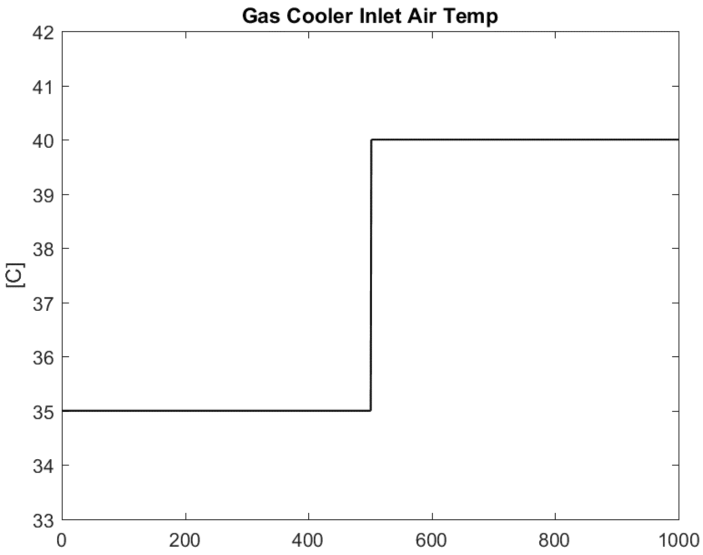

Figure 2.6 Step disturbance of gas cooler inlet air temperature for open-loop verification of transcritical VCS

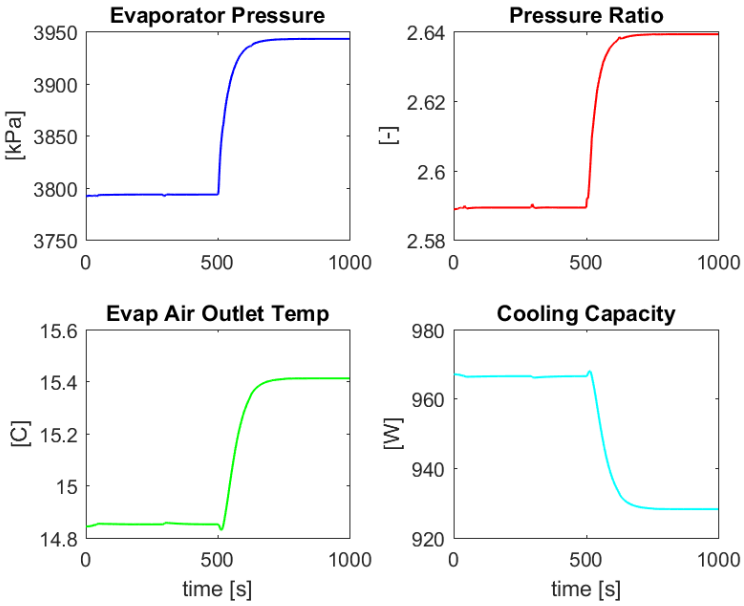

Figure 2.7 Selected VCS outputs' dynamic responses to step disturbances of Figure 2.6

2.2 Battery Pack Modeling

The goal of this section is to develop a battery pack model that captures both electrical and thermal behavior for use in control design. Electrochemical and equivalent circuit are the main methods for modeling cell electrical behavior and there are tradeoffs between complexity and computational load. Electrochemical (first principle) models represent transport, kinetic and thermodynamic phenomena with a set of nonlinear partial differential equations [33]. These models provide accuracy, but often contain a large set of unknown parameters and are computationally heavy. As noted by [34], this makes them unsuitable for control applications. Equivalent circuit models use a network of voltage sources, resistors and capacitors to describe the cell behavior. The dual-polarization (DP) model has shown to be an accurate equivalent circuit model and identified parameters are available for an A123 26650 $LiFePO_4$ cell [34]. [35] found that the parameters are dependent on both state of charge and temperature of the cell. Likewise, heat generation is dependent on the electrical state. Therefore, it is necessary to have a thermal model coupled with the electrical model (Figure 2.8).

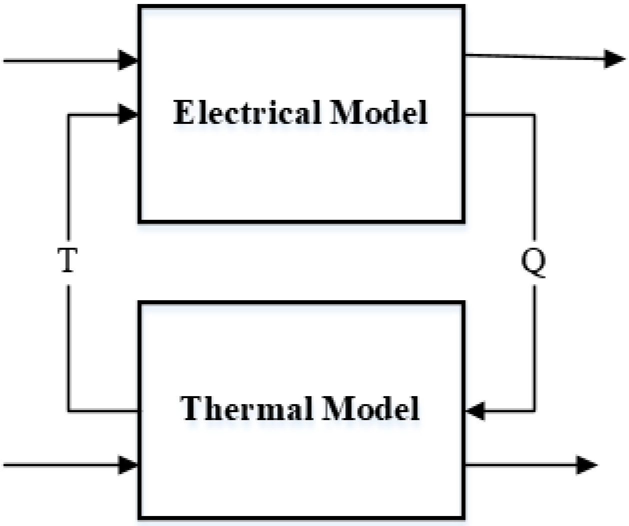

Figure 2.8 Coupling between cell electrical and thermal models. Q: heat generation, T: cell mean temperature. Adapted from [34]

Local heat generation within the cell is dependent on activation, concentration and ohmic losses resulting in a complex expression [36]. A simplified form, that neglects ohmic losses, can represent the local heat generation and be coupled with the DP electrical model.

2.2.1 Electrical Model

The dual polarization equivalent circuit is shown in Figure 2.9. It consists of an open-circuit voltage source, internal resistance and two RC pairs. One RC pair represents a fast polarization dynamic and the other represents a slow polarization dynamic.

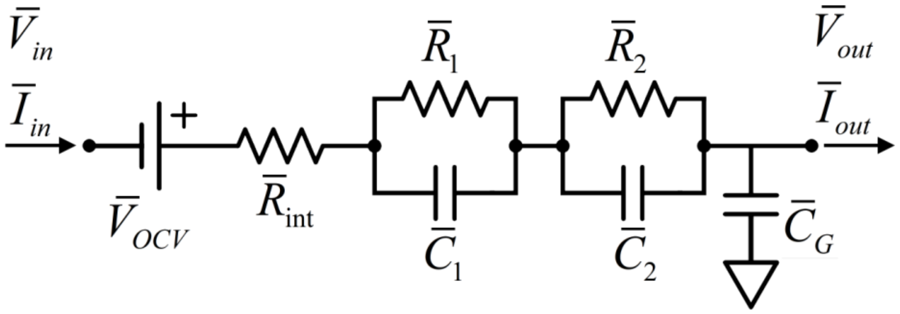

Figure 2.9 Dual polarization equivalent circuit with ground capacitance. Reprinted from [37]

In order to allow the cell model to be electrically modular the output voltage of the cell is made to be a state governed by Equation 2.66. The ground capacitance C_G is assumed to be very small (orders of magnitude smaller than the fastest system dynamic) so that it does not interfere with the other system dynamics. The input current is derived from Kirchoff's Voltage Law applied to Figure 2.9 (Equation 2.67). The state of charge (SOC) is defined as the cumulative current drawn from the battery relative to the battery capacity. Therefore, the time derivative is represented by Equation 2.68. The voltage dynamic of the RC pairs is governed by Equations 2.69-2.70 derived from Kirchoff's Current Law.

$$\bar{C}_G\dot{\bar{V}}_{out} = \bar{I}_{in} - \bar{I}_{out} \tag{2.66}$$

$$\bar{I}_{in} = \frac{1}{\bar{R}_{\text{int}}}\left(\bar{V}_{ocv} + \bar{V}_{in} - \bar{V}_{out} - \bar{V}_1 - \bar{V}_2\right) \tag{2.67}$$

$$S\dot{O}C = \frac{-\bar{I}_{in}}{\beta} \tag{2.68}$$

$$\dot{\bar{V}}_1 = \frac{-\bar{V}_1}{\bar{R}_1\bar{C}_1} + \frac{\bar{I}_{in}}{\bar{C}_1} \tag{2.69}$$

$$\dot{\bar{V}}_2 = \frac{-\bar{V}_2}{\bar{R}_2\bar{C}_2} + \frac{\bar{I}_{in}}{\bar{C}_2} \tag{2.70}$$

The inputs to the system are the input voltage and demanded current and the states are the RC-pair voltages, the output voltage, and state of charge (Equations 2.71-2.72).

$$u = \begin{bmatrix} \bar{V}_{in} & \bar{I}_{out} \end{bmatrix}^T \tag{2.71}$$

$$x = \begin{bmatrix} \bar{V}_1 & \bar{V}_2 & \bar{V}_{out} & SOC \end{bmatrix}^T \tag{2.72}$$

2.2.2 Thermal Model

The cell is modeled as a 2^{nd} order system with core and surface temperature states. The core generates heat and then heat is transferred to the cell surface by conduction. Additionally, cell-to-cell conduction and convection to a cooling fluid is included in the thermal circuit (Figure 2.10). The cell internal heat generation, dependent on electrical current and voltages, is described by Equation 2.73, which characterizes joule heating, energy dissipation from electrode over potentials, and entropic heating. Conservation of energy is analyzed for the temperature states of the cell and described by Equations 2.74-2.76.

$$Q_{gen} = \bar{I}_{in}\left(\bar{V}_{ocv} - \bar{V}_T\right) - \bar{I}_{in} T_m \frac{\partial U}{\partial T_m} \tag{2.73}$$

$$C_{c,i}\dot{T}_{c,i} = Q_{gen,i} + \frac{T_{surf,i} - T_{c,i}}{R_{\text{int}}} \tag{2.74}$$

$$C_{surf,i}\dot{T}_{surf,i} = \frac{T_{surf,i-1} + T_{surf,i+1} - 2T_{surf,i}}{R_{ext}} + \frac{T_{c,i} - T_{surf,i}}{R_{\text{int}}} + \frac{T_{fl,i} - T_{surf,i}}{R_u} \tag{2.75}$$

$$T_{fl,i} = T_{fl,i-1} + \frac{T_{surf,i} - T_{fl,i-1}}{R_{u,i}C_{fl,i}} \tag{2.76}$$

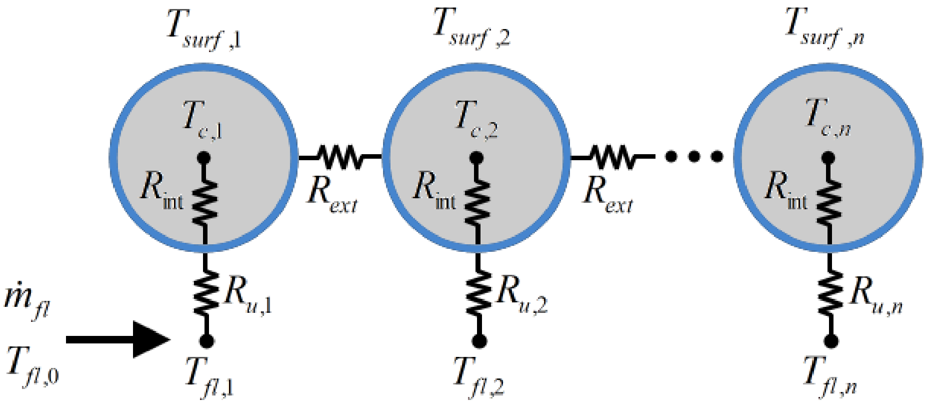

Figure 2.10 Thermal model for n **cells. Reprinted from** [37]

2.2.3 Model Reduction

The cell model derived in the previous two sections has 7 states. A battery pack large enough for a battery electric vehicle would require thousands of cells resulting in a model with an excessively large number of states. To reduce the number of states, a module model is developed that includes the following assumptions:

1. The cells have the same initial conditions
2. There exists no thermal gradients in the module (lumped temperature)

The number of cells in series and parallel, $\bar{N}_s$ and $\bar{N}_p$ respectively, are additional parameters defined for the module model. The output voltage dynamic is based on the total current through the module as seen in Figure 2.11 and described by Equation 2.77. The cell dynamics governing the state of charge, RC voltages, and heat generation is based on the current flowing through each cell described by Equation 2.78.

Electrical Current through Module

$$\bar{I}_{in} = \frac{\bar{N}_p}{\left(\bar{N}_s \bar{R}_{\mathrm{int}}\right)}\left(\left(\bar{N}_s \bar{V}_{ocv}\right) + \bar{V}_{in} - \bar{V}_{out} - \left(\bar{N}_s \bar{V}_1\right) - \left(\bar{N}_s \bar{V}_2\right)\right) \tag{2.77}$$

Electrical Current through each Row

$$\bar{I}_{in} = \frac{1}{\left(\bar{N}_s \bar{R}_{\mathrm{int}}\right)}\left(\left(\bar{N}_s \bar{V}_{ocv}\right) + \bar{V}_{in} - \bar{V}_{out} - \left(\bar{N}_s \bar{V}_1\right) - \left(\bar{N}_s \bar{V}_2\right)\right) \tag{2.78}$$

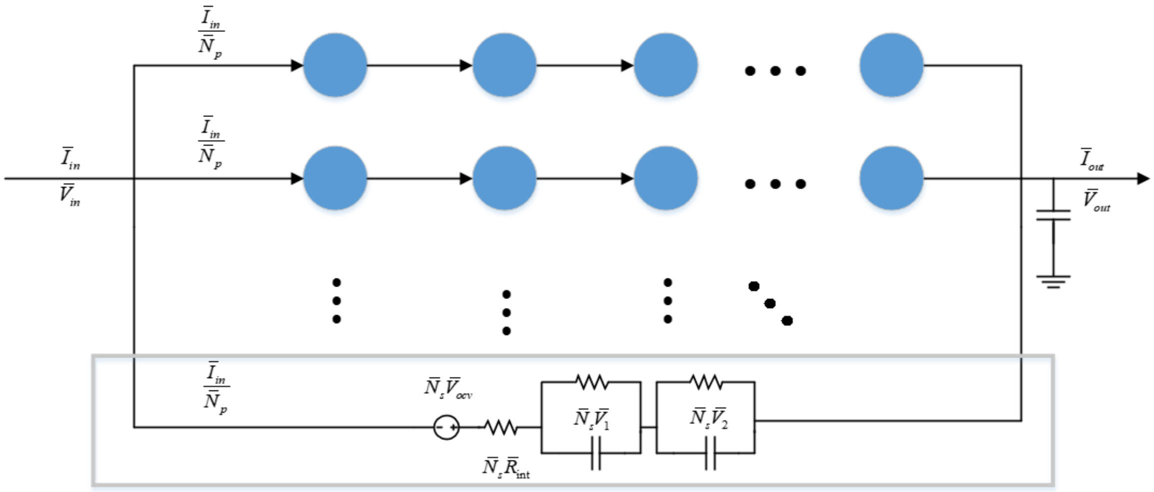

Figure 2.11 Representation of electrical circuit of a battery module

Lastly, the equation for the convective heat transfer from the module to the cooling fluid is scaled to account for the number of cells (2.79).

$$T_{fl,i} = T_{fl,i-1} + \frac{\bar{N}_s \bar{N}_p (T_{surf,i} - T_{fl,i-1})}{R_{u,i} C_{fl,i}} \tag{2.79}$$

2.2.4 System Performance

The model verification for the battery is done in two steps: 1) verification of state behavior with free convection, and 2) verification of state behavior with forced convection. To verify the model captures the dynamic behavior of the battery temperature and voltage, a battery module, was discharged at different rates in simulation and compared to available data in literature. The simulated battery module consists of a matrix of 30 cells in parallel and 14 cells in series. As mentioned in the modeling description, it is assumed that each cell is thermally and electrically uniform. Each cell has a nominal voltage of 3.3 V and a capacity of 2.3 Ah, therefore, the module has a total capacity of about 70 Ah. The module is discharged at 0.5C, 1C, 3C, and 5C (35 A, 70 A, 210 A, 350 A respectively) to match the experiment conducted by [38]. The simulation is carried out until the depth of discharge is about 90% (state of charge is 10%). The average voltage of each cell is plotted in Figure 2.12 and the average temperature of each cell is plotted in Figure 2.13. The data from the simulations closely matches the data of [38], in terms of curvature and magnitude. However, it should be noted that [38] provides data for an Li[NiMnCo]O_2 pouch cell, in contrast to the $LiFePO_4$ cylindrical cell modeled in this thesis. Therefore, it is not expected that the results will directly overlap. But, it is clear that the models developed in this work capture the same behavior of a physical battery.

Next, the behavior of the battery module with forced convection is verified. Figure 2.14 shows the cell surface and core temperature states, and cell voltage as a result of a step input to the battery fan speed (increase from 0% fan speed to 80%). As expected, the surface temperature responds faster to the increased cooling, and the core temperature cools on a slower time scale due to its larger thermal capacitance. Furthermore, the module voltage decreased as a result of the decreased average cell temperature when the cooling was applied.

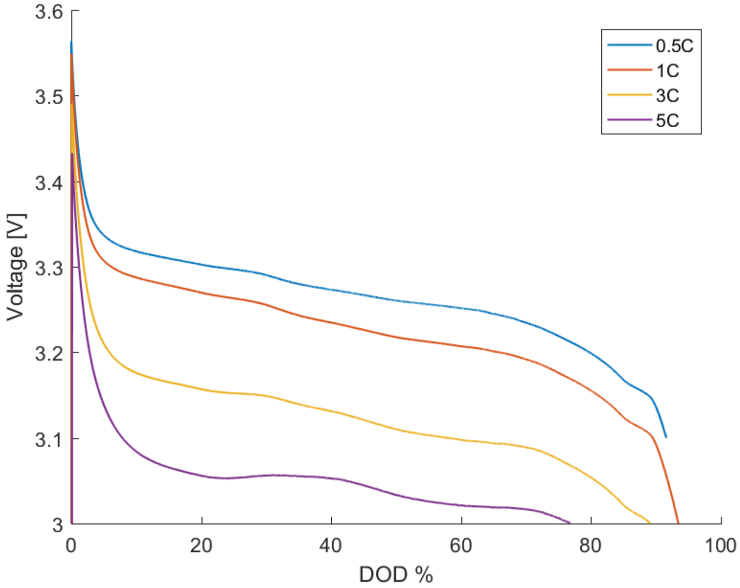

Figure 2.12 Battery module output voltage relative to discharge rate

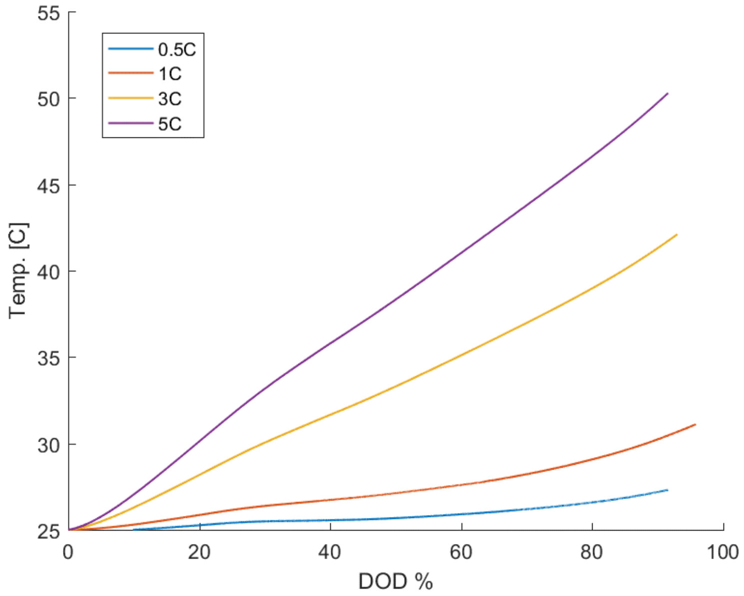

Figure 2.13 Battery module output average temperature relative to discharge rate

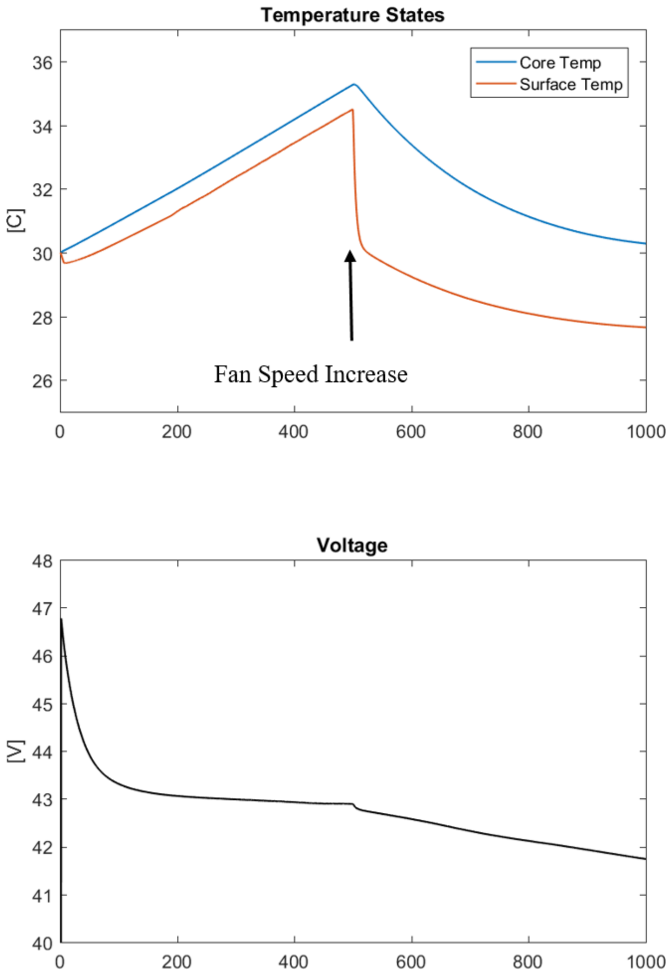

Figure 2.14 Battery module temperature and voltage states in response to stepped battery fan speed

2.3 Cabin Modeling

The cabin is modeled with consideration to conservation of energy with respect to the external and internal heat loads. The following assumptions are made to simplify the derivation [39]:

1. The air within the cabin is well mixed and uniform (lumped parameters)
2. There is no mass accumulation within the cabin
3. Radiative heat transfer between interior surfaces are negligible

4. Vehicle windows are transparent and all other surfaces are opaque
5. Surfaces can be assumed horizontal or vertical with incident solar radiation broken down into horizontal and vertical components

With these assumptions, the cabin temperature dynamic of the cabin air is governed by Equation 2.80 that includes heat loads from solar radiation through windows, the vapor compression system, the people in the cabin, air leakages/infiltration from the ambient air, the conduction through exterior surfaces of the vehicle, and heat exchange from the base of the vehicle. The base of the vehicle accounts for the thermal capacitance of the interior elements of the vehicle. Furthermore, the base exhibits its' own temperature dynamic described by Equation 2.81. Each heat load is defined in Table 2.2.

$$C_{a,cab}\dot{T}_{a,cab} = Q_{solar} + Q_{cool} + Q_{gen} + Q_{leak} + Q_{surf} + Q_{base} \tag{2.80}$$

$$C_{base}\dot{T}_{base} = \alpha_{base} Q_{solar} - Q_{base} \tag{2.81}$$

Table 2.2 Vehicle heat loads

Heat Load	**Equation**
Q_{solar}	$Q_{solar} = \gamma \bar{\tau}_{windows} q''_{solar} A_{windows}$
Q_{cool}	$Q_{cool} = \dot{m}_{a,evap} c_{p,a} (T_{a,evap,out} - T_{a,cab})$
Q_{gen}	$Q_{gen} = 108 * occupancy$
Q_{leak}	$Q_{leak} = \dot{m}_{a,leak} c_{p,a} (T_{\infty} - T_{a,cab})$
Q_{surf}	$Q_{surf} = \alpha_{surf} A_{surf} (T_{surf,\mathrm{int}} - T_{a,cab})$
Q_{base}	$Q_{base} = h_{base} A_{base} (T_{base} - T_{a,cab})$

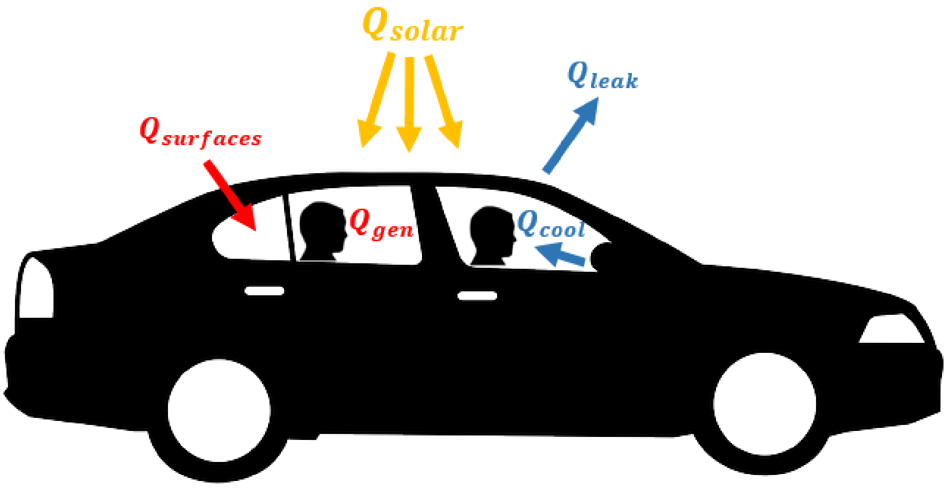

Figure 2.15 Heat loads on vehicle cabin considered in model. Reprinted from [37]

2.3.1 System Performance

The cabin model is verified by analyzing the cabin temperature when different cooling loads and ambient conditions are applied, while all other loads are held constant. Figure 2.16 shows the cabin temperature decreases with increasing cooling loads (magnitude). Figure 2.17 verifies that with increasing ambient temperature and a constant cooling load, the cabin temperature will remain at an elevated temperature. The cabin temperature responds like a first order system, which is to be expected from Equation 2.80.

The cabin model thermal behavior is verified with step changes in controllable inputs and external disturbances. Figure 2.18 shows the cabin air temperature resulting from a step change in the supply temperature and fan speed. The supply temperature increased from 18 to 19.2 C at 300 seconds and the fan speed increased from 50 to 80% at 600 seconds. A warmer supply temperature supplies less cooling and increased fan speed increases cooling. Figure 2.19 shows the cabin air temperature resulting from a step changes in solar radiation and wind speed. The solar radiation doubled from 1200 to 2400 W/m^2 and the relative wind speed increased from an average value of 15 m/s to 20 m/s. Increased solar radiation increases the heat load on the cabin, thus increasing the cabin air temperature. Wind speed increases the infiltration rate of ambient air into the cabin, thereby increasing the cabin temperature.

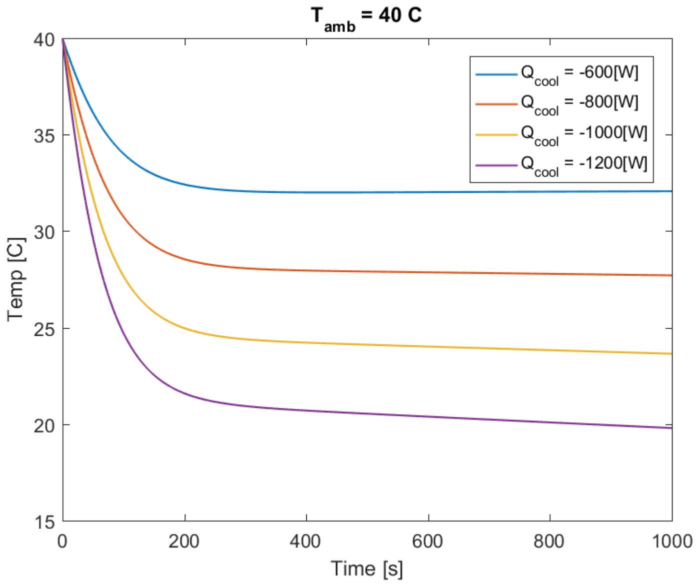

Figure 2.16 Cabin temperature given different cooling loads applied with an ambient temperature of 40 C

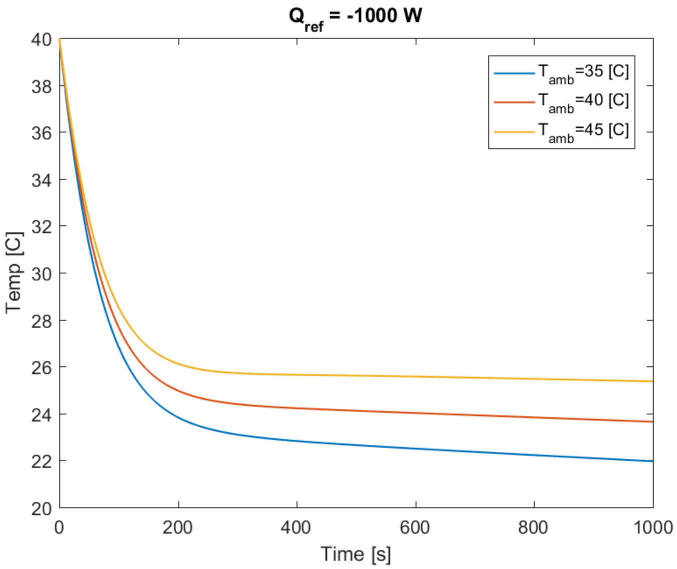

Figure 2.17 Cabin temperature given different ambient conditions with a constant applied cooling load

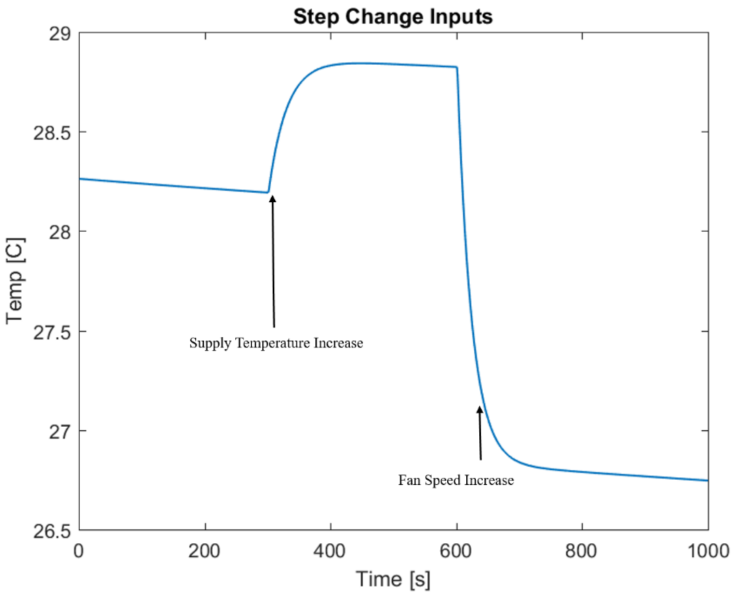

Figure 2.18 Step change in supply air temperature from evaporator followed by step change in fan speed

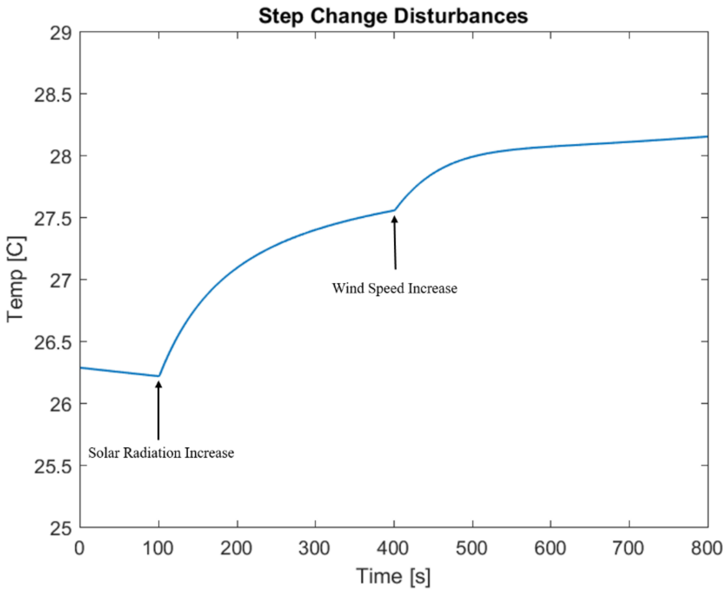

Figure 2.19 Step change in solar radiation followed by step change in wind speed

Chapter 3 System Simulation

Chapter 3 builds upon Chapter 2 and explores how the subsystem models can be parameterized and linked to build up a variety of thermal management systems. Then, the parameters for the sub-systems are defined that will be used in the remainder of this work. A modeled air-cooled cabin, air-cooled battery pack configuration will be described and the behavior verified based on outputs from open-loop simulations. This design will be used in Chapters 4 and 5 for control design and analysis. Lastly, the open-loop simulation outputs for a modeled air-cooled cabin, liquid-cooled battery pack configuration will be discussed to show the ability of the models to simulate liquid cooled systems.

3.1 Architecture design

The modular and scalable modeling approach allows for cooling system architecture design. Previous sections focused on the internal signal communication of the VCS (i.e. refrigerant states $P, h, \dot{m}$) and battery (i.e. Q_{gen}, T_m). But, externally there are user defined/controller inputs and inputs that are output signals from another subsystem. The way in which internal and external signals are connected dictate the form of the architecture design. Most air-cooled battery packs use recirculated cabin air [40] as shown in Figure 3.1. However, other air-cooled designs may offer more degrees of freedom for controls such as multi-evaporator systems (Figure 3.2) where cooling applied to each load is controlled by actuation of fans or valves. Additionally, liquid-cooled battery packs have the potential to provide better cooling performance due to increased heat transfer coefficients. Liquid cooling requires an additional heat exchanger (liquid-to-liquid) for a secondary cooling loop to the battery; an example is shown in Figure 3.3. Each of these configurations and more can be simulated with the models previously derived.

Table 3.1 External inputs and outputs and adjustable parameters for each subsystem

	External Inputs	External Outputs	Parameters
VCS			
Compressor	ω		Geometry, efficiency maps
Valve	z		Flow coefficient, aperture maps
Internal Heat Exchanger			Geometry, initial conditions, refrigerant properties, wall properties
Gas Cooler	$\dot{m}_{a,gc}, T_{a,gc,in}$	$T_{a,gc,out}$	Geometry, initial conditions, refrigerant properties, air properties, wall properties
Evaporator	$\dot{m}_{a,evap}, T_{a,evap,in}$	$T_{a,evap,out}$	Geometry, initial conditions, refrigerant properties, air properties, wall properties
Battery			
Module	$\bar{V}_{in}, \bar{I}_{out}, \dot{m}_{fl,in}, T_{fl,in}$	$\bar{V}_{out}, T_c, T_{surf}, T_{fl,out}$	Battery parameters, initial conditions, coolant properties, module parameters

Table 3.1 (cont.)

Cabin	$\dot{m}_{a,evap}, T_{a,evap,out}, v_{traction}$	$T_{a,cab}$	Material properties (car body and windows), vehicle dimensions, initial conditions, ambient conditions

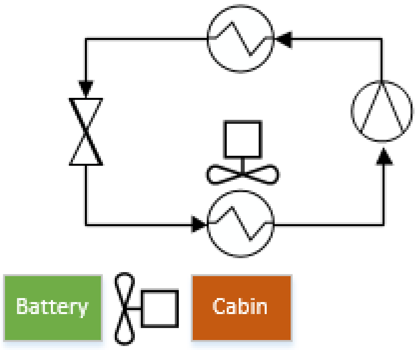

Figure 3.1 Representation of an air-cooled battery pack

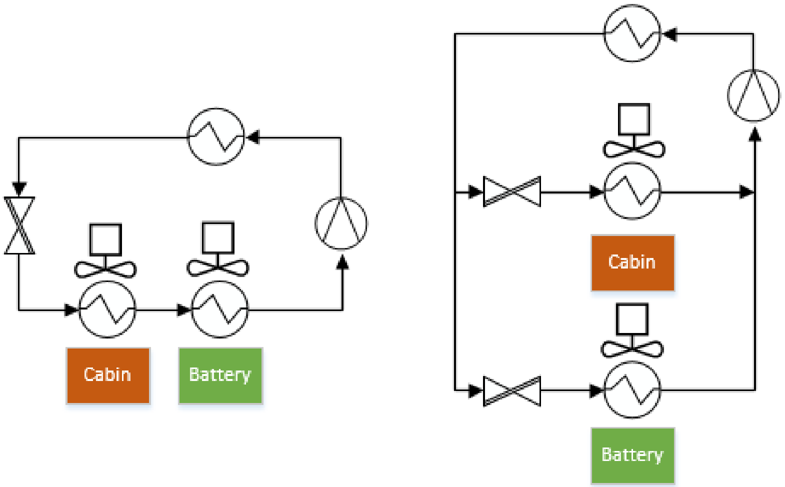

Figure 3.2 Multi-evaporator air-cooled battery pack architectures

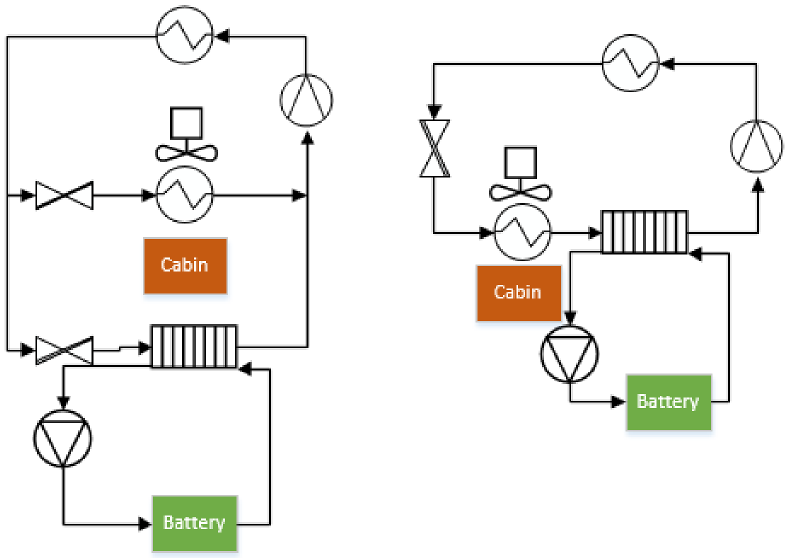

Figure 3.3 Multi-evaporator liquid-cooled battery pack architectures

3.2 Simulation Parameters

The parameters of the VCS, battery pack and cabin will remain consistent across all simulations discussed in the remainder of this thesis. The vehicle dimensions and material properties are estimated for a four door compact vehicle (Table 3.2). The transcritical VCS heat exchanger and compressor geometry is estimated from a prototype CO_2 mobile air conditioning system (MAC2R744) given in Table 3.3 [18]. The battery electrical parameters are from charge-discharge data of an A123-22650 cylindrical Li-Ion 3.3 V cell provided by [34], and vary as a function of cell average temperature and state of charge (Figures 3.4-3.7). The cell geometry and thermal parameters are listed in Table 3.4.

The battery pack consists of eight modules in series. Each module contains a matrix of 30 cells in parallel and 14 sells in series. Therefore, the entire battery pack contains 3360 cells, resulting in 370 nominal voltage and 138 Ah capacity, which is in the range of BEVs on the market. An internal resistance adjustment factor is used as a tuning parameter to capture the increased internal resistance of aged cells, and account for heat sources that are neglected in this work, such as waste heat from nearby electrical components.

Table 3.2 Vehicle parameters

Component	Parameter	Units	Value
Material Properties	Absorptivity of body		0.26
	Emissivity of body		0.9
	Thermal diffusivity of windshield	m^2/s	3.40E-07
	Thermal conductivity of windshield	W/(m*K)	1.4
	Thermal diffusivity of side window	m^2/s	3.40E-07
	Thermal conductivity of side window	W/(m*K)	1.4
	Absorptivity of window		0.2
	Emissivity of window		0.9
	Transmittance of window		0.45
Vehicle Dimension	Volume of cabin	m^3	3.11
	Length of roof	m	1.8
	Width of roof	m	1.1
	Length of wall	m	1.5
	Width of wall	m	0.35
	Length of windshield	m	0.63
	Width of windshield	m	1.3
	Thickness of windshield	m	6.00E-03
	Length of side window	m	1.45
	Width of side window	m	0.29
	Thickness of side window	m	6.00E-03
Traction Power	Drag Coefficient		0.28
	Rolling Resistance		0.009
	Frontal Area	m^2	2.29
	Mass	kg	1600
	Average slope	degrees	5
	Average wind speed	m/s	15

Table 3.3 Transcritical VCS parameters

Component	Parameter	Units	Value
Evaporator	Hydraulic Diameter	m	1.092E-03
	Length of One Refrigerant Pass	m	2.285
	Number of Parallel Passes		4
	Air Side Cross Sectional Area	m^2	0.0315
	Air Contact Surface Area	m^2	4.4
	Refrigerant Surface Area	m^2	0.0314
	Refrigerant Pass Cross Sectional Area	m^2	9.37E-07
	Mass	kg	2.458
	Specific Heat	kJ/(kg*K)	0.879
Internal Heat Exchanger	Hydraulic Diameter HP Side	m	6.00E-03
	Hydraulic Diameter LP Side	m	1.15E-02
	Length of One Refrigerant Pass	m	2
	Refrigerant Surface Area HP Side	m^2	0.0396
	Refrigerant Surface Area LP Side	m^2	0.0858
	Cross Sectional Area HP Side	m^2	2.83E-05
	Cross Sectional Area LP Side	m^2	4.53E-05
	Mass	kg	0.162
	Specific Heat	kJ/(kg*K)	0.91

Table 3.3 (cont.)

Gas Cooler	Avg. Number of Passes		1
	Hydraulic Diameter	m	6.35E-04
	Internal Volume	m^3	1.80E-04
	External Surface Area	m^2	7.09
	Length of One Refrigerant Pass	m	1.09
	Avg. Number of Microchannel Plates		65
	Number of Parallel Passes		1
	Number of Microchannel Ports per Plate		4
	Mass	kg	3.28
	Specific Heat	kJ/(kg*K)	0.879
Two Fluid Plate Evaporator	Number of Primary Fluid Channels		30
	Primary Hydraulic Diameter	m	2.54E-03
	Plate Length	m	0.325
	Primary Cross Sectional Area	m^2	2.85E-04
	Primary Surface Area	m^2	0.0137
	Number of Secondary Fluid Channels		30
	Secondary Hydraulic Diameter	m	2.54E-03
	Secondary Cross Sectional Area	m^2	2.85E-04
	Secondary Surface Area	m^2	1.37E-02
	Mass of one plate	kg	0.12
	Specific Heat	kJ/(kg*K)	0.385
Compressor	Displacement Volume	m^3	5.00E-07

Table 3.4 Battery pack parameters

Component	Parameter	Units	Value
Cell	Lumped Cell Core Heat Capacity	J/K	62.7
	Lumped Cell Surface Heat Capacity	J/K	4.5
	Conduction Resistance	K/W	1.94
	Battery Capacity	Ah	4.6
	Internal Resistance Adjustment Factor		6
Module	Number of Cells in Parallel		30
	Number of Cells in Series		14
Air Cooling	Number of Cooling Channels		150
	Equivalent Diameter of Cooling Channels	m	0.0254
	Coolant Specific Heat	kJ/(kg*K)	1.007
	Coolant Dynamic Viscosity	(N*s)/m^2	1.98E-05
	Thermal conductivity boundary layer	W/(m*K)	2.60E-02
	Coolant density	kg/m^3	1.204
Glycol75-Water25 Cooling	Number of Cooling Channels		1
	Equivalent Diameter of Cooling Channels	m	0.0254
	Coolant Specific Heat	kJ/(kg*K)	3.049
	Coolant Dynamic Viscosity	(N*s)/m^2	1.07E-02
	Thermal conductivity boundary layer	W/(m*K)	0.277
	Coolant density	kg/m^3	1030

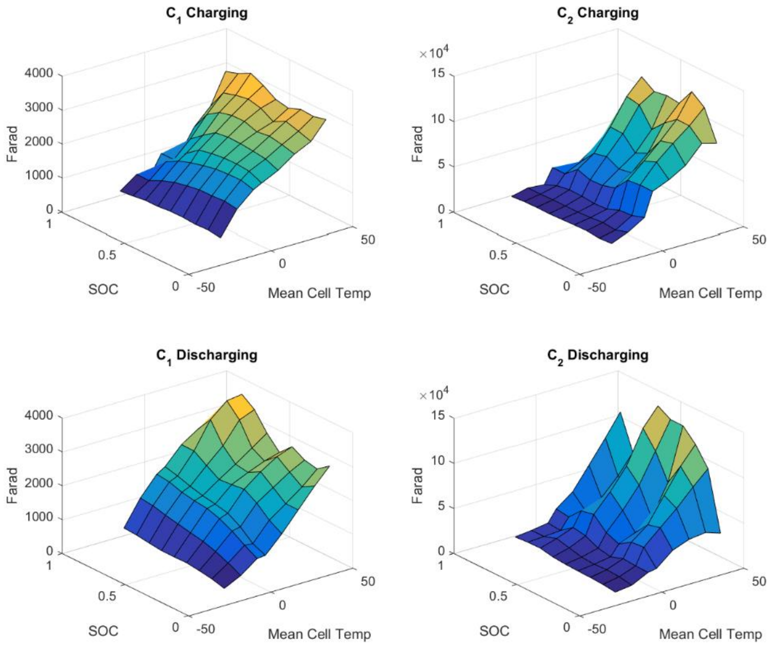

Figure 3.4 Capacitance data for charging and discharging A123-26650 3.3 V cell

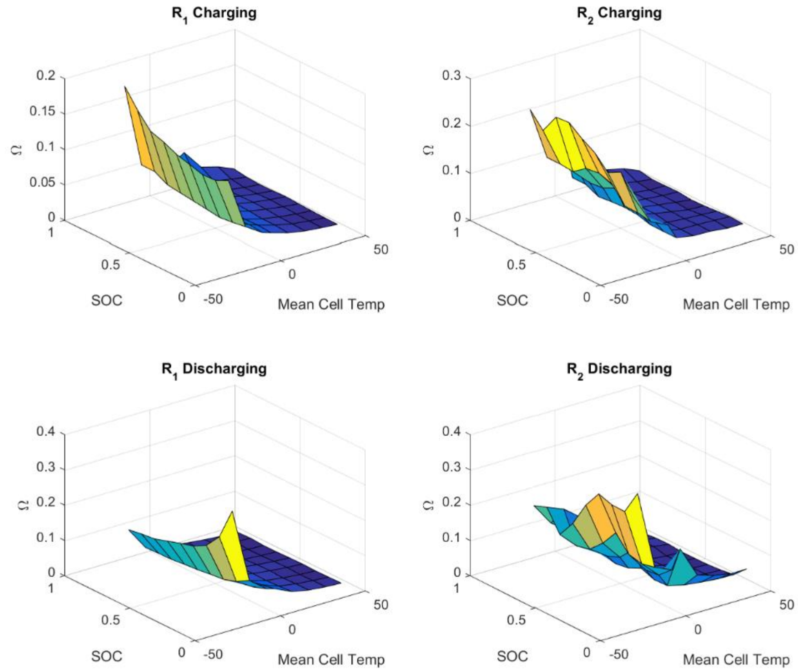

Figure 3.5 Resistance data for charging and discharging A123-26650 3.3 V cell

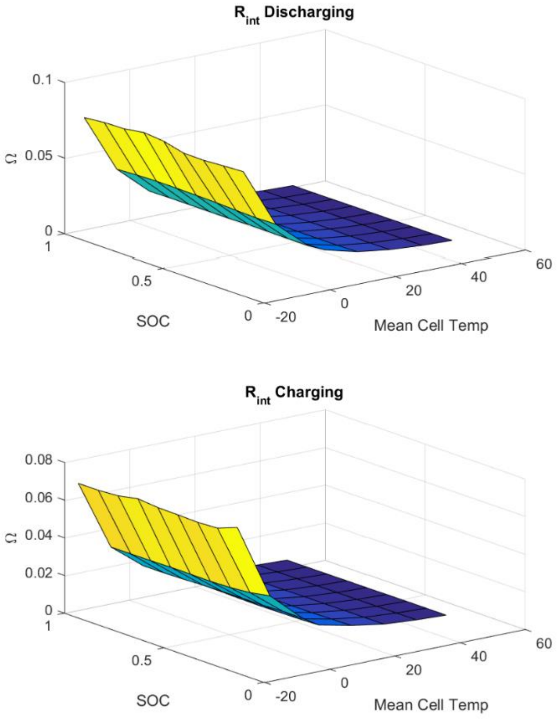

Figure 3.6 Internal resistance data for charging and discharging A123-26650 3.3 V cell

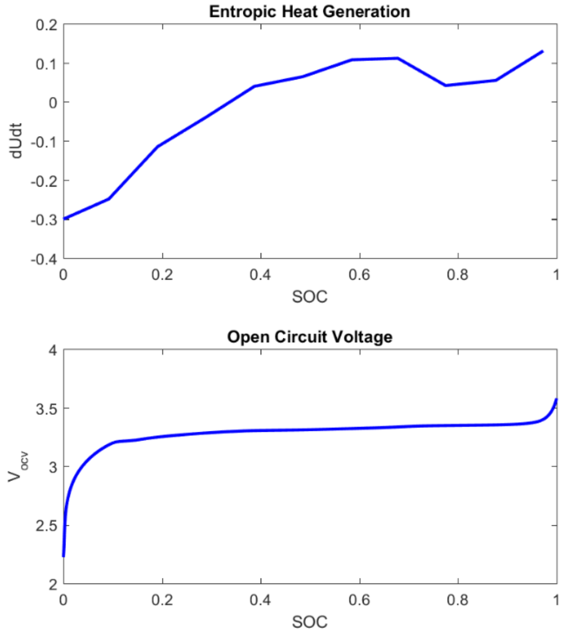

Figure 3.7 Entropic heat generation term and open circuit voltage as function of SOC

3.3 Power Consumption

The electrical loads on the battery pack considered in this work are the power consumption from traction, the VCS compressor, and pump and fan actuators. Furthermore, the battery is assumed to operate at a constant voltage, allowing the current demand to be defined by Equation 3.1.

$$\bar{I}_{out} = \frac{\bar{P}_{traction} + \bar{P}_{comp} + \bar{P}_{fan} + \bar{P}_{pump}}{\bar{V}_{pack,const}} \tag{3.1}$$

3.3.1 Traction Power

The traction power of the vehicle is calculated with a force balance that considers acceleration and resistive forces i.e. rolling resistance, wind drag, and gradient resistance [41].

$$F_{traction} = f_m m\dot{v} + mgc_{rr}\cos\theta + \frac{1}{2}\rho A c_D \left(v - v_{wind}\right)^2 + mg\sin\theta \tag{3.2}$$

f_m is the mass factor that relates rotational inertia to translational mass, c_{rr} the rolling resistance, and c_D the drag coefficient. The traction power is then $\bar{P}_{traction} = F_{traction} v$. Negative powers, resulting from deceleration greater than resistive forces, are used as regenerative braking. Regenerative braking charges the battery by converting the kinetic energy of the vehicle into electrical energy. No limits on regenerative braking are considered in this analysis. This work assumes an average gradient and average wind speed (combination of wind and vehicle speed). With a known velocity profile, the current profile can be calculated apriori if it is assumed that the battery pack voltage is approximately constant.

3.3.2 VCS Compressor Power

The compressor electrical power is the theoretical pump power divided by an assumed motor efficiency.

$$\bar{P}_{comp} = \frac{\dot{m}\Delta h_{comp}}{\eta_{mech}} \tag{3.3}$$

The compressor power is calculated at each time step of the simulation and then divided by the pack voltage to provide the current signal to the battery pack.

3.3.3 Fan Power

The evaporator and battery fan models are modified from data of an experimental system at the University of Illinois. The data provides a map of electrical power as a function of air mass flow rate. The maximum mass flow rate and power for the evaporator fan is 0.12 kg/s and 180 W, respectively. The data is scaled to approximate the mass flow rate and power consumption of a smaller fan for the battery pack. The maximum air mass flow rate and power for the battery fan is assumed to be 0.06 kg/s and 150 W, respectively. The electrical power is quadratic with respect to flowrate as shown in Figure 3.8. This power is calculated at each time step of the simulation and divided by the pack voltage.

3.3.4 Pump Power

The liquid pump is assumed to pump a maximum 5 GPM and can be commanded linearly within that region. The pump operates at 110 V and a maximum 1.2 A of current. The electrical power, calculated at each simulation time step is assumed quadratic with maximum value given by the produce of the operating voltage and maximum current.

$$\bar{P}_{pump} = \left(\frac{u}{100}\right)^2 * 110 * 1.2 \tag{3.4}$$

Note: u is a value 0-100 %. A simplified model like this is satisfactory for the purpose of calculating an approximated power associated with a flowrate. The pump is used in the secondary loop of the transcritical VCS for a liquid cooled battery pack. This power is calculated at each time step of the simulation and divided by the pack voltage.

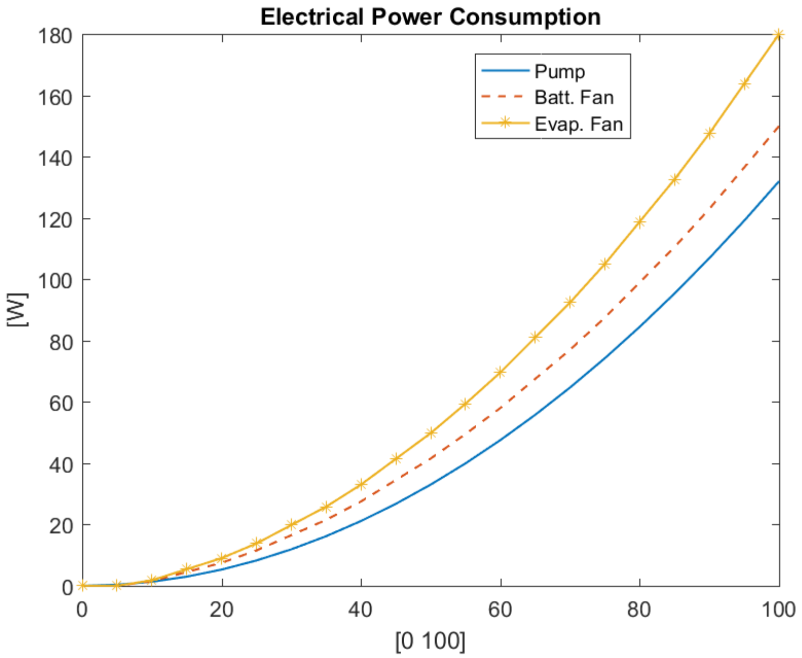

Figure 3.8 Pump and fan power curves

3.4 Sample Simulations

3.4.1 Air-cooled Cabin, Air-cooled Battery pack

The simulated air-cooled cabin and air-cooled battery pack configuration is shown in Figure 3.9. The vapor compression system cools supply air blown across the evaporator and into the cabin. A second fan blows cabin air across the battery pack. The battery pack provides electrical power for the vehicle traction, the two fans and the VCS compressor. It is assumed that the air entering the evaporator is 50% recirculated air from the cabin and 50% ambient air. Similar to Chapter 2, selected inputs are varied to verify the open-loop behavior of the entire system. The simulation inputs are summarized in Table 3.5. Battery temperature refers to the average temperature of the battery pack by taking the average of each modules surface and core temperatures.

$$T_{batt} = \frac{T_c^{mean} + T_{surf}^{mean}}{2} \tag{3.5}$$

Simulation 1 provides a set of constant actuator inputs, but the solar radiation load on the cabin doubles at 600 seconds and the current drawn from the battery pack increases from 100 to

150 Amps at 1200 seconds. The simulation outputs are shown in Figure 3.10. It is clear that in open-loop simulation, the cabin and battery temperatures are not resistant to disturbances. The impact of increasing the solar radiation is a cascading increase in the evaporator air outlet, cabin air, and battery temperatures. Additionally, the step increase in current impacts the rate of increase of mean battery pack temperature. The battery pack reaches temperatures close to 40 C (recall that optimal performance is between 15-35 C) because there is no adjustment made to the actuator commands to account for the disturbances. The battery pack state of charge decreases linearly and proportional to the magnitude of the current being discharged.

In Simulation 2 the fan speeds and valve opening are held constant in each iteration. The current drawn from traction is varied incrementally from 50 to 150 Amps. The compressor speed is varied incrementally from 1600 to 2000 RPM, resulting in 9 iterations. Figure 3.11 shows the results at 1200 seconds when the evaporator air outlet temperature and cabin temperature have achieved steady state. Data points are shown for each of the 9 tests and a curve was fitted to each data set to determine trends. It is verified that the output temperatures (evaporator, cabin, and battery) decrease with increasing compressor speed, as more cooling is provided. Furthermore, the evaporator outlet air temperature is the coolest, followed by the cabin and then battery pack, which matches the chosen configuration. Lastly, the simulation results show that the heat generated by the battery is largely coupled with the current being discharged. At the same cooling capacity to the cabin, the temperature of the battery pack is not managed as effectively at higher currents.

Simulation 3 demonstrates the impacts of increasing the evaporator fan and battery fan speed on the cabin temperature and battery pack mean temperature (Figure 3.12). Increasing the battery fan speed shows a larger decrease in battery average temperature. However, increasing the evaporator fan speed from 20 to 50 % shows increased cooling but not from 50 to 80%. Given this set of actuator inputs, the optimal fan speed is less than the maximum speed. There exists a tradeoff between the mass flow rate of air and the change in temperature of the air across the evaporator. At higher fan speeds, the air mass flow rate is greater, but the temperature is reduced less as it flows across the evaporator. Recall from Chapter 2 that the cooling provided to the cabin is proportional to both of these terms: $Q_{cool} = \dot{m}_{a,evap} c_{p,a} (T_{a,evap,out} - T_{a,cab})$.

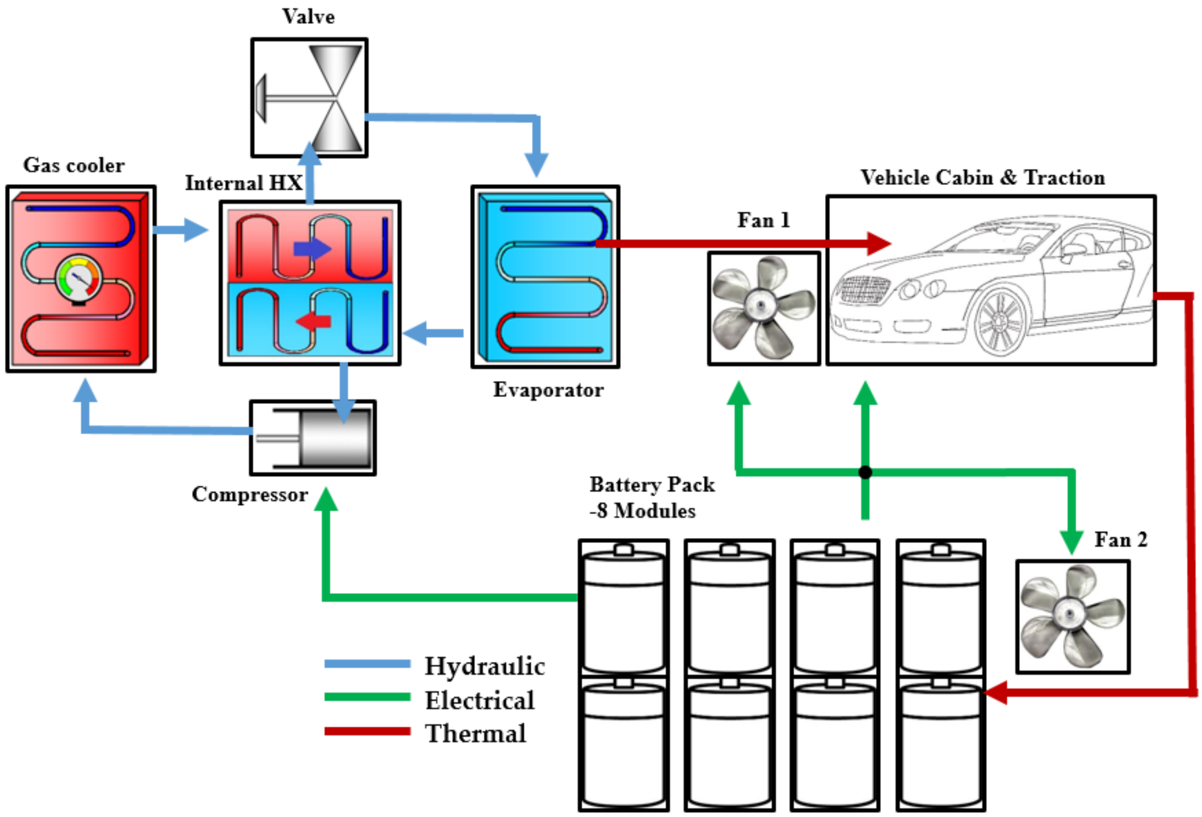

Figure 3.9 Air-cooled cabin, air-cooled battery pack system schematic

Table 3.5 Air-cooled cabin, air-cooled battery pack open-loop simulation inputs

	Inputs	**Figure**
Simulation 1	Fan 1 = 50%, Fan 2 = 10%, Valve = 8%, Comp = 1600 RPM Solar Irradiance step change $I_{traction}$ step change	**Fig. 3.10**
Simulation 2	Fan 1 = 50%, Fan 2 = 30%, Valve = 10% $I_{traction}$ = 50, 100, 150 A Comp = 1600, 1800, 2000 RPM	**Fig. 3.11**
Simulation 3	Comp = 1800 RPM, Valve = 10%, $I_{traction}$ = 150 A Fan 1 = 20, 50, 80%, Fan 2 = 20, 50, 80%,	**Fig. 3.12**

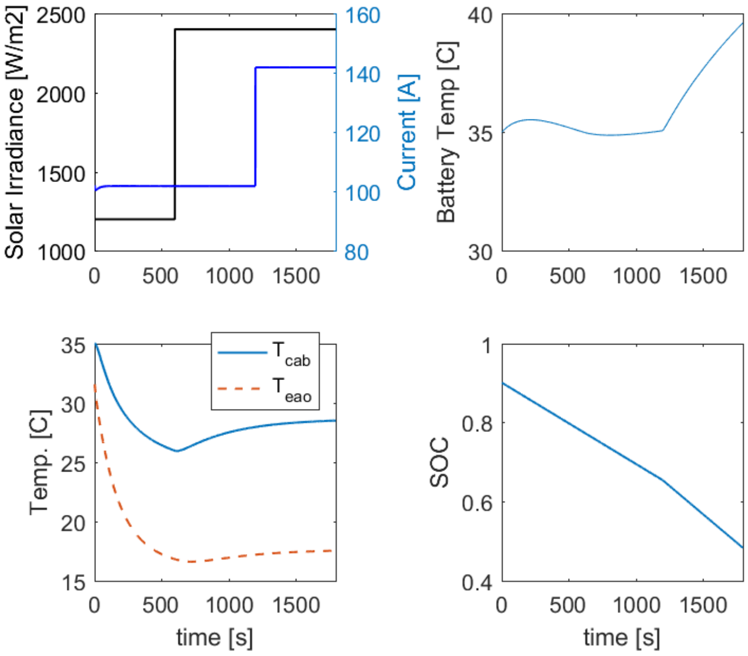

Figure 3.10 Selected outputs with ‘Simulation 1’ inputs of Table 3.5

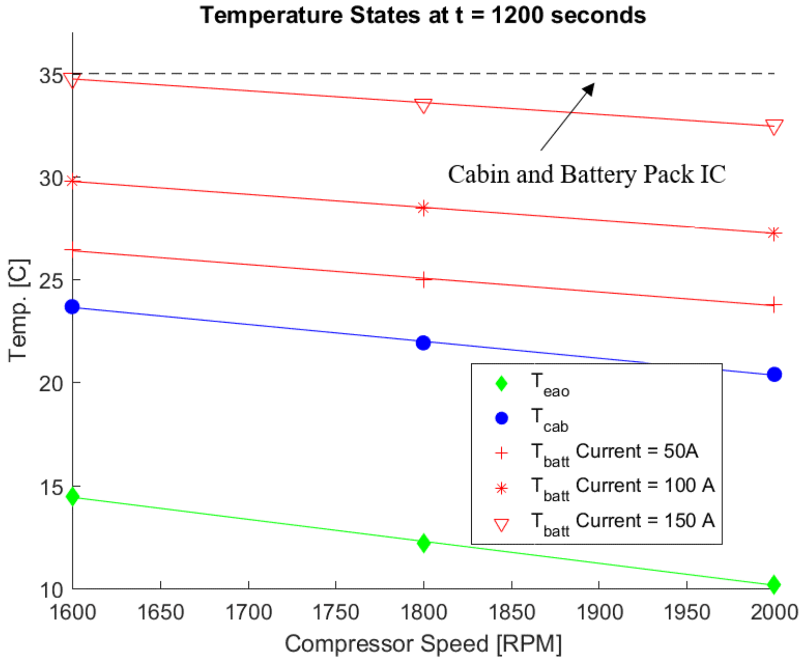

Figure 3.11 Temperature states of the evaporator outlet air, cabin, and battery pack with ‘Simulation 2’ inputs of Table 3.5

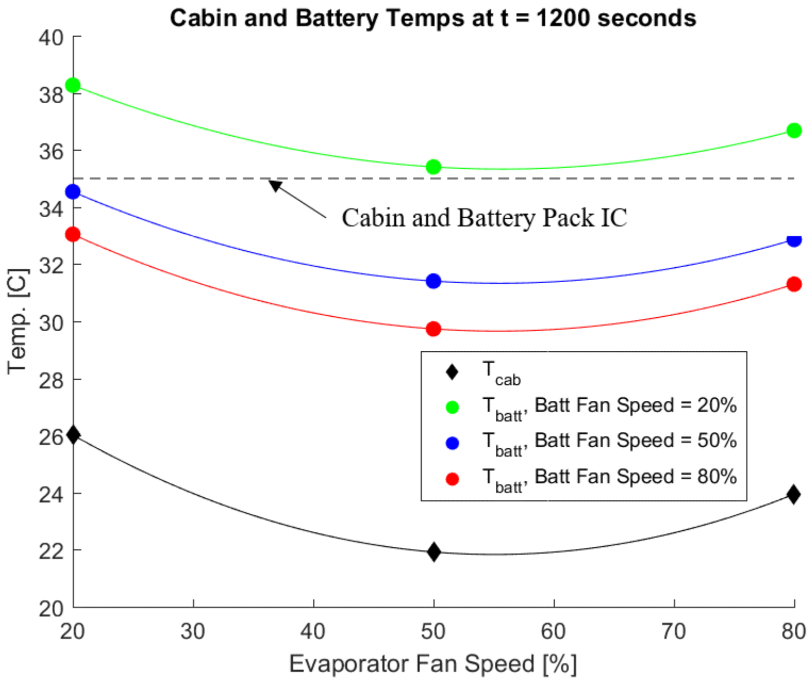

Figure 3.12 Temperature states of the cabin and battery pack with 'Simulation 3' inputs of Table 3.5

3.4.2 Air-cooled Cabin, Liquid-cooled Battery Pack

The simulated air-cooled cabin, liquid-cooled battery pack configuration is detailed in Figure 3.13. The additional liquid-to-liquid heat exchanger is in parallel with the evaporator, thus requiring an additional valve. The evaporator cools air for the cabin and the liquid-to-liquid heat exchanger cools a mixture of Glycol and water (Glycol-75%, Water 25%) for the battery pack. The secondary loop includes a pump to drive the fluid through the battery pack cooling structure and heat exchanger. The battery pack provides power for vehicle traction, the compressor, evaporator/cabin fan, and the pump.

To accommodate the additional heat exchanger cooling capacity, the compressor speeds of this system are greater than that of the air-cooled system and the valve commands are less. The faster compressor speed is to provide enough refrigerant flow into each heat exchanger when the flow splits. The valves are decreased because the flow is split among two valves. The simulation tests are summarized in Table 3.6. In the figures, T_{llo} refers to the outlet temperature of the liquid-to-liquid heat exchanger that cools the battery pack.

The first simulation shows time data for the temperatures of the battery, the evaporator outlet air and cabin air with respect to the same disturbances previously applied to the all air-cooled system. The dynamic responses are similar to that of the air-cooled system but with different magnitudes. Similarly, the battery pack temperature is not maintained within the optimal operating temperature range with the given current disturbance load and with the constant inputs provided.

The second simulation shows the evaporator outlet air temperature, the outlet liquid temperature of the liquid-to-liquid heat exchanger, the cabin temperature, and the battery pack temperatures as a function of compressor speed and current load. It is verified that compressor speed increases the cooling to both loads and that the current has a significant influence on the battery temperature. The cooling to the battery is not dependent on the cabin temperature and is directly applied from the transcritical VCS. Therefore, the battery temperature can feasibly be less that the cabin temperature.

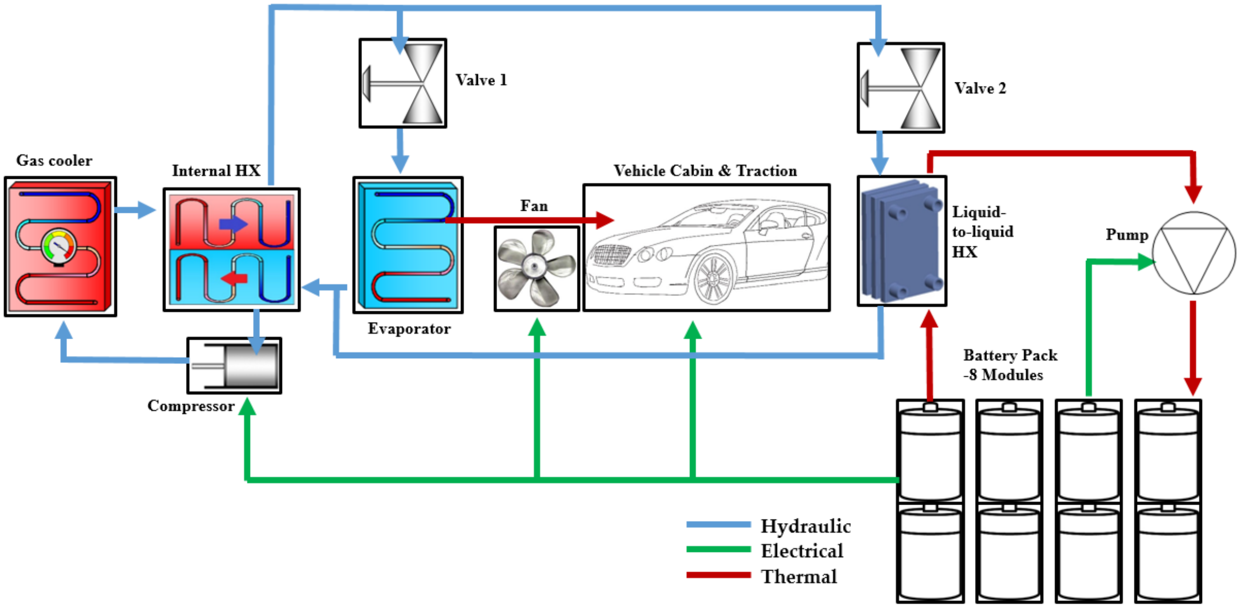

Figure 3.13 Air-cooled cabin, liquid-cooled battery pack system schematic

Table 3.6 Air-cooled cabin, liquid-cooled battery open-loop simulation inputs

	Inputs	Figure
Simulation 1	Fan = 50%, Pump = 10%, Valve 1= 10%,Valve 2= 4% Comp = 2400 RPM Solar Irradiance step change $I_{traction}$ step change	**Fig. 3.14**
Simulation 2	Fan = 50%, Pump = 30%, Valve 1= 10%,Valve 2= 4% $I_{traction}$ = 50, 100, 150 A Comp = 2200, 2400, 2600 RPM	**Fig. 3.15**

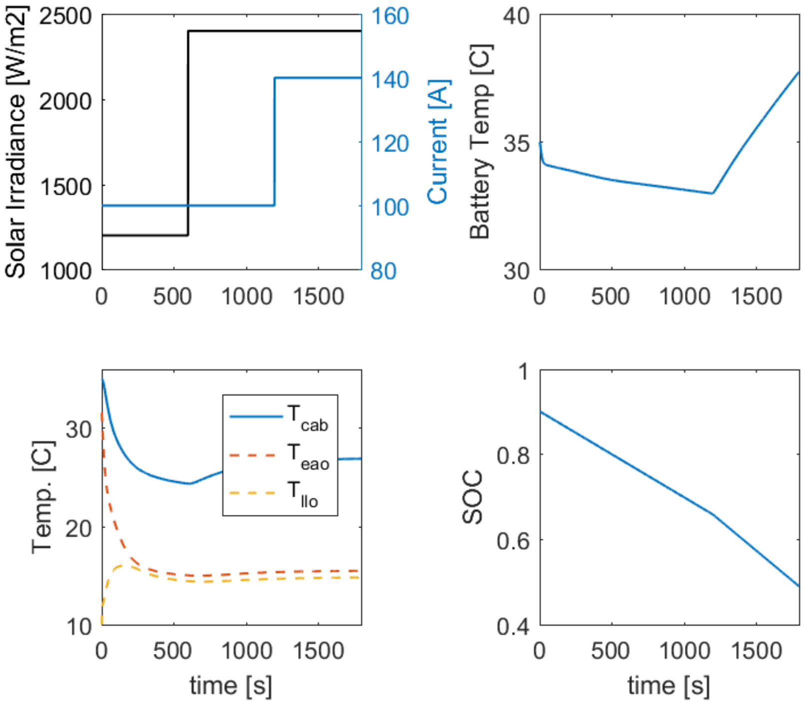

Figure 3.14 Selected outputs with ‘Simulation 1’ inputs of Table 3.6

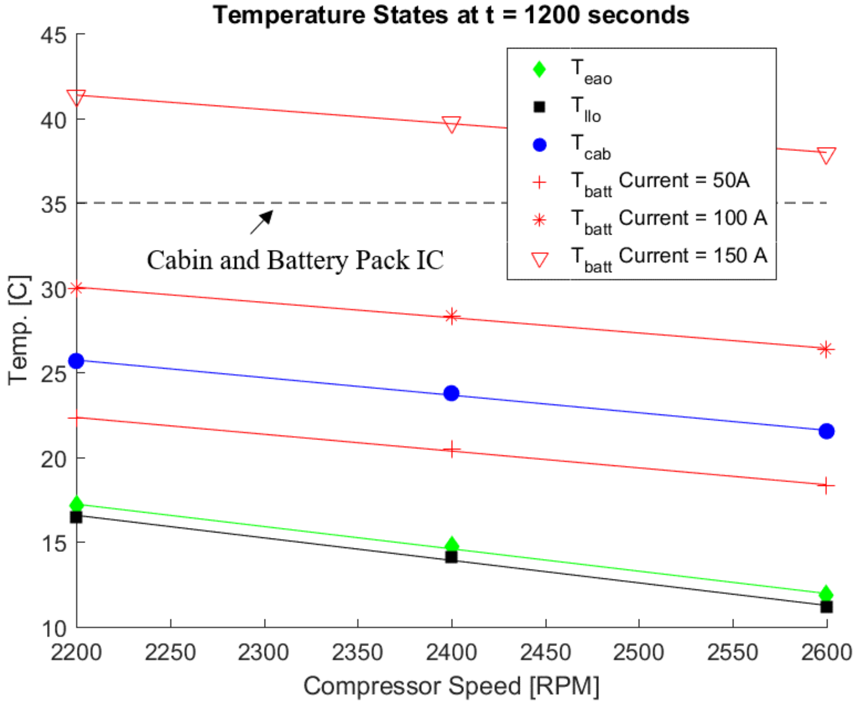

Figure 3.15 Temperature states of the evaporator outlet air, liquid-to-liquid heat exchanger outlet fluid, cabin, and battery pack with 'Simulation 2' inputs of Table 3.6

From these simulations, it is clear that there may exist sets of inputs that result in the same cooling performance of the cabin and battery pack. However, some sets may consume more power and be less efficient. Additionally, nonlinearities and system coupling can make it difficult to extract linear trends of how the system operates. Finally, disturbances such as current discharge rate and solar radiation can prevent the cabin and battery temperature from regulating to a desired temperature. In the next chapter, this thesis will begin to explore closed loop control of the air-cooled cabin, air-cooled battery pack system.

Chapter 4 Baseline Controllers

Chapter 4 develops decentralized baseline controllers for cabin and battery temperature regulation. Decentralized controllers consist of one or multiple SISO control loops; one actuator controls one output. These approaches are often more simple and cheap to implement, and if designed well can give good performance compared to more complex algorithms. In Section 4.1, two baseline controllers for the transcritical VCS are designed for cabin thermal management. Section 4.2 describes the baseline controller for thermal management of the battery pack. Section 4.3 combines the previous two sections and evaluates the performance of the combined system baselines.

4.1 Cabin Temperature Regulation Baseline

The goal is to control the transcritical vapor compression system to provide sufficient cooling to the cabin and consume minimal electrical power. For human comfort, the cabin temperature should be regulated within a desired temperature region. The region of comfort will be taken to be between 20-24 C. The controllable actuators are the compressor speed, evaporator fan speed, and the EEV opening. The airflow rate through the gas cooler is assumed to be a disturbance because in vehicles it is largely a function of velocity. The design of high performance SISO loops is a non-trivial task as many works in the literature have shown that there is coupling between outputs which may result in competing controllers. This is especially evident between the compressor and valve as both influence the mass flow rate of refrigerant through the system. Furthermore, as explained in Chapter 1, it is important to manage the high side pressure in transcritical systems because it strongly affects COP. As mentioned, several works have developed correlations for optimal high side pressure. However, these correlations are dependent on the specific system geometry, operating conditions, and system nonlinearities. These correlations require immense data collection from a physical system or a model. In the two control strategies to be described, correlation free approaches for high side pressure control are considered.

The first baseline uses two PI control loops to control the compressor and evaporator fan. Both PI loops are aiming to track a cabin reference temperature. Recall the formula for the cooling provided to the cabin.

$$Q_{cool} = \dot{m}_{a,evap} c_{p,a} (T_{a,evap,out} - T_{a,cab}) \tag{4.1}$$

The compressor affects the evaporator air outlet temperature and thereby the temperature difference between the supply air and the cabin air. Additionally, the evaporator air mass flow rate affects the cooling multiplicatively with respect to the temperature differential. A ‘weak’ PI controller on the EEV opening is used to maintain the high side pressure within a region of operation. The lower limit is to maintain the transcritical cycle operating above the critical pressure and within a region of acceptable COP range; the upper limit is to ensure safe operation of the compressor. Compressors are limited to discharge temperatures of 150 C. The reference provided to the PI controller is a pressure between the lower and upper limit. The controller gains are ‘weak’ because the goal is not to tightly regulate to the reference, but to apply corrective control if the pressure deviates close to the bounds. Furthermore, when the gains are more aggressive the system sometimes exhibits competing behavior with the actions of the compressor. This control scheme uses three actuators to control two outputs. The next scheme proposes that a better method will use three actuators to control three outputs, thus providing more control of the entire system performance.

The second baseline separates the controlled outputs of the compressor and evaporator fan. The compressor PI controls the cabin temperature and the evaporator fan PI controls the evaporator refrigerant superheat. References [42], [43] demonstrated that the evaporator fan has a significant impact on the evaporator superheat thus supporting this choice of actuator-output pairing. A PI on the valve regulates the high side pressure based on a reference determined by an on-line optimizer proposed by [44]. The on-line optimizer will be summarized in the next section. This baseline control scheme controls three degrees of freedom in the transcritical VCS, namely the low-side pressure, high side pressure, and the shift of the line 1-2 (Figure 4.1). The low-side pressure largely impacts the cooling capacity of the system as it determines the saturation temperature of the refrigerant. The high side pressure is largely coupled with COP in the transcritical system. The last degree of freedom impacts both cooling and COP. More efficient cooling occurs in the two-phase zone due to higher heat transfer coefficients. Additionally, the isentropic lines become more flat further from the two-phase dome, thus impacting the required compressor power. In the proposed controller design, the compressor control is determining the pressure differential between the gas cooler and the evaporator, as it responds to the cabin temperature. The valve control is determining the high side pressure and the evaporator fan is determining the distance from the saturated vapor line via control of evaporator superheat. The two baseline controllers are summarized in Table 4.1 and depicted in Figures 4.2 and 4.3.

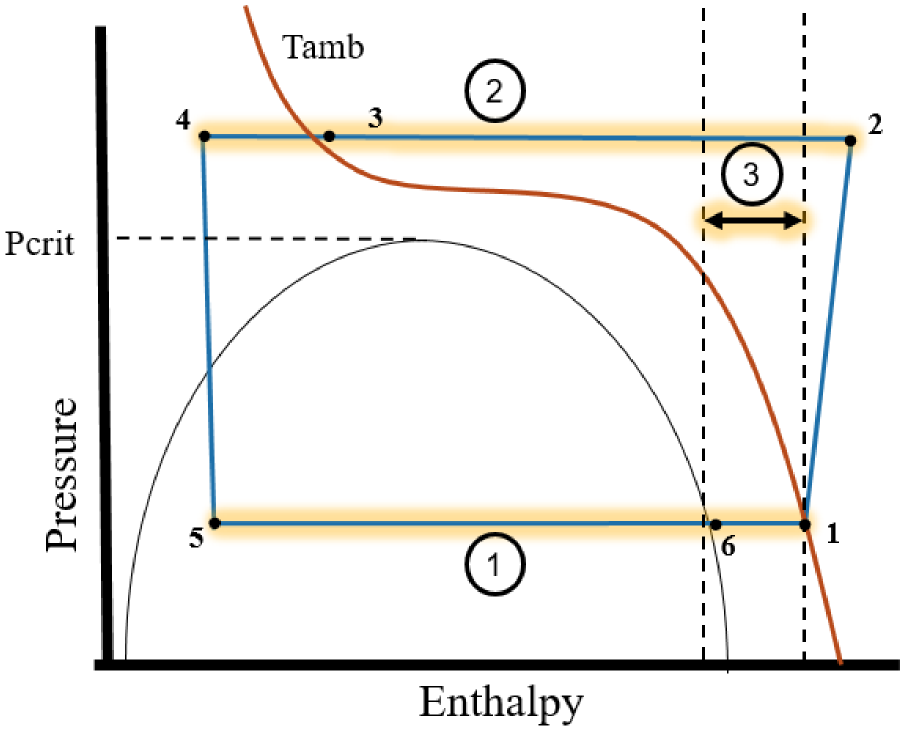

Figure 4.1 Transcritical VCS degrees of freedom

Table 4.1 Comparison of baseline controllers

	Baseline 1		**Baseline 2**		
Actuator	*Controller Type*	*Controlled Output*	*Controller Type*	*Controlled Output*	*Corresponding VCS State*
Compressor	PI	$T_{a,cab}$	PI	$T_{a,cab}$	ΔP_{e-gc}
Evaporator Fan	PI	$T_{a,cab}$	PI	T_{evap}^{sh}	T_{evap}^{sh}
EEV	PI	P_{gc}	On-line optimizer with PI	P_{gc}, COP	P_{gc}

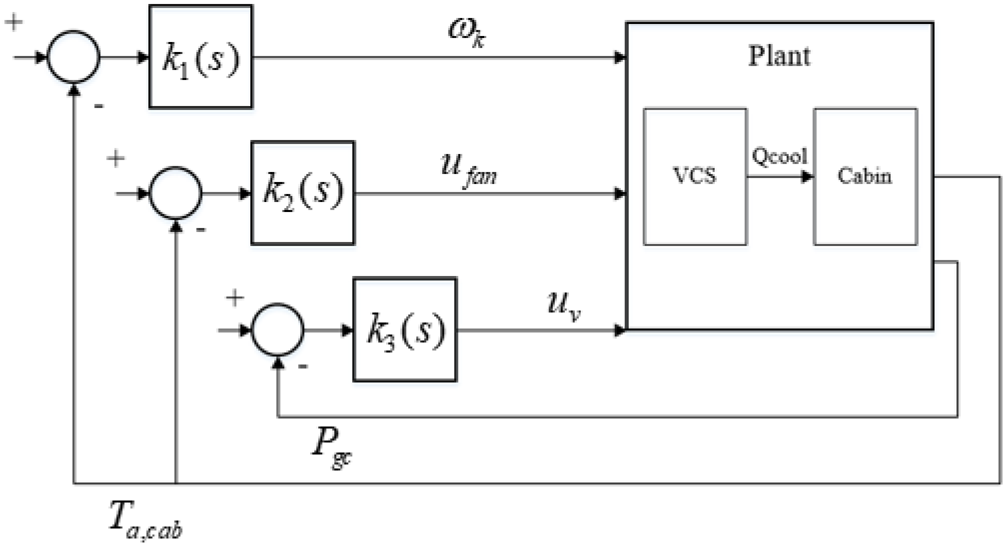

Figure 4.2 Baseline 1 for transcritical vapor compression system control for cabin thermal management

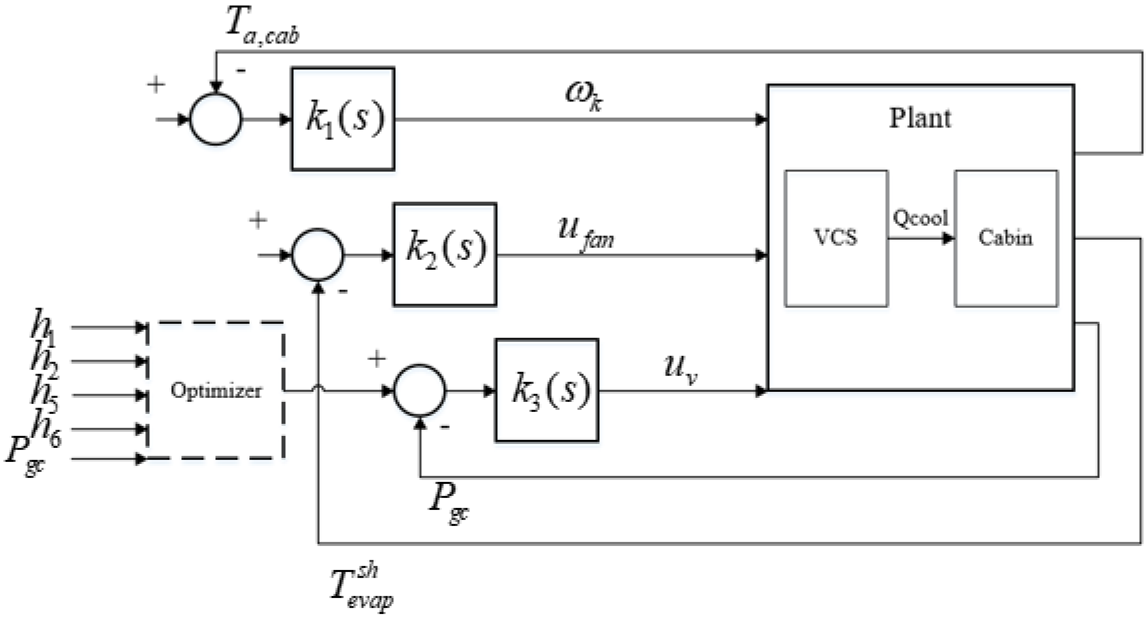

Figure 4.3 Baseline 2 for transcritical vapor compression system control for cabin thermal management

4.1.1 On-line High-side Pressure Optimizer

[44] developed a method for discrete, on-line optimization of the high-side pressure using a correction formula based on the steepest descent method. This method can be used to determine the reference pressure for a PI controller to command the valve. A brief summary of the method is provided here. The correction formula for the optimal high side pressure is a function of the current measured high side pressure state and the gradient of the COP with respect to pressure. The correction formula is

$$P_{gc,k+1} = P_{gc,k} + \alpha \frac{dCOP}{dP_{gc}} \tag{4.2}$$

where k is the discrete time step and α is a gain. If the gradient of the COP with respect to pressure is positive, then the optimal pressure set-point will be increased proportional to the derivative. Likewise, if the gradient is negative then the optimal pressure set-point will be decreased. The derivative of COP can be estimated with real time measurements of temperature and pressure states to determine the state enthalpies.

$$COP = \frac{q}{w} \tag{4.3}$$

$$w = h_2 - h_1 \tag{4.4}$$

$$q = h_6 - h_5 \tag{4.5}$$

where q and w are the specific cooling capacity and specific compressor work respectively. Next, the derivative of COP is taken with respect to P_{gc} using the quotient rule and the result is rearranged.

$$\frac{dCOP}{dP_{gc}} = \frac{d\left(\frac{q}{w}\right)}{dP_{gc}} = \frac{w\frac{dq}{dP_{gc}} - q\frac{dw}{dP_{gc}}}{w^2} = \frac{1}{w}\frac{dq}{dP_{gc}} - \frac{q}{w^2}\frac{dw}{dP_{gc}} = COP\left(\frac{1}{q}\frac{dq}{dP_{gc}} - \frac{1}{w}\frac{dw}{dP_{gc}}\right) \tag{4.6}$$

The derivatives can be approximated by the finite difference method.

$$\frac{dCOP}{dP_{gc}} = COP\left(\frac{\Delta q}{q} - \frac{\Delta w}{w}\right)\frac{1}{\Delta P_{gc}} \tag{4.7}$$

Now define θ and substitute back into Equation 4.7.

$$\theta(P_{gc}) = \frac{\Delta q}{q} - \frac{\Delta w}{w} \tag{4.8}$$

$$\frac{dCOP}{dP_{gc}} = COP\frac{\theta}{\Delta P_{gc}} \tag{4.9}$$

At each time step, COP is a scaling factor in Equation 4.9. θ alone has approximately the same meaning as the full derivative of COP but without the problem of division by zero in the case that $\Delta P_{gc} \to 0$. Therefore, the expression for θ is substituted into the correction formula of Equation 4.2.

$$P_{gc,k+1} = P_{gc,k} \pm \alpha\theta_k \tag{4.10}$$

The sign in the correction formula is dictated by the combination of the sign of the change in pressure ΔP_{gc} from the previous sample time, and the sign of θ_k.

$$\Delta P_{gc} = P_{gc,k} - P_{gc,k-1} \tag{4.11}$$

$$P_{gc,k+1} = \begin{cases} P_{gc,k} + \alpha\theta_k, \; if \; \text{sgn}(\Delta P_{gc}) * \text{sgn}(\alpha_k) = 1 \\ P_{gc,k} - \alpha\theta_k, \; if \; \text{sgn}(\Delta P_{gc}) * \text{sgn}(\alpha_k) = -1 \end{cases} \tag{4.12}$$

4.1.2 Impact of Superheat on COP

For subcritical systems, it is common to maintain evaporator superheat within 5-15 C via passive or active control of the valve (i.e. thermostatic expansion valve, electronic expansion valve, etc.). The purpose of this control is to maintain high system efficiency by reducing the compressor power and maintaining most of the cooling within the two-phase zone (improved heat transfer coefficients). As previously mentioned, the COP of transcritical vapor compression systems is largely determined by the high side pressure. Therefore, the same superheat criterion may not apply to the transcritical CO_2 system.

To determine a suitable region of superheat for the transcritical VCS system, simulation data was collected for a range of actuator inputs surrounding the nominal inputs. The nominal actuator inputs considered in this thesis are $u_v = 8[\%];\ u_{fan} = 50[\%];\ \omega_k = 1800[rpm]$. Each actuator was varied below and above its nominal value, while the other actuators were held constant. The steady state evaporator superheat, high side pressure, and COP were collected, and the results are shown in Figures 4.4-4.6. Figures 4.4 and 4.5 are 3D plots from different angles of COP with respect to gas cooler pressure and evaporator superheat. Figure 4.6 projects the COP data onto the gas cooler pressure and evaporator superheat plane.

Evaporator superheat and gas cooler pressure increase as a result of increasing compressor speed. Furthermore, the COP is seen to decrease with increasing superheat. The range of attainable COP spans values less than 1 and greater than 1.6. The compressor consumes the most power of the three VCS actuators. Therefore, increasing the compressor speed has a large impact on power consumption. The increased superheat further increases the power required by the compressor due to increased specific volume of the refrigerant.

The superheat and gas cooler pressure increase with increasing fan speed. In this case, increasing superheat has a positive impact on the COP because more cooling is provided and outweighs the increase in compressor power due to superheat. Furthermore, the fan has a relatively small impact on the high side pressure, and so the COP is not also affected by a high side pressure change.

Finally, the superheat is shown to decrease as the valve opens, while the steady-state high side pressure is shown to increase initially, and then decrease. The superheat decreases because the refrigerant flow rate increases. However, the increase in high side pressure may be counterintuitive. As mentioned at the beginning of Chapter 2, the models have not been validated, so it is uncertain if this is an actualizable physical behavior. However, this behavior will be analyzed further in Section 4.1.3. Figures 4.4-4.6 shows that within the operating region considered, the COP is improved with superheat less than about 40 C that results from a more open valve.

It is clear from this evaluation that there exists numerous variables impacting system COP, and that superheat does have some impact. However, the superheat does not require maintenance within the same region as a subcritical system. For the parameters and operating conditions of this thesis, the COP is of a reasonable value between 10 and 40 C, given the high side pressure is maintained within an optimal operating range and compressor outlet temperature is below 150 C. This superheat operating range may not be applicable for all transcritical systems, but rather an appropriate range for this work. A more thorough data collection and analysis would be beneficial for other systems with different parameters and operating conditions.

Additionally, these results support the use of the evaporator fan to control superheat in Baseline 2. The fan has less impact on the system pressure, as compared to the compressor and valve, thereby limiting interference with the high side pressure controller. Furthermore, the fan has a clear impact on evaporator superheat.

4.1.3 Impact of Valve Opening on High Side Pressure

It is observed that the high side pressure response to the valve opening is non-monotonic and potentially coupled with system refrigerant flow rate. At lower refrigerant mass flow rates, it is observed that the high side pressure increases with valve opening. At larger refrigerant flow rates, the high side pressure decreases with an increase in valve opening. Figures 4.7 and 4.8 provide the COP variance with respect to gas cooler pressure and superheat with respect to two compressor speeds and varied valve opening. At a compressor speed of 1800 RPM, the high side pressure increases with valve opening from 6% to 9%. At greater flowrates beginning at 10%, the high side pressure decreases with valve opening. At a compressor speed of 2400 RPM, the high side pressure increases (slightly) with valve opening from 9 to 10%. Beyond 10%, increasing the valve opening reduces the high side pressure. Furthermore, for the same valve opening of 9, 10 and 11%, the high side pressure is lower with a slower compressor speed. The high side pressure appears to be dominated by the compressor speed at lower system flow rates and dominated by the valve at higher system flow rates. This will be an important result for the closed-loop system.

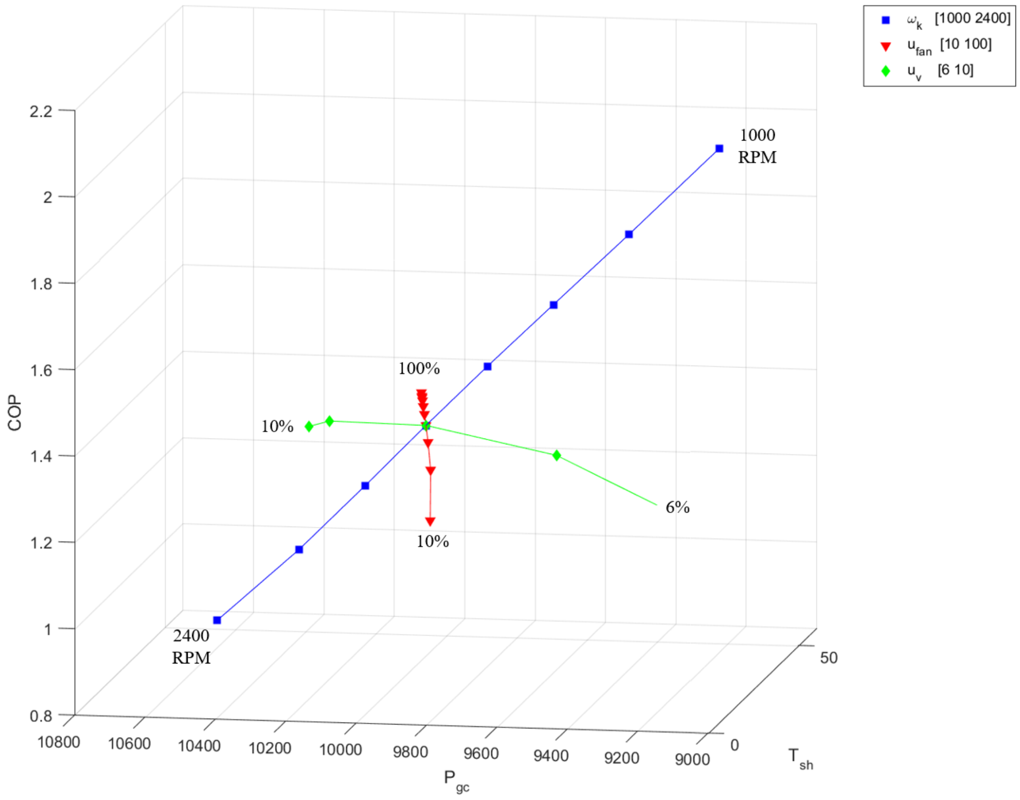

Figure 4.4 3D plot of COP with respect to superheat and gas cooler pressure for variation of compressor speed, evaporator fan speed, and valve opening; Angle 1

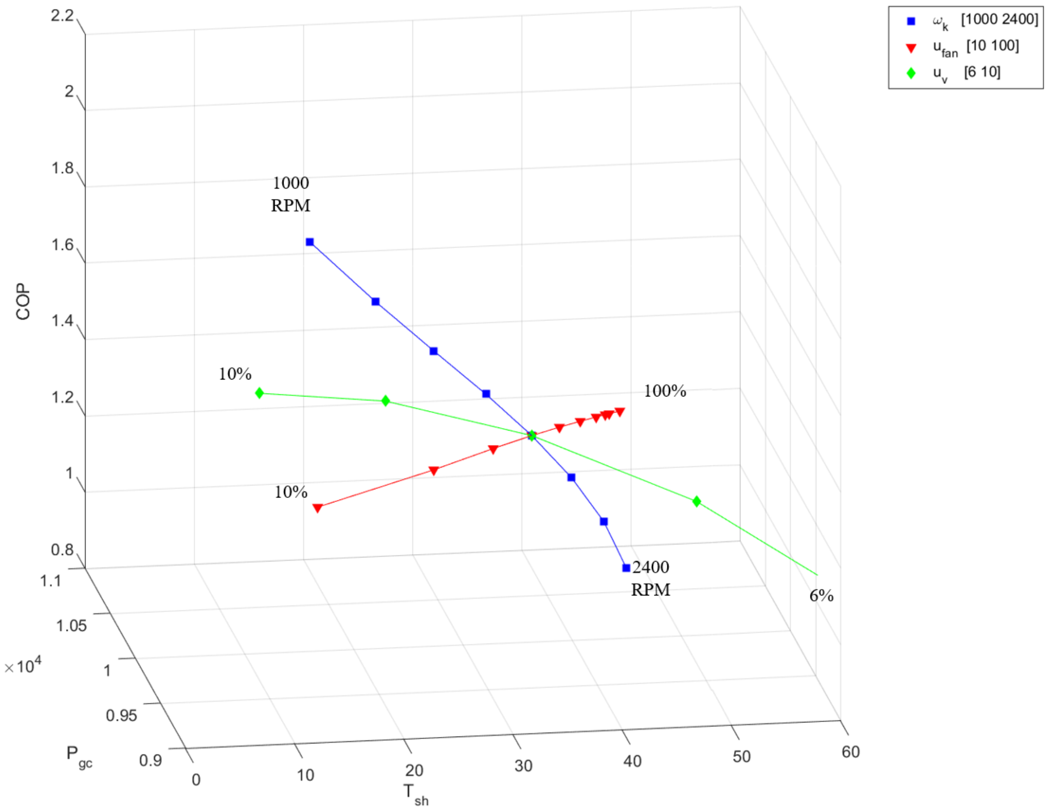

Figure 4.5 3D plot of COP with respect to superheat and gas cooler pressure for variation of compressor speed, evaporator fan speed, and valve opening; Angle 2

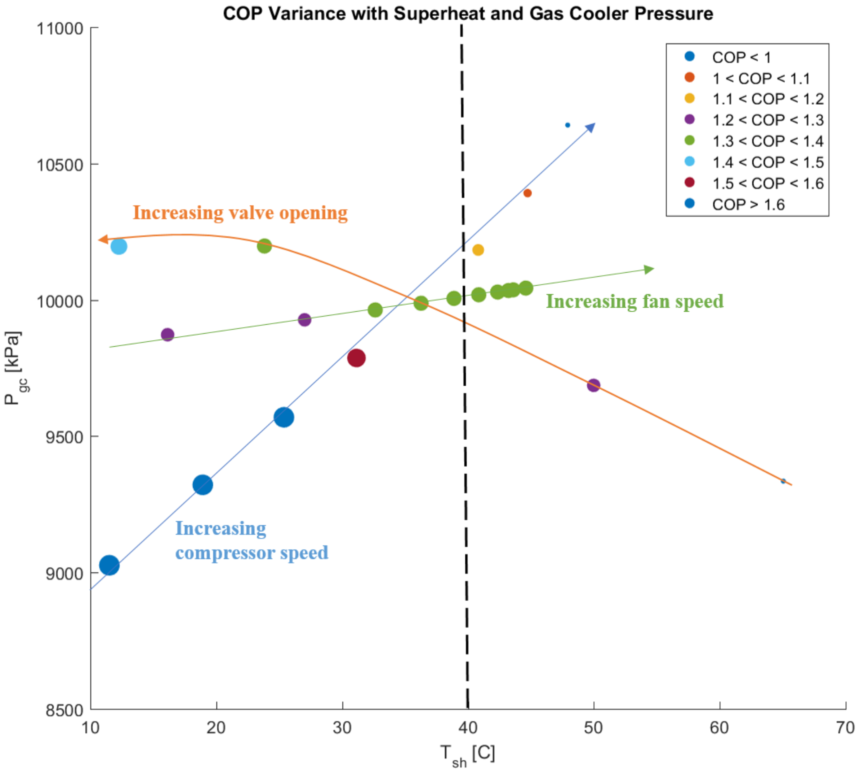

Figure 4.6 COP with respect to superheat and gas cooler pressure for variation of compressor speed, evaporator fan speed, and valve opening. Circle size corresponds to magnitude of COP

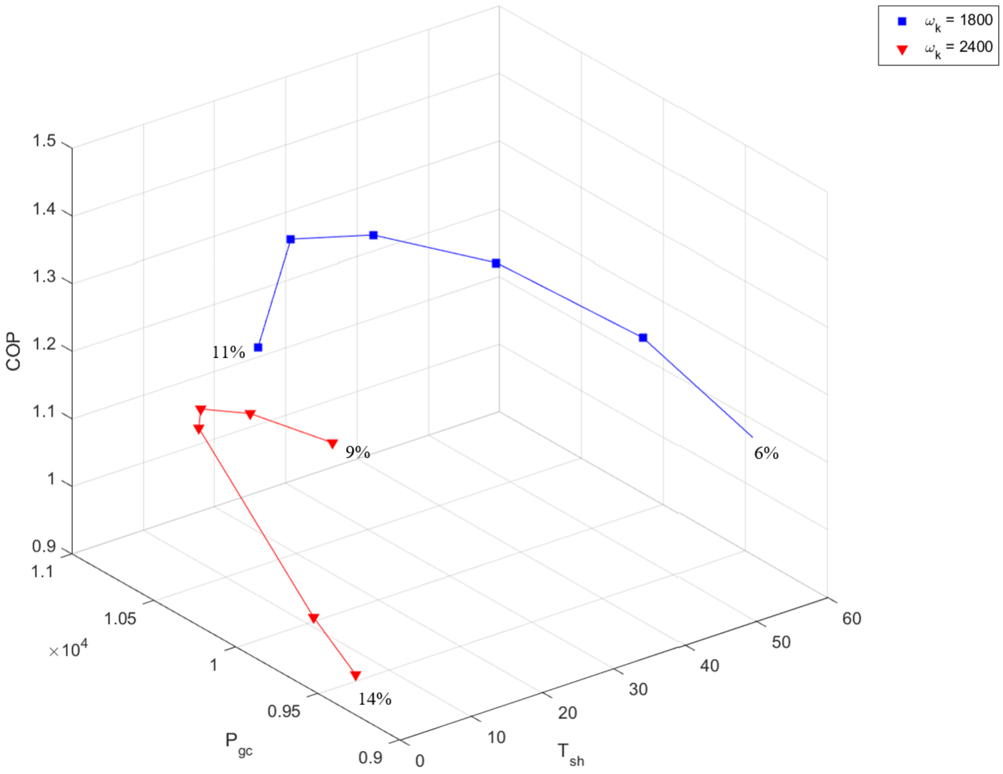

Figure 4.7 3D plot of COP with respect to superheat and gas cooler pressure when valve opening is varied for two compressor speeds

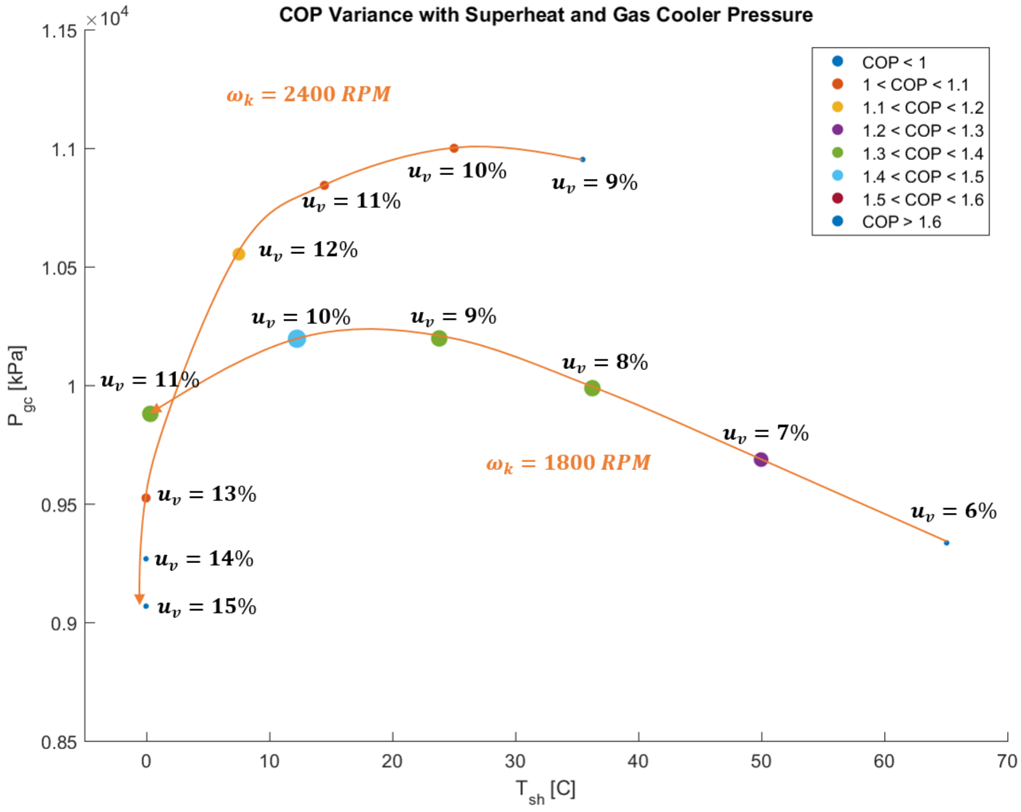

Figure 4.8 COP with respect to superheat and gas cooler pressure when valve opening is varied for two compressor speeds. Circle size corresponds to magnitude of COP

4.1.4 Evaluation of Baseline Controllers

This section evaluates the performance of both baseline controllers in simulation. The controller gains, provided in Table 4.2, were hand-tuned to balance tracking performance, avoidance of aggressive actuator behavior, and to avoid loss of superheat. Note that $k_3(s)$ of Baseline 2 is I-gain dominant. This means that many of the control input responses will have ramp-like behavior that is linear with respect to time, as seen in the valve and fan commands of Figures 4.9 and 4.13. The parameters for the optimizer are given in Equation 4.13. T_s is the discrete sample time and $\Delta P_{\max}$ is the magnitude of the maximum change in set-point at each step.

$$T_s = 300\,s, \alpha = 3000,\ \Delta P_{\max} = 1000\,kPa \tag{4.13}$$

The previous section showed that opening the valve (around the nominal value of 8%) in open-loop, and with compressor speed and evaporator fan speed held constant, increased high side pressure. However, in closed-loop the high side pressure response is relative to both the compressor and valve. Consequently, the high side pressure decreases in closed-loop when the valve opens. Opening the valve increases the refrigerant flow to the evaporator and provides more cooling, which in turn causes the compressor to slow down. As previously discussed, the compressor dominates the high side pressure response in this operating range (lower refrigerant mass flow rates) and thus the high side pressure decreases. Therefore, the controller is designed to increase the valve opening when the setpoint is lower than the measured pressure, and decrease the valve opening when the setpoint is higher than the measured pressure. This controller formulation applies for both low refrigerant flow rates and high refrigerant flowrates.

Table 4.2 Tuned gains for PI controllers

Controller	**Baseline 1**		**Baseline 2**	
	P	I	P	I
$k_1(s)$	150	0.5	100	0.2
$k_2(s)$	5	0.01	0.5	1.00E-03
$k_3(s)$	1.00E-03	0	1.00E-05	1.00E-06

The commands and outputs of the baseline controllers when constant disturbances are applied to the plant is shown in Figures 4.9 and 4.10. Constant disturbances means that the loads on the cabin are constant, i.e. solar radiation, wind speed, etc., and the inlet conditions to the gas cooler of the VCS are constant. The initial conditions are provided in Equation 4.14.

$$T_{a,cab,i} = 30[C];\ u_{v,i} = 8[\%];\ u_{fan,i} = 50[\%];\ \omega_{k,i} = 1800[rpm] \tag{4.14}$$

Each controller is tracking a cabin temperature of 23 C. Baseline 1 is tracking a high side pressure of 9,500 kPa. Baseline 2 is tracking 15 C superheat in the evaporator and the optimizer updates the high side pressure reference every 300 seconds. Baseline 1 achieves steady state operation at approximately 1600 seconds when it achieves 23 C in the cabin. Because of the continuously adjusting high side pressure reference, Baseline 2 takes more time to reach steady state operation. The valve adjusts based on the updated reference, which has a cascading effect causing the compressor and fan to adjust to track the cabin temperature and superheat. Due to the continuous reference adjustments and the inescapable coupling of the system variables, Baseline 2 has greater reference tracking error of the cabin temperature, including steady state error. However, it does maintain the temperature within ± 1.5 degree of the reference which is within the comfort range. The combined power consumption of the evaporator fan and compressor is given in Figure 4.8. Baseline 1 consumes 17.2% more energy than Baseline 2.

Next, a disturbance to the plant is varied to qualify the controller robustness to uncertainty. The gas cooler air mass flow rate disturbance is shown in Figure 4.12. The results of the simulation of both controllers is provided in Figures 4.13-4.15. Both controllers exhibit increased variability in tracking error of the cabin temperature, but are able to maintain the temperature within a comfortable range. Additionally, both baseline controllers remain stable and respond accordingly to the applied disturbance. As a result of the control structure, Baseline 1 exhibits highly transient valve behavior as it responds to the transient gas cooler pressure. Baseline 2 exhibits transient fan behavior as it responds to the transient superheat in the evaporator. Baseline 1 consumes 17.7% more energy than Baseline 2.

A summary of the baseline controller performances with respect to root mean square error (RMSE) (Equation 4.15) of cabin temperature error and the integral of power consumption is given in Table 4.3. The RMSE error is taken starting at 500 seconds after the initial pull down of the cabin temperature. Baseline 1 gives smaller RMSE of the cabin temperature, but at the cost of greater power consumption compared to Baseline 2.

$$RMSE_{cab} = \sqrt{\frac{\sum_{k=1}^{k=n}\left(T_{cab,k} - T_{cab}^{sp}\right)^2}{n}} \tag{4.15}$$

Table 4.3 Transcritical VCS and cabin baseline performance

Applied Load	**Baseline 1**		**Baseline 2**	
	$RMSE_{cab}$	$\int P$	$RMSE_{cab}$	$\int P$
Constant disturbances	0.4868	2.084E6	0.8816	1.778E6
Varied $\dot{m}_{a,in,gc}$	0.4751	2.099E6	0.8795	1.783E6

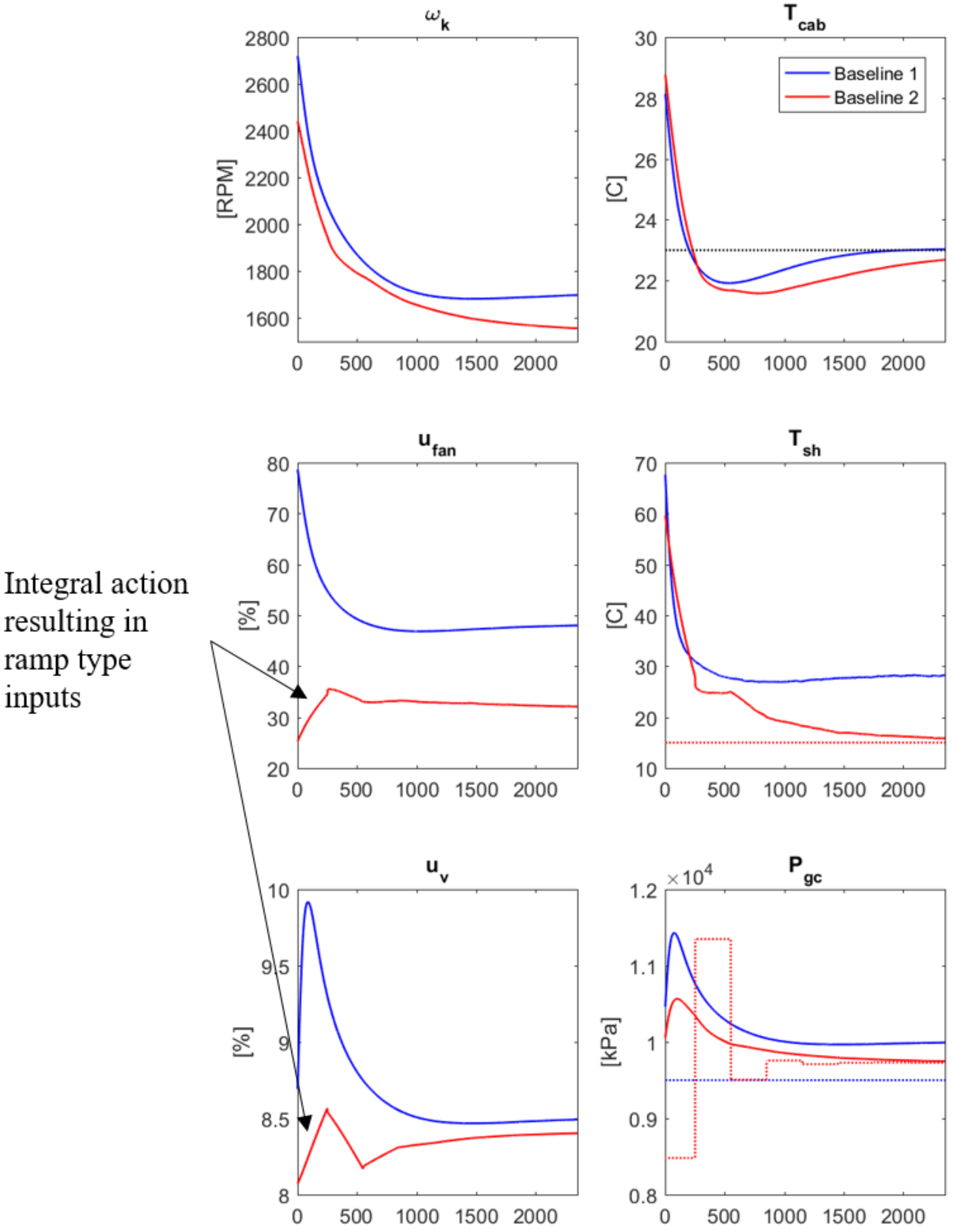

Integral action resulting in ramp type inputs

Figure 4.9 Baseline controllers' performance with constant loads and disturbances. Note: Dotted lines are references (black is a mutual reference for Baseline 1 and Baseline 2, otherwise color corresponding with controller)

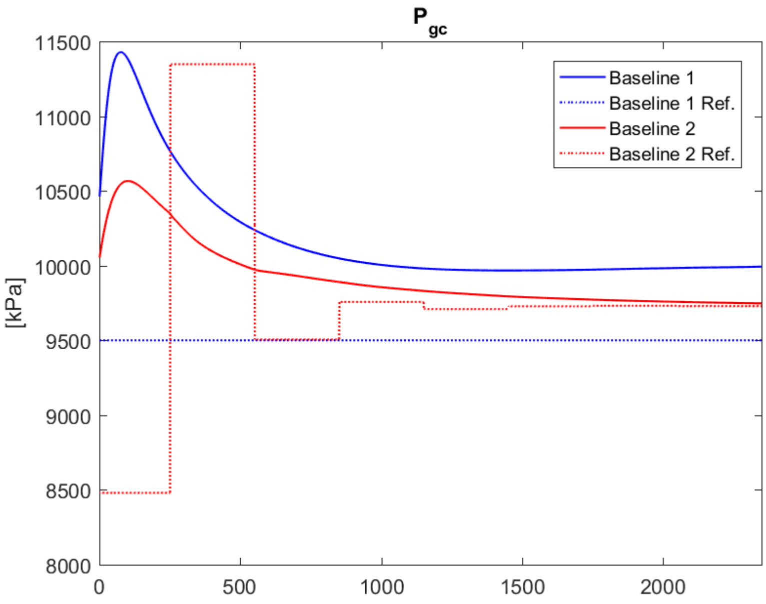

Figure 4.10 Gas cooler reference pressure and actual pressure of Baseline 1 and Baseline 2 with constant loads and disturbances

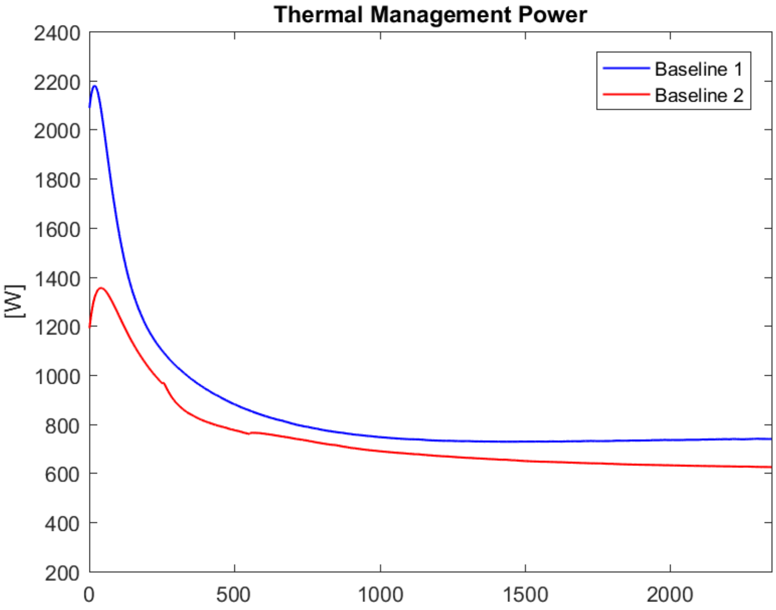

Figure 4.11 Power consumption of baseline controllers with constant loads and disturbances

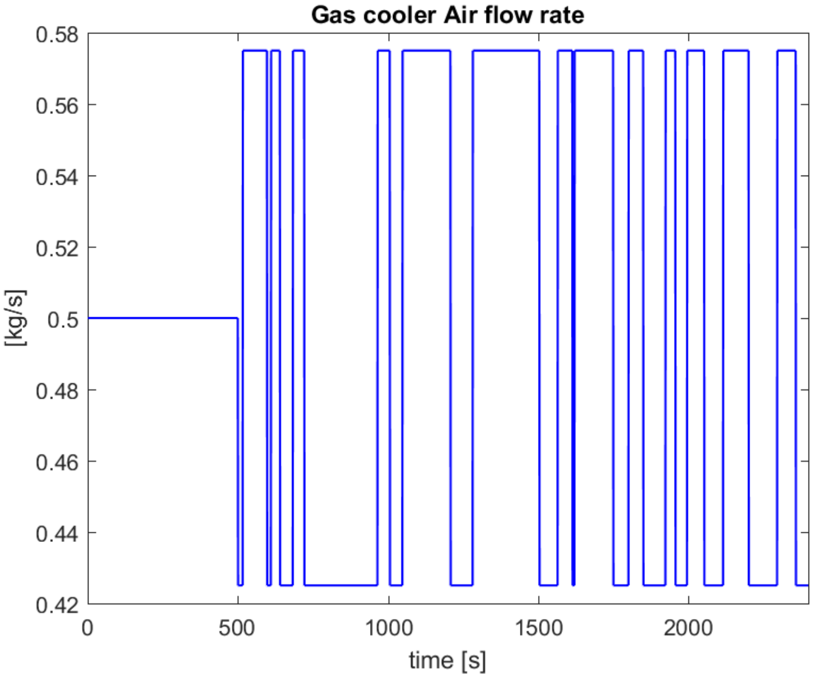

Figure 4.12 Gas cooler air flow rate disturbance applied to plant to test robustness of baseline controllers

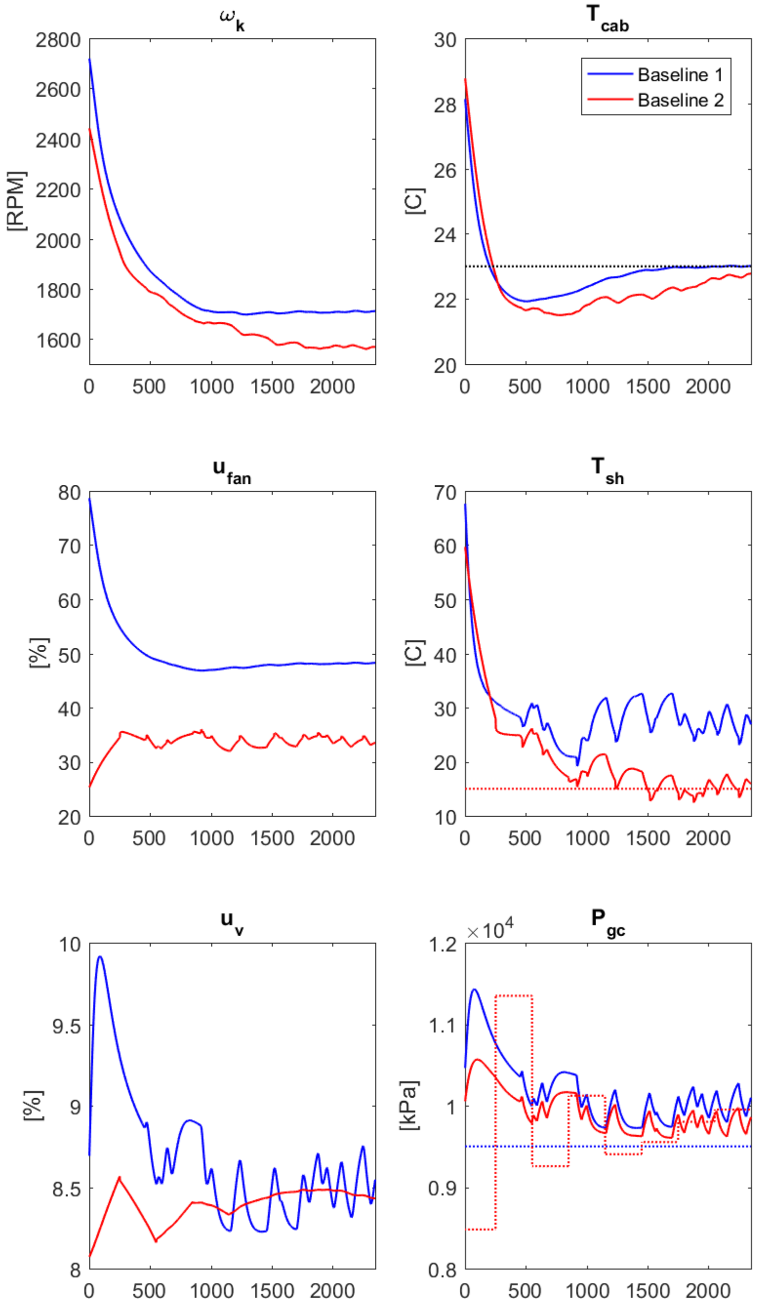

Figure 4.13 Baseline controllers' performance with applied gas cooler air mass flowrate disturbance

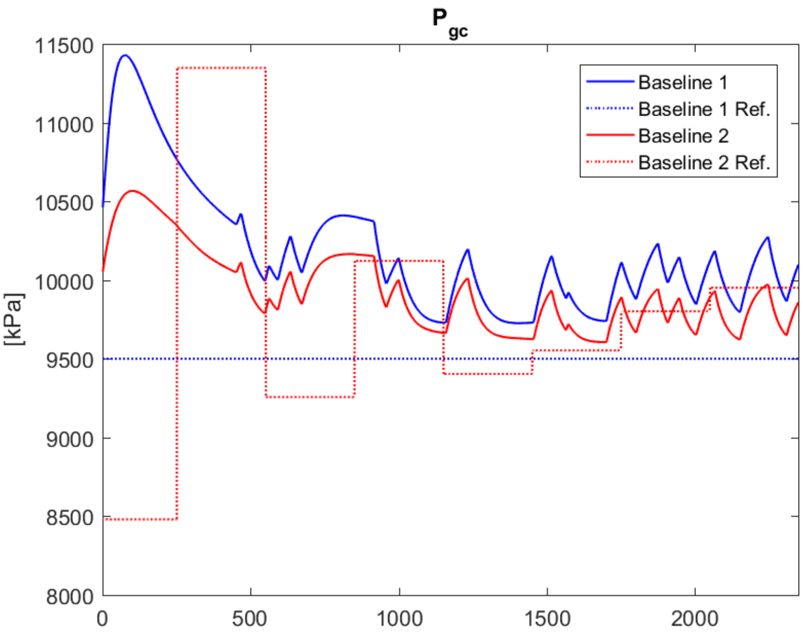

Figure 4.14 Gas cooler reference pressure and actual pressure of Baseline 1 and Baseline 2 with applied gas cooler air mass flowrate disturbance

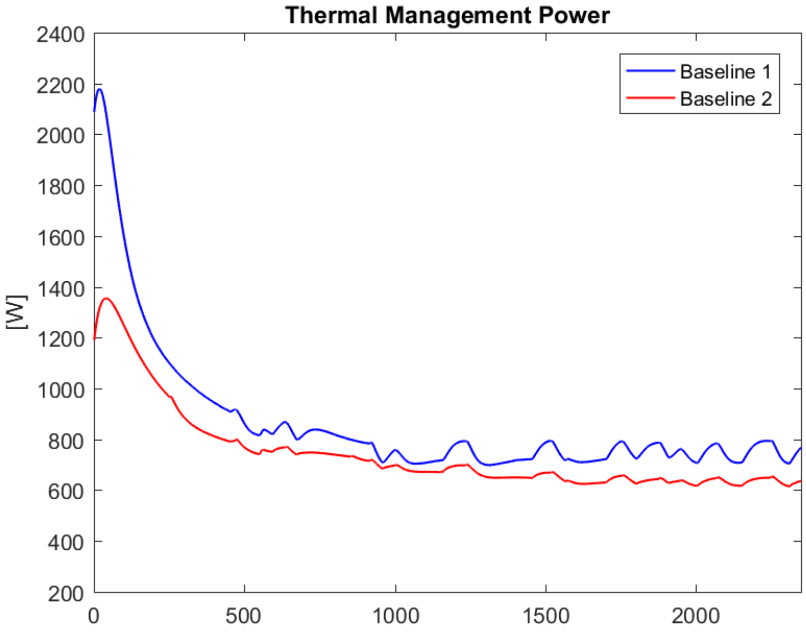

Figure 4.15 Power consumption of baseline controllers with applied gas cooler air mass flowrate disturbance

4.2 Battery Temperature Regulation Baseline

The additional actuator for cooling of the battery pack is the battery fan. In air-cooled battery packs, the fan circulates cooled air through the battery pack. The air can be sourced from the outside environment, the cabin, or an auxiliary evaporator. In the air-cooled cabin, air-cooled battery configuration described in this work, the air cooling for the battery is sourced from the cabin. Therefore the cooling of the battery pack is affected by the performance of the transcritical VCS in cooling the cabin air. The baseline control applied to the battery fan is a PI controller that regulates the mean battery core temperature. The battery core temperature is chosen because it has a slower response to cooling because of its larger thermal capacitance as compared to the surface temperature. It is assumed that for application to a physical system, the surface temperature could be measured and the core temperature estimated based on models. Furthermore, the mean core temperature (average of each module in the battery pack) is chosen as opposed to the maximum core temperature because using the average acts as a filter and prevents aggressive switching behavior of the fan. A block diagram of the battery pack baseline controller is given in Figure 4.16. The gains of the controller are provided in Equation 4.16.

$$P = 50,\ I = 1 \tag{4.16}$$

Figure 4.17 compares the closed loop plant when the controlled temperature is the mean surface temperature compared to the mean core temperature. It can be seen by the blue lines that when the surface temperature is controlled the core temperature remains much hotter and the fan is not actuated as much as it could be to provide cooling. The maximum temperature of the battery pack is regulated when the core temperature is controlled. The response of the controlled plant with respect to a range of air inlet temperatures is shown in Figure 4.18. When the inlet air temperature is less than 24 C, the fan controller is able to achieve perfect tracking of the core temperature. At warmer air inlet temperatures, the fan speed reaches saturation (100%) and there is reference-tracking error. At inlet temperatures of 28 and 30 C, the core temperature approaches or exceeds the upper bound for optimal battery operating conditions. These results indicate the necessity for well-performing thermal regulation of the cabin.

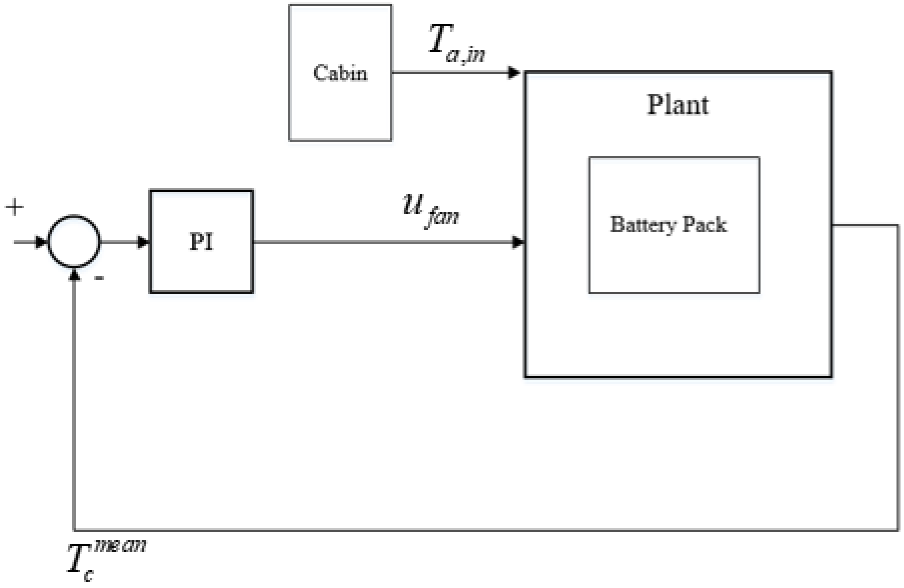

Figure 4.16 Baseline battery pack controller to regulate mean core temperature

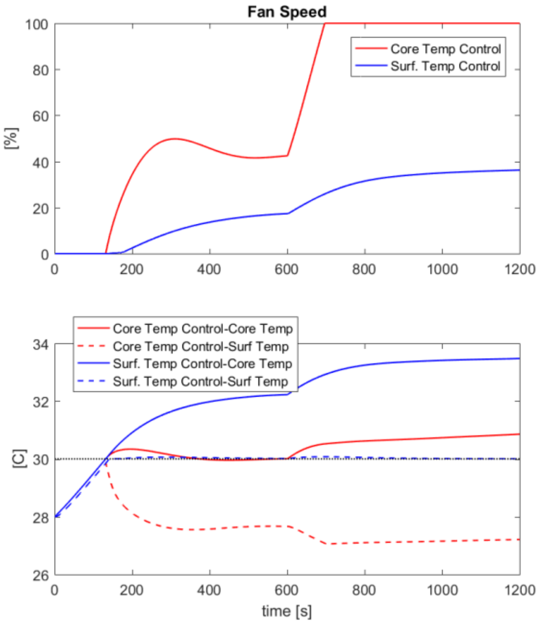

Figure 4.17 Comparison of closed loop control of the mean battery pack surface temperature and core temperature

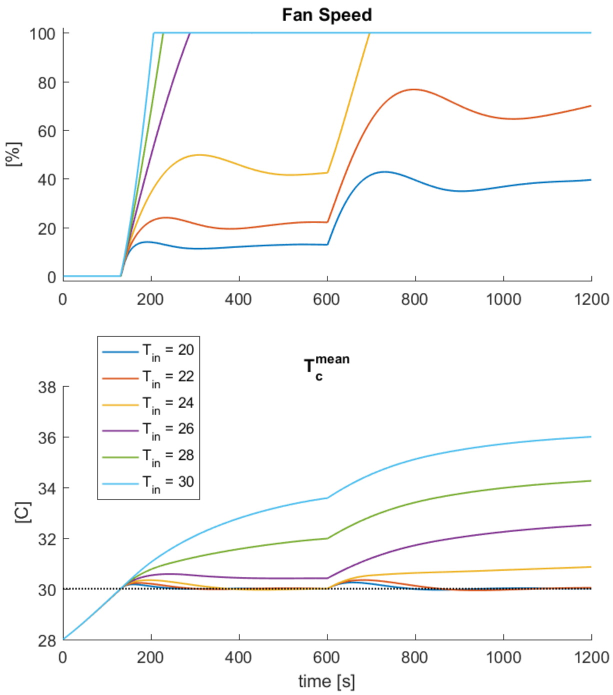

Figure 4.18 Comparison of control effort and mean battery core temperature as a result of variable inlet air temperature

4.3 Combined System Baseline

The final step in the baseline control is to combine the previous controllers for the air-cooled cabin and air-cooled battery pack configuration. Each of the two baselines for cabin thermal management will be paired with the single baseline for the battery pack thermal management. Therefore, there are two combined system baseline controllers, as depicted in Figures 4.19 and 4.20.

A random traction current and gas cooler air mass flow rate load was applied to the closed loop system (Figure 4.21) in simulation to evaluate the performance of each baseline controller. The results of these simulations are described in Figures 4.22-4.25. Baseline 1 is able to bring down the cabin temperature faster and this trickles down to benefit the battery pack. The battery fan puts in less effort initially compared to Baseline 2 because it is receiving cooler air from the cabin at that time. Due to the fluctuating current, it is far more difficult to achieve perfect tracking of the battery pack temperature, but the battery fan does adjust to mitigate the temperature deviation. As expected from Section 4.1, Baseline 2 consumes less power than Baseline 1 with slightly poorer regulation of the cabin temperature. But, both controllers are successful in keeping the cabin temperature within the comfortable range and the battery temperature within its optimal operating range.

A limitation of both decentralized baseline controllers is that they are reactionary control schemes. The control action is a result of measured error. In the event of a persistent disturbance, such as a large current load, it could be expected that the battery temperature may exceed the optimal operating range because the controllers cannot respond quick enough. Furthermore, the controllers are not coordinated. For example, it may be ideal if the transcritical vapor compression system were to provide extra cooling to the cabin when a large current load is applied to help in managing the battery temperature. In Chapter 5, a model-based, centralized control approach will be formulated that will be able to control the system in a unified manner to achieve the performance objectives.

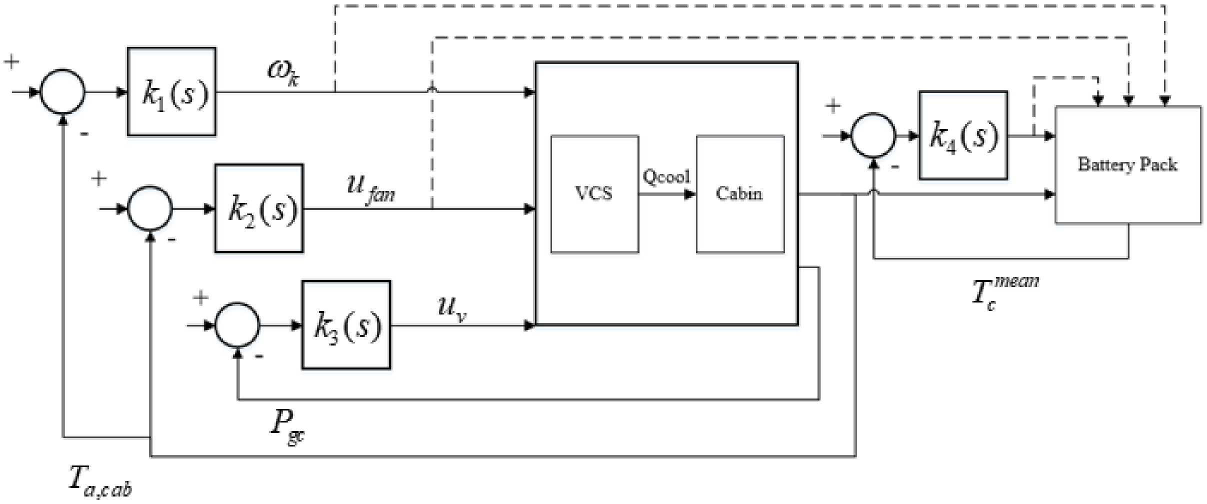

Figure 4.19 Combined Baseline 1 and battery thermal management baseline. The dashed lines represent the power consumption of the actuators.

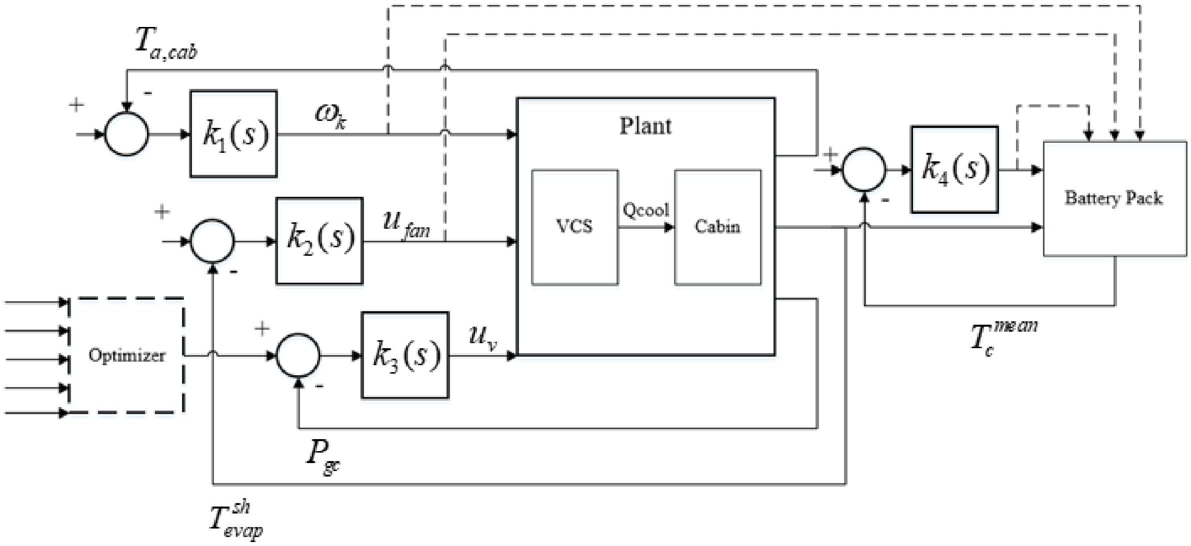

Figure 4.20 Combined Baseline 2 and battery thermal management baseline. The dashed lines represent the power consumption of the actuators.

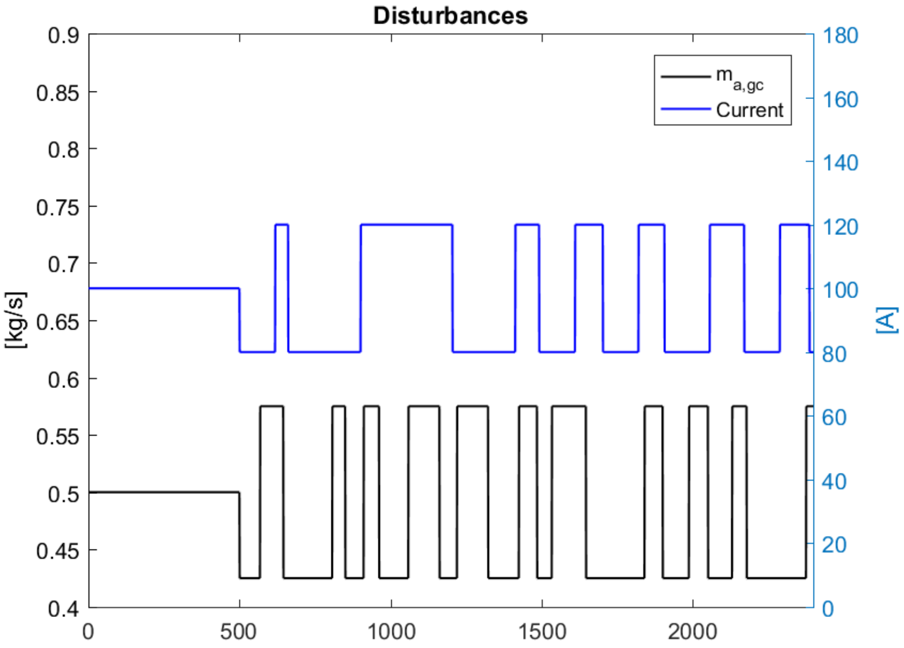

Figure 4.21 Applied traction current and gas cooler air flow rate disturbances to combined Baseline 1 and Baseline 2 controller systems

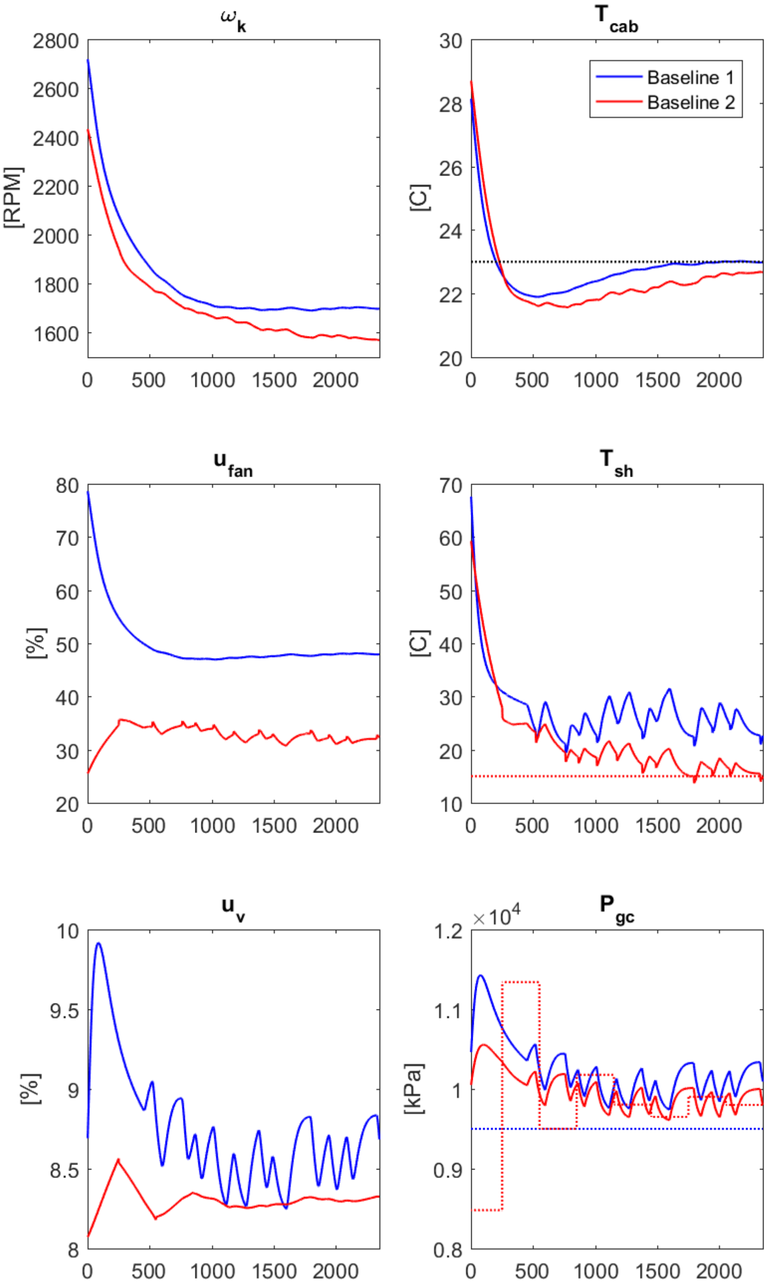

Figure 4.22 Combined Baseline controllers' cabin performance with applied gas cooler air mass flowrate and traction current disturbance

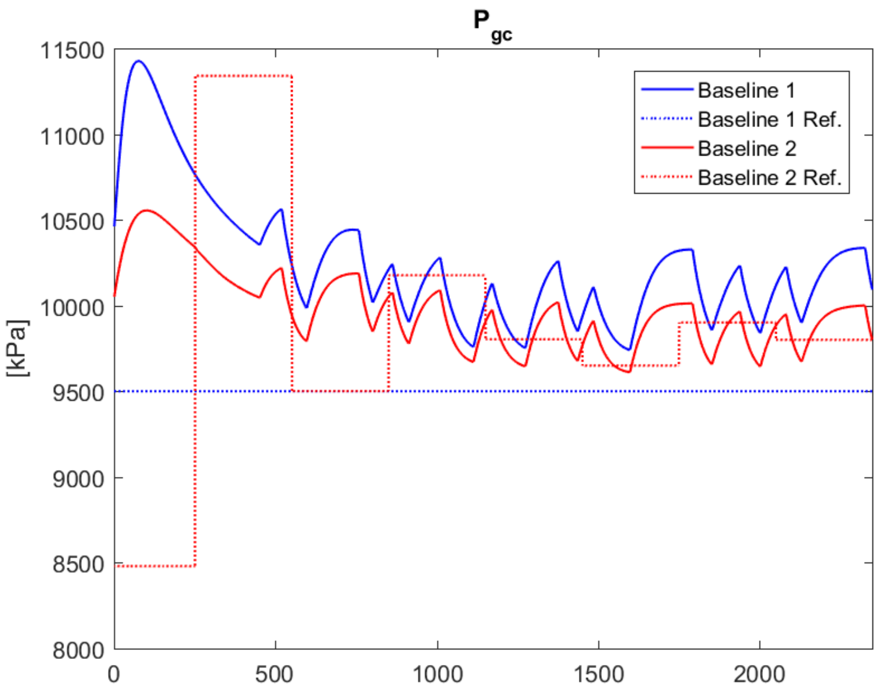

Figure 4.23 Gas cooler reference pressure and actual pressure of Combined Baseline 1 and Baseline 2 with applied gas cooler air mass flowrate and traction current disturbance

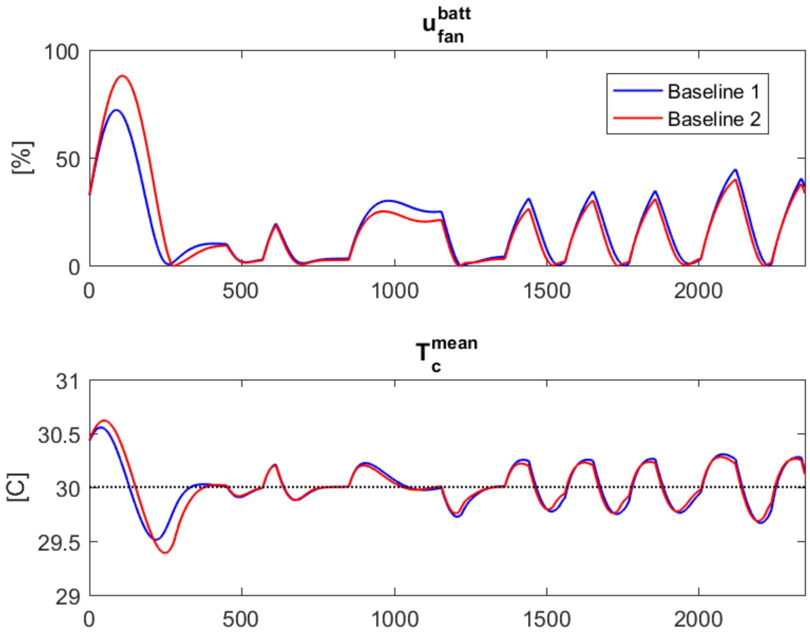

Figure 4.24 Combined Baseline controllers' battery performance with applied gas cooler air mass flowrate and traction current disturbance

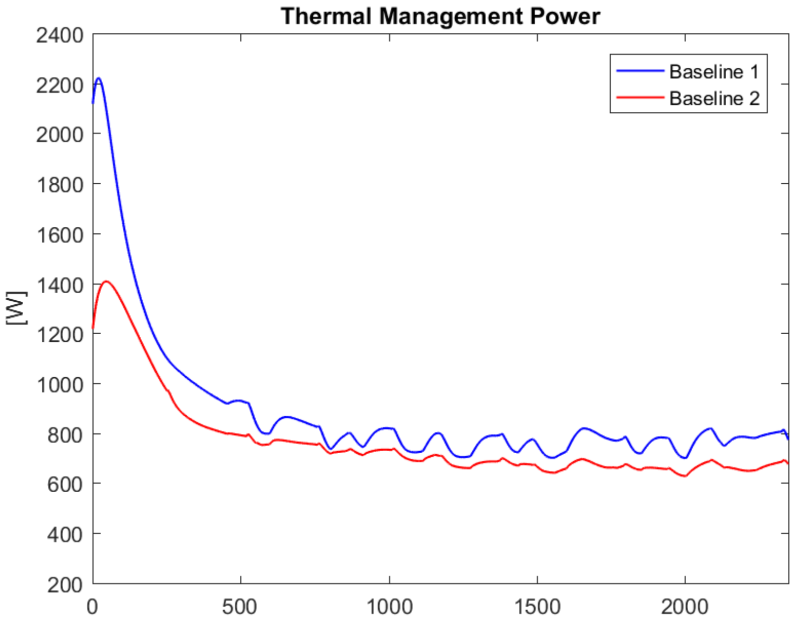

Figure 4.25 Power consumption of combined Baseline controllers with applied gas cooler air mass flowrate and traction current disturbance

Chapter 5 Model Predictive Controller

Section 5.1 will introduce model predictive control (MPC) by providing an overview of the method, a literature review of its application to HVAC and electric vehicles, and a description of the formulation for linear MPC. Section 5.2 will explain the method to obtain linear models for the nonlinear air-cooled cabin, air-cooled battery plant. Section 5.3 will detail the formulation of the controller specific to this system. Section 5.4 will show the results of the MPC controller and compare it to the baseline controller described in Chapter 4.

5.1 Introduction to Model Predictive Control

Model predictive control (MPC) is a technique commonly used in industry for large, multi-variable, constrained problems. References [45], [46] provide a comprehensive review of the theory and history of model predictive control. This section will provide a brief overview of the MPC method. The model predictive controller uses a dynamic model that allows it to predict future states over a prediction horizon. At each time step, a finite-horizon, open-loop, optimal control problem is solved to determine the optimal control input trajectory to minimize a cost function, with respect to the system dynamics and constraints. The first input of the optimized input trajectory is applied to the plant. At each time step the measured current state is provided to the controller, thus shifting one step forward the state and control sequence. This is referred to as receding horizon and contributes to the robustness of MPC. Figure 5.1 describes the MPC method visually. The controller receives feedback from the plant by providing the initial condition. The optimal control problem is open-loop because the modeled state trajectory over the prediction horizon does not include feedback of the actual states at those time steps. Therefore, the implemented control inputs can vary from what is predicted at each time step. The objective function of an MPC penalizes quantities of interest to the designer, usually this includes reference tracking and input minimization. Furthermore, MPC can handle constraints well, including bounds on actuator commands or a system state. Due to the model-based nature of MPC, it is capable of capturing the coupling within a system that PID controllers cannot account for. Comparatively, decentralized PID controllers can suffer from excess use of energy, setpoint overshoot, and competing controllers due to system coupling.

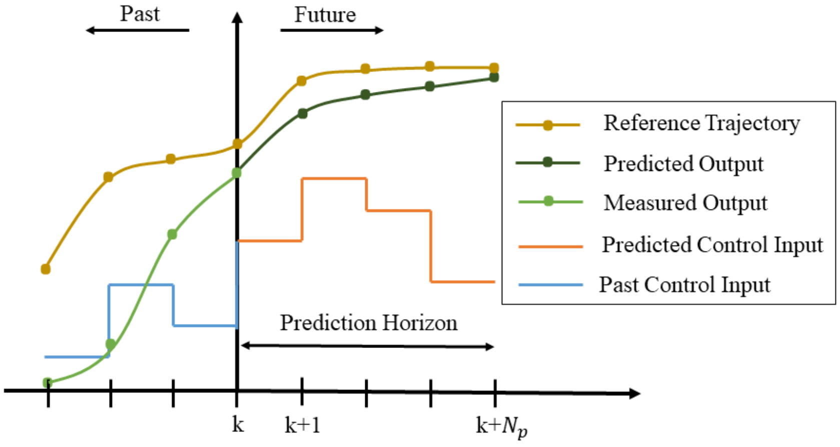

Figure 5.1 Model predictive controller past and future behavior at each time step

5.1.1 Literature Review

Model predictive control techniques have been applied extensively for building HVAC systems. Reference [47] provides a review of the key contributions to this area. For HVAC control design, the MPC attempts to minimize temperature error and minimize power consumption. Additionally, there exists MPC work specific to electric vehicle thermal management. Reference [48] implemented a nonlinear model predictive controller (NMPC) to manage the cabin temperature of an electric vehicle with the intent to extend MPC to regulating both the cabin and battery pack temperature in future work. They use a cooling configuration in which the vapor compression system cools water that is split between two cooling loops: cabin and battery pack. The controlled actuators are the compressor, expansion valve, and a 3/2-way-valve. They found that the NMPC performs better than a baseline decentralized PI approach, exhibiting faster convergence to the setpoint with minimal overshoot and quicker response to unknown disturbances. Reference [49] used nonlinear MPC for thermal management of hybrid electric vehicle battery and power electronics and found that it could maintain the battery in a healthy temperature range while consuming 5% less electrical energy. Reference [50] investigated the use of model predictive control for cabin heating that minimizes power consumption by effectively distributing the load among a heater core and electrical heater. This work distinguishes itself by applying linear MPC to an entirely air-cooled cabin and battery pack with a single-loop transcritical vapor compression system. Linear MPC is chosen because it is computationally faster and cheaper to implement than nonlinear MPC. Similarly, the chosen air-cooled configuration provides benefits of simplicity and reduced cost in comparison to liquid cooled systems. This work proposes that a linear MPC can allow for effective and efficient cooling of the battery pack and cabin with the air-cooled system.

5.1.2 Formulation

This section outlines the formulation for a linear MPC. The controller utilizes a discrete, linear model with $x \in \mathbb{R}^n, u \in \mathbb{R}^m$, and $y \in \mathbb{R}^p$, and matrices $A \in \mathbb{R}^{nxn}, B \in \mathbb{R}^{nxm}, C \in \mathbb{R}^{pxn}$, and $D \in \mathbb{R}^{pxm}$.

$$\begin{aligned} x[k+1] &= Ax[k] + Bu[k] \\ y[k] &= Cx[k] + Du[k] \end{aligned} \tag{5.1}$$

A controller prediction and control horizon are defined, N_p and N_u respectively ($N_p \geq N_u$). Longer prediction horizons can improve the performance of the MPC because it can predict further out into the future, but at the cost of computational time. The benefit of a control horizon less than the prediction horizon is the reduced computational cost by providing the optimizer fewer decision variables, while still providing it with a long prediction horizon to foresee the impact of its decisions. The current state at time k, $x[k \mid k]$, is provided to the controller and predicts the future states, $x[k+j+1 \mid k]$ for $j = 0...(N_p - 1)$, based on a predicted control sequence, $u[\cdot \mid k]$. The predicted future states and control sequence are determined in order to minimize the cost function and adhere to the constraints of the following form:

$$\begin{aligned} \underset{u[\cdot|k]}{\text{minimize}} \quad & J = \sum_{j=0}^{N_p-1} f\left(x[k+j+1 \mid k], y[k+j \mid k], u[k+j \mid k]\right) \\ \text{subject to} \quad & \underline{U} \leq u[k+j \mid k] \leq \overline{U} \\ & \underline{X} \leq x[k+j+1 \mid k] \leq \overline{X} \\ & \underline{Y} \leq y[k+j \mid k] \leq \overline{Y} \\ & x[k+j+1 \mid k] = Ax[k+j \mid k] + Bu[k+j \mid k] \end{aligned} \tag{5.2}$$

The objective function is a function of the predicted states, outputs, and inputs and most commonly formulated as a 2-norm. The actuator inputs, $u[k+j\,|\,k]$, are constrained within a lower and upper bound of operation, i.e. a fan command between 0 and 100%, etc. The states, $x[k+j+1|\,k]$, and outputs, $y[k+j\,|\,k]$, may be bounded, i.e. upper and lower bound on a temperature state of interest. The last constraint is the linear dynamics that the predicted state sequence must obey with respect to the predicted inputs. As mentioned previously, the first control input of the optimized sequence is applied to the plant and then at time k+1 the process is repeated. This procedure is reiterated concisely in the steps below:

1. Provide MPC the current plant states $x[k\,|\,k]$
2. Optimize future states and future inputs, $x[\cdot\,|\,k]$ and $u[\cdot\,|\,k]$ respectively, by solving control problem 5.2
3. Apply the first control input, $u[k\,|\,k]$, to the plant
4. At time k=k+1, repeat from Step 1

5.2 System Identification

To implement linear MPC requires a discrete, linear model of the system dynamics. This section will describe how linear models were identified and combined for the air-cooled cabin, air-cooled battery pack system. Chapter 2 described the nonlinear models developed for the transcritical vapor compression system, battery pack, and vehicle cabin. In this section, standard 'black box' system identification techniques from the Matlab System Identification Toolbox [51] are used to obtain linear state-space models for each system. First, a random binary signal (RBS) of each input(/disturbance), around a nominal value, is applied to the nonlinear system and output data is collected (sampled every 1 seconds). Then, the algorithm uses the Input/Output (I/O) data and minimizes prediction errors to obtain a maximum likelihood system. Figure 5.2 illustrates the method of 'black box' system identification.

Outputs from each system were chosen based on what could conceivably be measured in a physical system, such as temperatures and pressures. Beyond that, trial-and-error was used to find I/O combinations that provided a good fit between the linear model and nonlinear system. When possible, the model order was chosen to match the number of outputs so that an observer would not be required to provide states to the MPC (and given matrix C_d is invertible). Inputs may include actuator inputs and measurable or predictable disturbances. As will be discussed in more detail later, disturbances that are known or can be estimated can be fed to the MPC controller to improve its performance. Once each subsystem linear model is identified, they are combined by sending relevant signals to one another as described in Section 5.2.4.

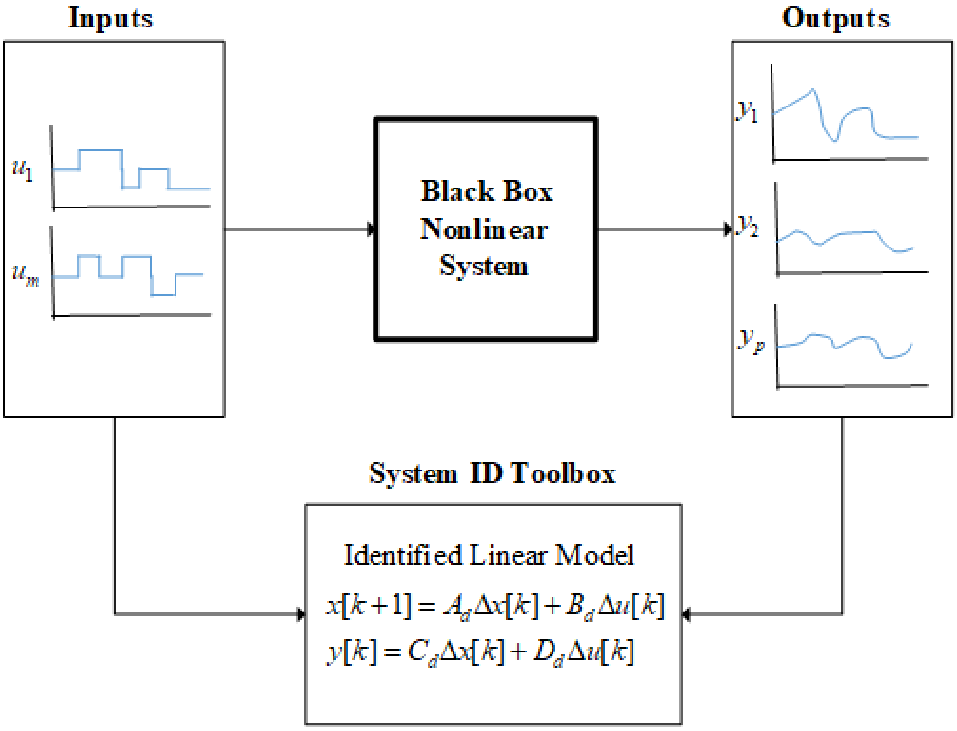

Figure 5.2 Black box system identification structure

5.2.1 Identified Transcritical VCS Model

The inputs for the transcritical VCS are from Rasmussen et al. [52], in which a transcritical vapor compression system reduced order model was identified. The outputs were modified from the paper to obtain a better fit for a greater range of input signal deviations. The internal heat exchanger wall temperature was chosen to characterize the slow dynamic associated with thermal capacitance of this heat exchanger.

$$u=\begin{bmatrix} u_{fan} & \omega_k & u_v & T_{gc,ai} & \dot{m}_{gc,a} & T_{e,ai} \end{bmatrix}^T \tag{5.3}$$

$$y=\begin{bmatrix} T_{e,ao} & P_e & P_{gc} & T_{w,IHX} \end{bmatrix}^T \tag{5.4}$$

The nominal value and perturbation deviation of the RBS signal is provided in Table 5.1. A 4th order model provided a good fit and does not require use of an observer because matrix C_d is invertible. The state space matrices are provided in Equation 5.5. To verify the identified model, another RBS signal was applied to the nonlinear system and linear model. The output data was collected from both and compared to confirm that the model consistently captures the dominant system behaviors. The results of this verification is shown in Figure 5.3 and shows that the fit is sufficient for control design.

$$
\begin{gathered}
A_d = \begin{bmatrix} 0.3206 & 0.0894 & 0.0937 & 0.0838 \\ 0.6215 & 0.7489 & -0.3906 & 0.4537 \\ 0.5381 & -0.1159 & 0.8309 & 0.0838 \\ -0.3481 & -0.1256 & 0.2335 & 0.7075 \end{bmatrix}, \\
B_d = \begin{bmatrix} -9.8860E-05 & -5.9332E-04 & 0.1569 & -3.1623E-04 & 7.1006E-04 & 3.0815E-05 \\ 4.4601E-04 & 1.4000E-03 & -0.2843 & -2.5240E-05 & 3.4740E-01 & 1.3000E-03 \\ -1.7336E-04 & 7.1094E-04 & -0.1630 & -1.6113E-04 & 9.7800E-02 & -1.1000E-03 \\ -3.9634E-04 & -7.8148E-04 & 0.1654 & 5.3570E-04 & -2.2500E-01 & -1.4000E-03 \end{bmatrix}, \\
C_d = \begin{bmatrix} -2.7845 & -0.7603 & -4.3567 & -3.9634 \\ 1.6962E+03 & 552.8532 & -785.4314 & 759.6072 \\ 216.0754 & 3.5950E+03 & -1.7855E+03 & 4.0041E+03 \\ -3.5590 & 19.4110 & -10.0501 & 25.5733 \end{bmatrix}, \\
D_d = \begin{bmatrix} 0 & 0 & 0 & 0 & 0 & 0 \\ 0 & 0 & 0 & 0 & 0 & 0 \\ 0 & 0 & 0 & 0 & 0 & 0 \\ 0 & 0 & 0 & 0 & 0 & 0 \end{bmatrix}
\end{gathered}
\tag{5.5}
$$

Table 5.1 Transcritical VCS system ID inputs

	Nominal Value	Perturbation Deviation
Evaporator Fan Speed [%]	50	0.15
Compressor Speed [RPM]	1800	0.15
Valve Opening [%]	8	0.05
Ambient Temp. [C]	35	0.15
GC Air massflow rate [kg/s]	0.5	0.05
Evap. Inlet Temp. [C]	30	0.15

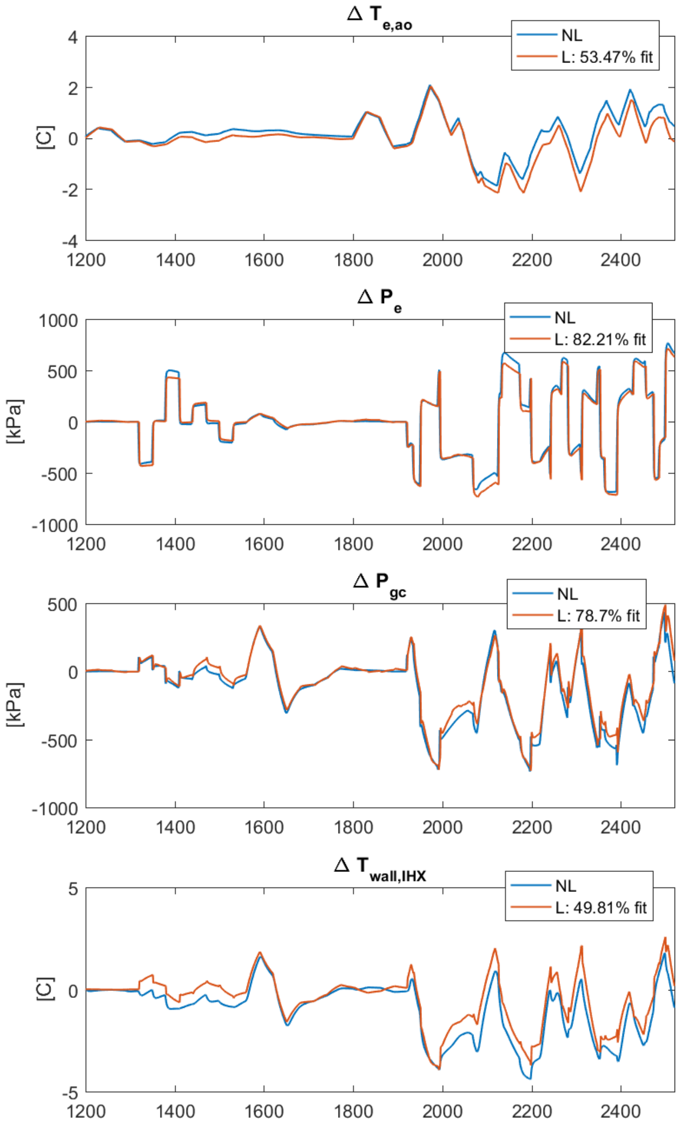

Figure 5.3 Verification of identified linear VCS model with RBS input signal different from signal for identification

5.2.2 Identified Battery Pack Model

The external inputs and disturbances to the battery pack model are the current, and the cooling air inlet temperature and mass flowrate. The nominal values and deviations are provided in Table 5.2. The output states that are most valuable for thermal management are the mean surface temperature and mean core temperature. Several output combinations were tested to determine the set that would capture the system dynamics most precisely. Output set y_2 included the cooling fluid outlet temperature and output set y_3 included the battery pack voltage. The motivation to try these sets was to see if knowledge of these other dynamics, that influence the temperatures of interest, would provide a better model fit to the plant. However, it was consistently found that output set y_1 provided the best fit for a 2nd order system (Equation 5.10). Verification of the linearized model against the nonlinear model is shown in Figure 5.4. There is greater deviation of the core temperature as the simulation time increases; this could be a result of the dependence of resistive and capacitive values on state of charge (a nonlinearity not captured with the identified linear model). This in turn affects the heat generated by each cell.

$$u = \begin{bmatrix} u_{fan} & T_{fl,in} & \bar{I} \end{bmatrix}^T \tag{5.6}$$

$$y_1 = \begin{bmatrix} T_{surf}^{mean} & T_c^{mean} \end{bmatrix}^T \tag{5.7}$$

$$y_2 = \begin{bmatrix} T_{surf}^{mean} & T_c^{mean} & T_{fl}^{out} \end{bmatrix}^T \tag{5.8}$$

$$y_3 = \begin{bmatrix} T_{surf}^{mean} & T_c^{mean} & \bar{V}_{out} \end{bmatrix}^T \tag{5.9}$$

$$\begin{aligned}
A_d &= \begin{bmatrix} 0.8967 & -0.0186 \\ -0.2364 & 0.9572 \end{bmatrix}, \\
B_d &= \begin{bmatrix} -1.3437E-04 & 0.0025 & 1.6600E-05 \\ -2.8827E-04 & 0.0054 & 3.7108E-06 \end{bmatrix}, \\
C_d &= \begin{bmatrix} 20.0171 & -1.0353 \\ 21.7475 & -9.7025 \end{bmatrix}, \\
D_d &= \begin{bmatrix} 0 & 0 & 0 \\ 0 & 0 & 0 \end{bmatrix}
\end{aligned} \tag{5.10}$$

Table 5.2 Battery pack system ID inputs

	Nominal Value	Perturbation Deviation
Batt. Fan Speed [%]	30	0.5
Inlet Coolant Temp. [C]	26.5	0.2
Current [A]	100	0.5

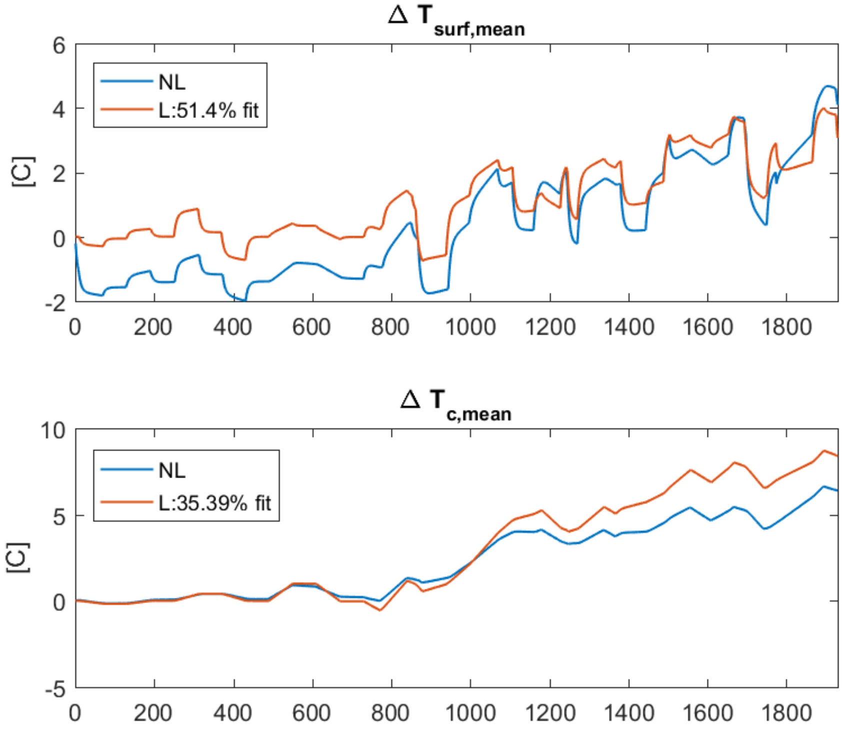

Figure 5.4 Verification of identified linear battery pack model with RBS input signal different from signal for identification

5.2.3 Identified Cabin Model

The inputs considered for system identification of the cabin are the evaporator fan speed, evaporator air outlet temperature and the ambient temperature. All other disturbances are considered unmeasurable and so are not included in the identification. The output is the cabin air temperature. As expected from the derivation of the cabin, a first order model captures the dynamics of the nonlinear system (Equation 5.13). Verification of the linearized model is shown in Figure 5.5.

$$u = \begin{bmatrix} u_{fan} & T_{e,ao} & T_{amb} \end{bmatrix}^T \tag{5.11}$$

$$y = T_{a,cab} \tag{5.12}$$

$$\begin{aligned} &A = 0.9756, \\ &B = \begin{bmatrix} -.0024 & 0.0176 & 0.0031 \end{bmatrix}, \\ &C = 1, \\ &D = \begin{bmatrix} 0 & 0 & 0 \end{bmatrix} \end{aligned} \tag{5.13}$$

Table 5.3 Cabin system ID inputs

	Nominal Value	Perturbation Deviation
Evap. Fan Speed [%]	50	0.25
Evap. Air Outlet Temp. [C]	16	0.25
Ambient Temp. [C]	35	0.25

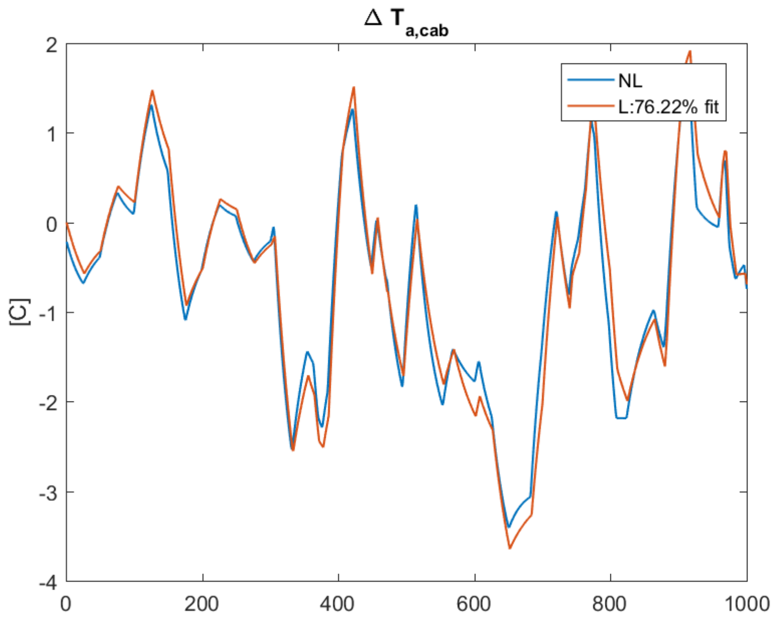

Figure 5.5 Verification of identified linear cabin model with RBS input signal different from signal for identification

5.2.4 Combined Identified Model

The previously identified models can be connected to give a linear system for the air-cooled cabin, air-cooled battery system. A summary of each subsystem's inputs, outputs, and matrix dimensions are provided in Table 5.4. The three identified models have a combined total of 12 inputs and 7 outputs. In the combined system, two of the outputs become internal signals. The evaporator air outlet temperature from 'Model 1' is input to 'Model 2' and the cabin air temperature output form 'Model 2' is input to 'Model 3' as the inlet coolant temperature. This structure is shown in Figure 5.6. Furthermore, the linear model outputs were verified against the nonlinear plant. Figures 5.7-5.8 show that the dominant dynamics are captured for each output. It should be noted that errors in the evaporator air temperature cascade down to the cabin temperature and battery temperatures, as a result of the chosen cooling structure. The errors remain relatively small (within 10%) which makes the models suitable for control design. More importantly for MPC, the linear model captures the correct shape and relative change of the output values. Since an updated initial condition is provided to the MPC at each time step, the model error would likely be less significant than shown in Figure 5.8.

Table 5.4 Subsystem I/O's for system identification

	Subsystem	*I/O's*	*Matrix Dimensions*
Model 1	Transcritical VCS	$u = \begin{bmatrix} u_{fan} & \omega_k & u_v & T_{gc,ai} & \dot{m}_{gc,a} & T_{e,ai} \end{bmatrix}^T$ $y = \begin{bmatrix} T_{e,ao} & P_e & P_{gc} & T_{w,IHX} \end{bmatrix}^T$	A_1 - 4x4 B_1 - 4x6 C_1 - 4x4 D_1 - 4x6
Model 2	Cabin	$u = \begin{bmatrix} u_{fan} & T_{e,ao} & T_{amb} \end{bmatrix}^T$ $y = T_{a,cab}$	A_2 - 1x1 B_2 - 1x3 C_2 - 1x1 D_2 - 1x3
Model 3	Battery Pack	$u = \begin{bmatrix} u_{fan} & T_{fl,in} & \bar{I} \end{bmatrix}^T$ $y = \begin{bmatrix} T_{surf}^{mean} & T_c^{mean} \end{bmatrix}^T$	A_3 - 2x2 B_3 - 2x3 C_3 - 2x2 D_3 - 2x3

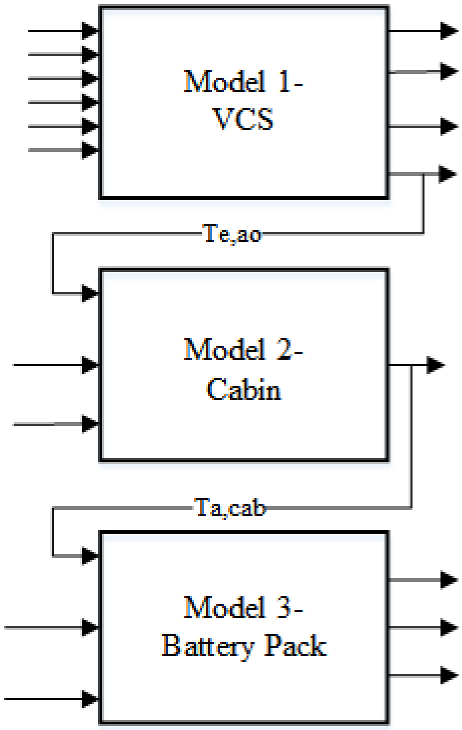

Figure 5.6 Structure of linear model of air-cooled cabin, air-cooled battery pack configuration

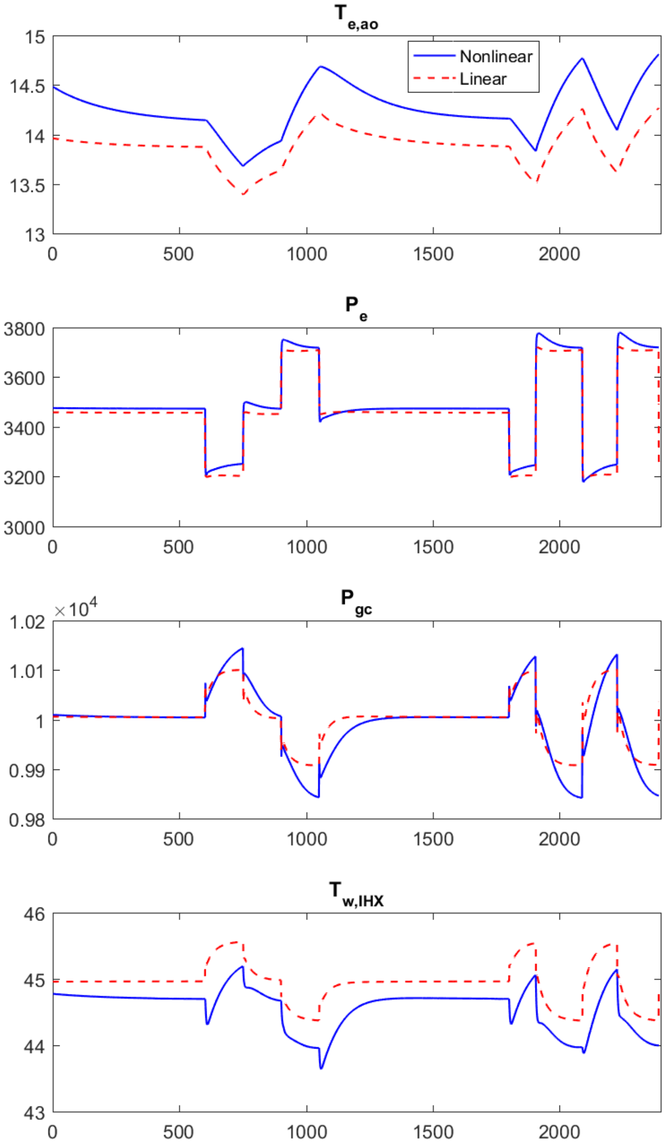

Figure 5.7 Verification of VCS outputs for combined system identified linear model. Green box emphasizes the evaporator air outlet temperature that cascades to cabin and battery temperatures

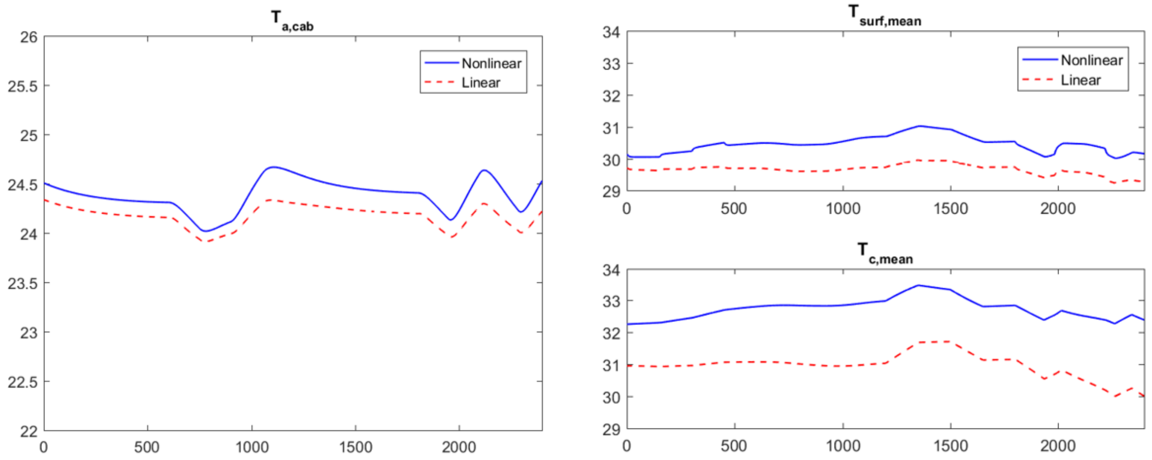

Figure 5.8 Verification of cabin and battery pack outputs for combined system identified linear model

5.3 Controller Formulation

In the battery electric vehicle system modeled, the objectives of interest are maintaining the cabin space at a comfortable temperature, regulating the battery pack temperature to be within the optimal range, and minimizing power consumption of the transcritical vapor compression system. These goals will be designed into the model predictive controller via the framework previously described in Section 5.1 and with the linear models obtained in Section 5.2. The controllable inputs are the fan speeds, u_{fan}^{evap} and $u_{fan}^{battery}$, the valve opening, u_v, and the compressor speed, ω_k. These will be the outputs of the MPC. Furthermore, the remaining linear model inputs are the measureable and unmeasurable disturbances, notated as d_1, d_2, d_3, and d_4, representing T_{amb}, $\dot{m}_{gc,a}$, $T_{e,ai}$, and $\bar{I}$ respectively. The objective function (Equation 5.14) and constraints (Equations 5.15-5.17) are formulated as:

$$
\begin{aligned}
J = \sum_{j=0}^{N_p-1} & q_1 \left| r_{T_{a,cab}} - T_{a,cab}[k+j+1] \right|^2 + q_2 \left| r_{T_c^{mean}} - T_c^{mean}[k+j+1] \right|^2 \\
& + r_1 \left| u_{fan}^{evap}[k+j] \right|^2 + r_2 \left| u_{fan}^{batt}[k+j] \right|^2 + r_3 \left| \omega_k[k+j] \right|^2 \\
& + \delta_1 \left| s_1[k+j] \right|^2 + \delta_2 \left| s_2[k+j] \right|^2 + \delta_3 \left| s_3[k+j] \right|^2 \\
& + \gamma_1 \left| u_{fan}^{evap}[k+j] - u_{fan}^{evap}[k+j-1] \right|^2 + \gamma_2 \left| u_{fan}^{batt}[k+j] - u_{fan}^{batt}[k+j-1] \right|^2 \\
& + \gamma_3 \left| u_v[k+j] - u_v[k+j-1] \right|^2 + \gamma_4 \left| \omega_k[k+j] - \omega_k[k+j-1] \right|^2
\end{aligned}
\tag{5.14}
$$

$$
\begin{aligned}
x_1[k+j+1] &= A_1 x[k+j] + B_1 \left[u_{fan}^{evap}[k+j] \quad \omega_k[k+j] \quad u_v[k+j] \quad d_1[k+j] \quad d_2[k+j] \quad d_3[k+j] \right]^T \\
x_2[k+j+1] &= A_2 x[k+j] + B_2 \left[u_{fan}^{evap}[k+j] \quad C_1(1,:) * x_1[k+j] \quad d_1[k+j] \right]^T \\
x_3[k+j+1] &= A_3 x[k+j] + B_3 \left[u_{fan}^{batt}[k+j] \quad C_2 * x_2[k+j] \quad d_4[k+j] \right]^T
\end{aligned}
\tag{5.15}
$$

$$
\begin{aligned}
\underline{u}_{fan}^{evap} \le u_{fan}^{evap}[k+j] \le \bar{u}_{fan}^{evap} \\
\underline{u}_{fan}^{batt} \le u_{fan}^{batt}[k+j] \le \bar{u}_{fan}^{batt} \\
\underline{u}_{v} \le u_{v}[k+j] \le \bar{u}_{v} \\
\underline{\omega}_k \le \omega_k[k+j] \le \bar{\omega}_k
\end{aligned}
\tag{5.16}
$$

$$
\begin{aligned}
\underline{T}_{a,cab} - s_1[k+j] \le T_{a,cab}[k+j+1] \le \bar{T}_{a,cab} + s_1[k+j] \\
\underline{T}_c^{mean} - s_2[k+j] \le T_c^{mean}[k+j+1] \le \bar{T}_c^{mean} + s_2[k+j] \\
\underline{P}_{gc} - s_3[k+j] \le P_{gc}[k+j+1] \le \bar{P}_{gc} + s_3[k+j]
\end{aligned}
\tag{5.17}
$$

The first two objective function terms of Equation 5.14 penalize cabin and mean core battery temperature deviations from references $r_{T_{a,cab}}$ and $r_{T_c^{mean}}$ with weightings q_1 and q_2. These weightings should be relatively small compared to the penalty for deviations outside the constrained temperature region. The purpose of the first two terms is to provide additional guidance of where the system should try to operate. Terms 3-5 penalize power consumption of the power consuming actuator inputs, namely the evaporator fan, battery fan, and the compressor with weightings r_1, r_2, and r_3. It is assumed that power consumption to change the valve opening is negligible. Furthermore, constraints for the cabin and mean core battery temperature are defined with a 'slack' variable, s_i. The slack variables allow the system to operate outside the constrained region without causing an error in the optimizer, but at relatively large penalty compared to the other cost function terms. The gas cooler pressure is also constrained with a slack variable to maintain the pressure within transcritical operating range, but below a maximum pressure where safety of the compressor may be compromised due to a high outlet temperature. The slack objective terms (6-8) are penalized with weightings δ_1, δ_2, and δ_3. Finally, terms 9-12 penalize the rate of change of the actuator commands with weightings γ_1, γ_2, γ_3, and γ_4.

If a disturbance were to be unknown to the MPC, then its value would be assumed to remain constant at the nominal value for which the system was linearized (Equation 5.18). Known disturbances are measurable and/or predictable. A disturbance may be measureable at each time step, but not known for the rest of the prediction horizon. This disturbance value would be assumed constant at the value measured at time k over the prediction horizon (Equation 5.19). Other disturbances may be known or predicted with some level of certainty for the duration of the controller time. In the case of the system in consideration, an example 'known disturbance' is the current drawn from the traction motors, given a known velocity profile. Therefore, an estimate of the total current (d_4) can be provided to the controller for the entire prediction horizon. In general terms, a known disturbance can be provided as a discrete function $\Omega[k]$ (Equation 5.20). This concept is known as disturbance preview. Disturbance preview improves the controller performance by providing it with more knowledge of the systems behavior. The controller is able to see large deviations in a previewed disturbance and able to make proactive decisions to mitigate risk of violating a constraint or accumulating reference error.

$$\Delta d_i[k+j]=0 \tag{5.18}$$

$$\Delta d_i[k+j]=\Delta d_i[k] \tag{5.19}$$

$$\Delta d_i[k+j]=\Omega[k] \tag{5.20}$$

In this work, we assume that disturbances d_1 and d_3 are measureable at each time step, and that disturbances d_2 and d_4 can be predicted ahead of time based on a known velocity profile. The electrical current prediction is not perfect because it only accounts for the traction power. The additional current drawn from the transcritical vapor compression system remains unknown to the controller. The gas cooler air mass flow rate is a function of vehicle velocity. We assume that it can be predicted based on the change in current, assuming that if the current increases, then the vehicle is speeding up, therefore the air flow through the front of the vehicle also increases.

The tunable parameters in this controller are each of the weightings in the objective function $(q_1, q_2, r_1, r_2, r_3, \delta_1, \delta_2, \delta_3, \gamma_1 \gamma_2, \gamma_3, \gamma_4)$ and the prediction horizon (N_p).

5.4 Simulation Results

This section will test the MPC in simulation on the plant system. Recall that the plant is the nonlinear simulated system and the linear models are used by the MPC in the optimization problem. This is illustrated by Figure 5.9. The controller is programmed in Matlab/Simulink and using the YALMIP toolbox [53].

The objective function weightings were tuned by trial-and-error to achieve the desired performance. This process takes into account the magnitude differences of the states and inputs. For example, compressor speed and high side pressure are on the order of $10^3 - 10^4$, with changes on the order of magnitude of $10^1 - 10^3$. Temperatures are on the order of magnitude of 10^1 , with changes on the order of magnitude of $10^{-1} - 10^0$.

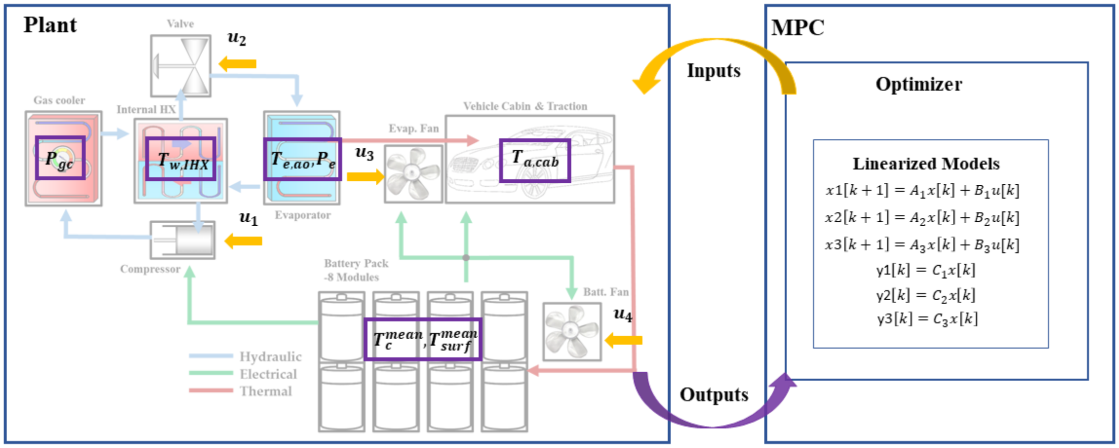

Figure 5.9 Interaction of nonlinear system plant and MPC that utilizes the linear system models

There are two categories of penalties: state penalties and actuator penalties. The state penalties are the weights on reference tracking and the slack variables. Comparatively, slack variables were weighted heavier than reference tracking. It is more important that these specific states do not violate constraints. Operation outside the optimal battery temperature range impacts the battery pack performance and life, and could potentially lead to safety issues. The cabin temperature constraint is for the purpose of passenger comfort, health and safety. The pressure constraint is for safety of the transcritical vapor compression system. The cabin is not forced to regulate the temperature strictly to the setpoint, because with the chosen architecture, the battery pack relies on the cabin air for cooling. In times of peak current, we are designing the controller to allow the cabin temperature to be brought down to the lower bound in order to provide additional cooling to the battery pack-- beyond the cooling that commanding the battery fan can achieve.

The actuator penalties are the weights on the control effort and on the rate of change. Comparatively, the rate of change of actuators is penalized heavier to ensure stability of the controller and reduce noise in the vehicle. Table 5.5 provides the state references and bounds and Table 5.6 the relative weightings of the four categories of objective function entries. The relative weightings were estimated based on scaling everything to approximately the same order of magnitude.

Table 5.5 State references and bounds for MPC

	$T_{a,cab}$	T_c^{mean}	P_{gc}
Reference	23	30	-
Upper Bound	24.5	35	12000
Lower Bound	21	20	8000

Table 5.6 Relative magnitudes of MPC weightings

Type	Category	Weightings	Relative Magnitude
State	*Reference*	q_1, q_2	$10^{-4} - 10^{-1}$
	Bounds	$\delta_1, \delta_2, \delta_3$	$10^{-1} - 10^{0}$
Actuator	*Effort*	r_1, r_2, r_3	$10^{-6} - 10^{-4}$
	Rate of Change	$\gamma_1 \gamma_2, \gamma_3, \gamma_4$	$10^{2} - 10^{3}$

The prediction horizon used is 120 seconds (2-minutes). The remainder of this chapter will look at the results of this controller with and without disturbance preview, and its performance relative to the baseline controllers discussed in Chapter 4.

5.4.1 Disturbance Preview Test

The results of this simulation is to show the benefits of disturbance preview. Disturbances T_{amb} and $\dot{m}_{gc,a}$ acting on the plant are held constant and the traction current $\overline{I}$ is cycled between 150 and 200 A for 2400 seconds (40 minutes) (Figure 5.10). ‘Controller 1’ receives a measurement of the current at each time step k, but does not have preview over the rest of the control horizon. It assumes that the disturbance is constant over the horizon as previously discussed in Section 5.3. ‘Controller 2’ receives preview of the current disturbance, thereby having knowledge of the traction current over the entire prediction horizon. Figure 5.11 shows a portion of the current disturbance profile. The red dashed line is the current that Controller 1 assumes at that time step for the optimization sequence. When the current is increasing, Controller 1 is continuously underestimating the current over the prediction horizon. When the current is decreasing, Controller 1 is overestimating the current over the prediction horizon. It will be shown that this lack of knowledge of Controller 1 results in excessive power consumption of the VCS compared to Controller 2.

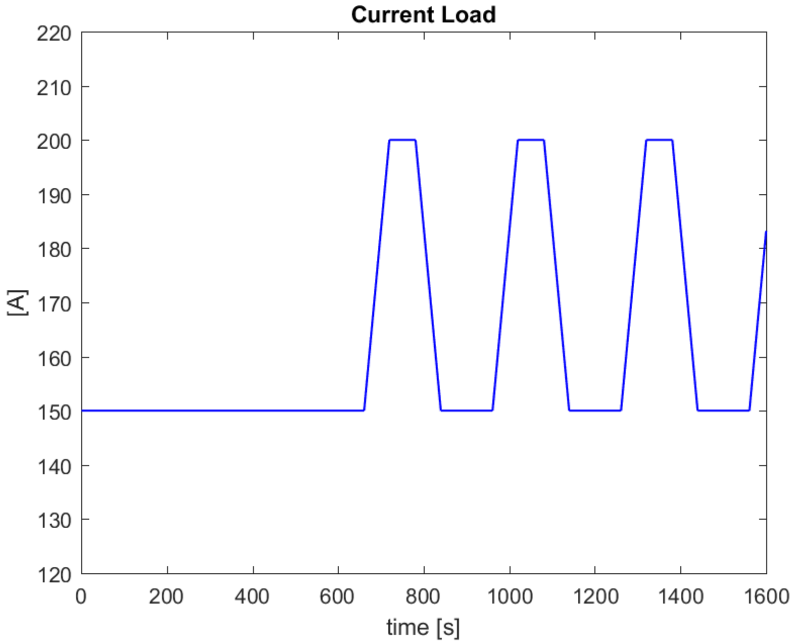

Figure 5.10 Traction current profile for disturbance preview test

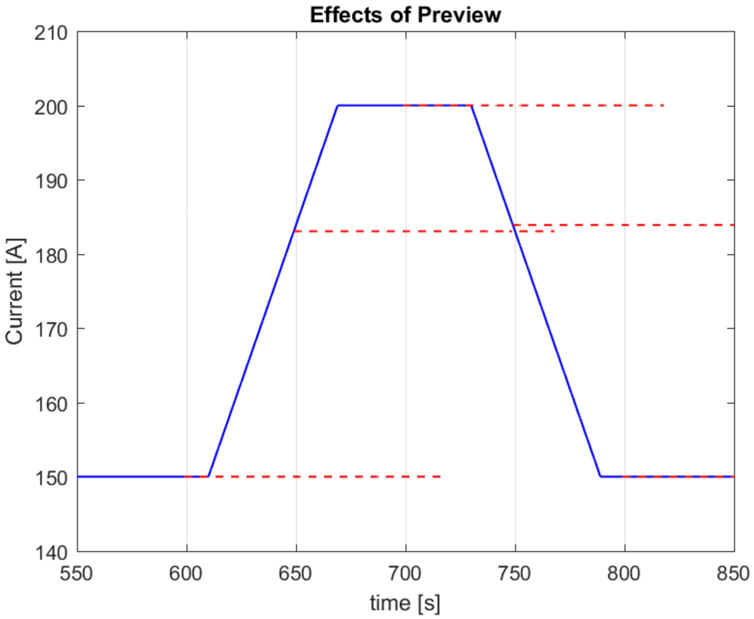

Figure 5.11 Traction current profile from 550-850 seconds. Red dashed line is the current assumed by Controller 1 for the prediction horizon at that time step

Figures 5.12-5.14 provide a comparison of the control inputs determined by each controller, the states of interest, and power metrics respectively. The cyclical under- and over-assumption of the current explains the lagging response and greater change in amplitude of Controller 1’s battery fan. It does not receive knowledge of the severity of the disturbance until it has to act drastically. Then it holds the fan speed at its maximum value for longer than required because it does not have knowledge that the current is decreasing. Furthermore, the controller responds to the peak disturbance signals by cooling the cabin to provide more cooling for the battery pack. It does this through aggressive changes in the compressor, evaporator fan and the valve opening. Both controllers are successful in maintaining the mean battery core temperature below the upper bound and the high side pressure within its thresholds. The state responses to Controller 1 are more oscillatory due to the oscillatory nature of the current load and the lack of disturbance knowledge. Controller 1 also violates the lower bound of the cabin temperature constraint twice, when it assumes that the current will remain at a peak value for a long time. Controller 1 has cyclical power peaks and over the duration of the simulation consumes about 25% more power than Controller 2, as determined by the integral of the power consumption provided in Table 5.7.

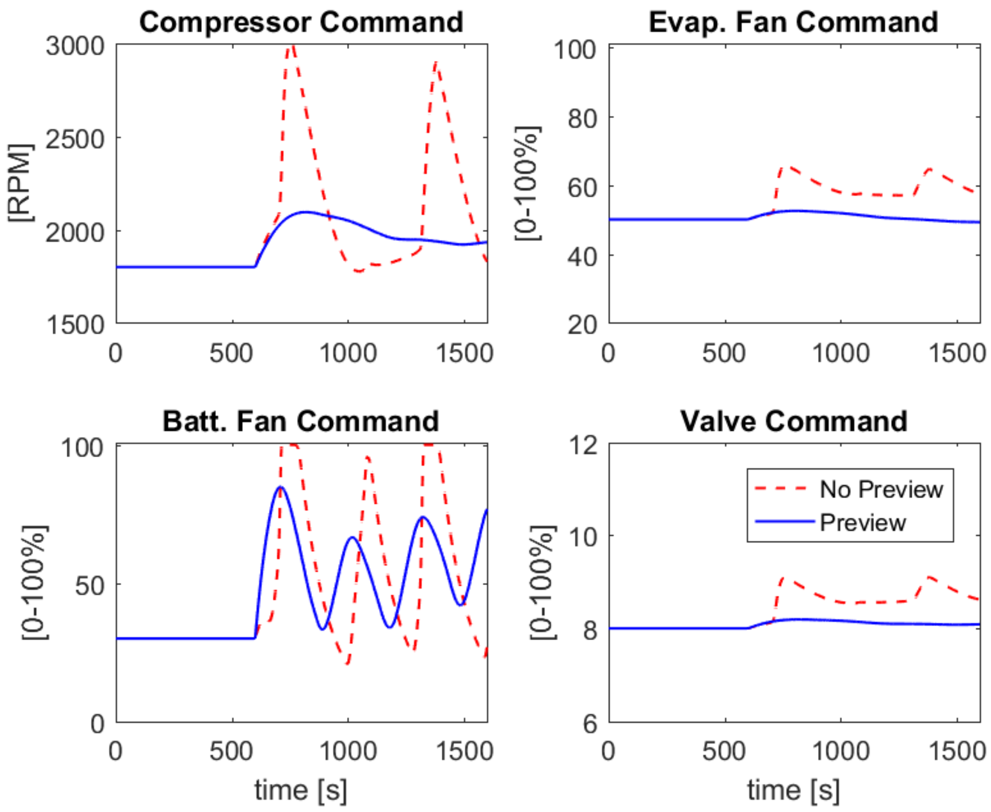

Figure 5.12 MPC input commands for Controller 1 (no preview) and Controller 2 (preview) for disturbance preview test

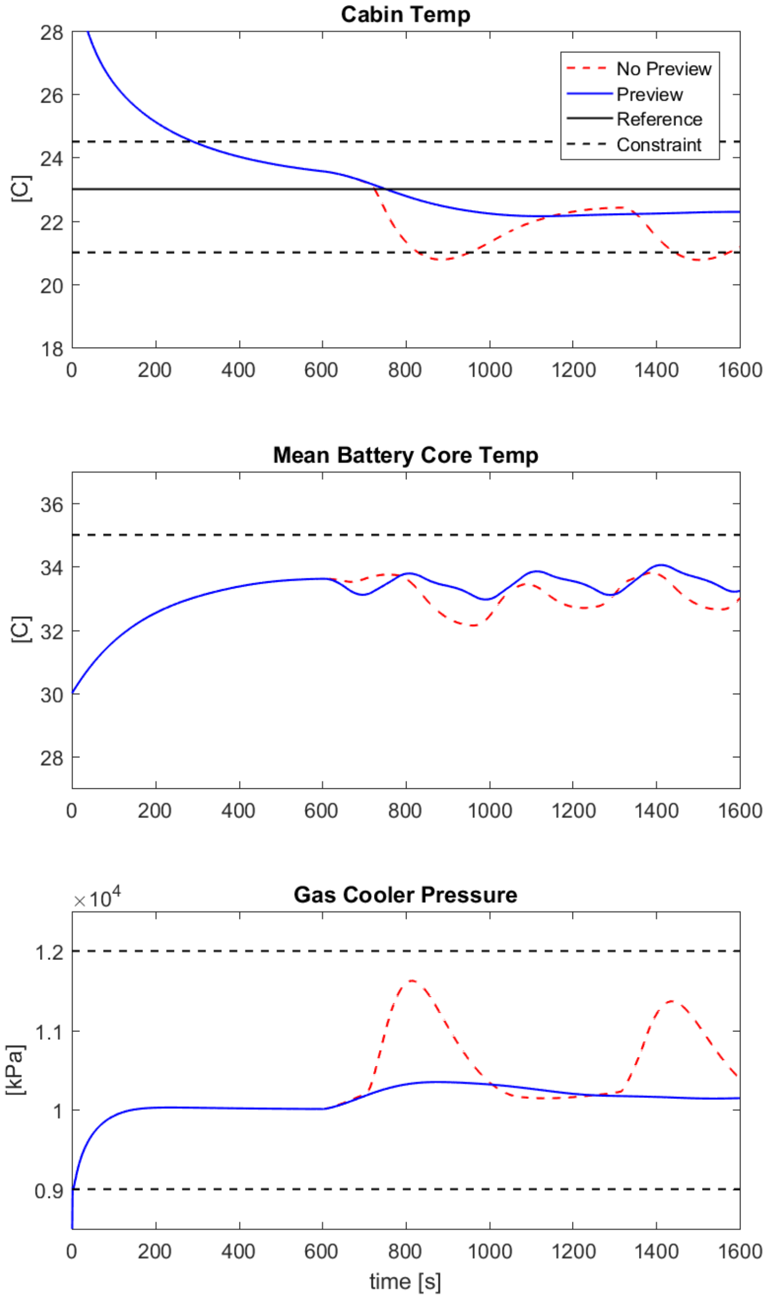

Figure 5.13 Constrained temperature and pressure state outputs for disturbance preview test

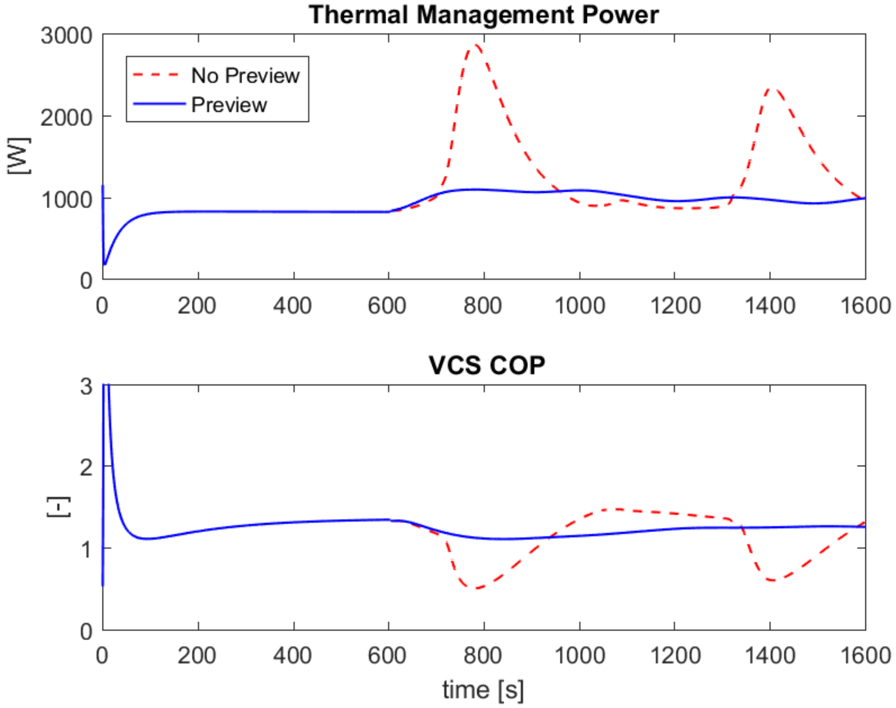

Figure 5.14 Power consumption of transcritical VCS and cycle COP for disturbance preview test

Table 5.7 Total work [J] of thermal management system – disturbance preview test

Controller 1	**Controller 2**
1.8156 E06	1.4756 E06

5.4.2 Drive Schedule Test

In this section, we test the MPC controller with the US06 (“Supplemental FTP”) driving schedule, provided in reference [54], and compare the performance to the baseline controllers. The US06 driving schedule is 600 seconds (10 minute) and includes periods of aggressive acceleration. It would be expected that this drive cycle would draw significant current that would heat up the battery pack over time. To extend the period of the test, the US06 drive cycle is repeated 4 times resulting in a 40 minute test shown in Figure 5.15.

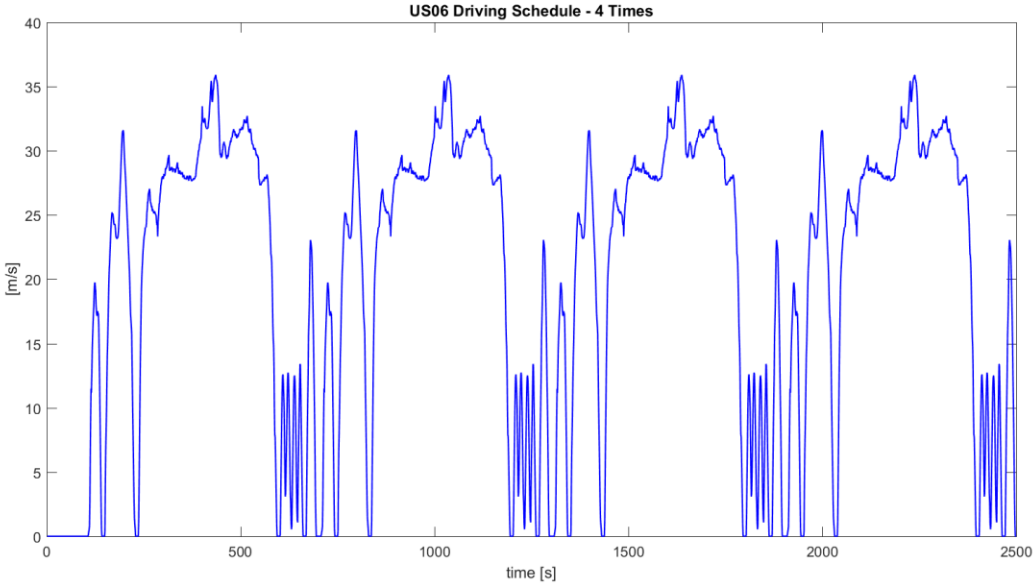

Figure 5.15 US06 driving schedule replicated 4 times (units of speed are m/s)

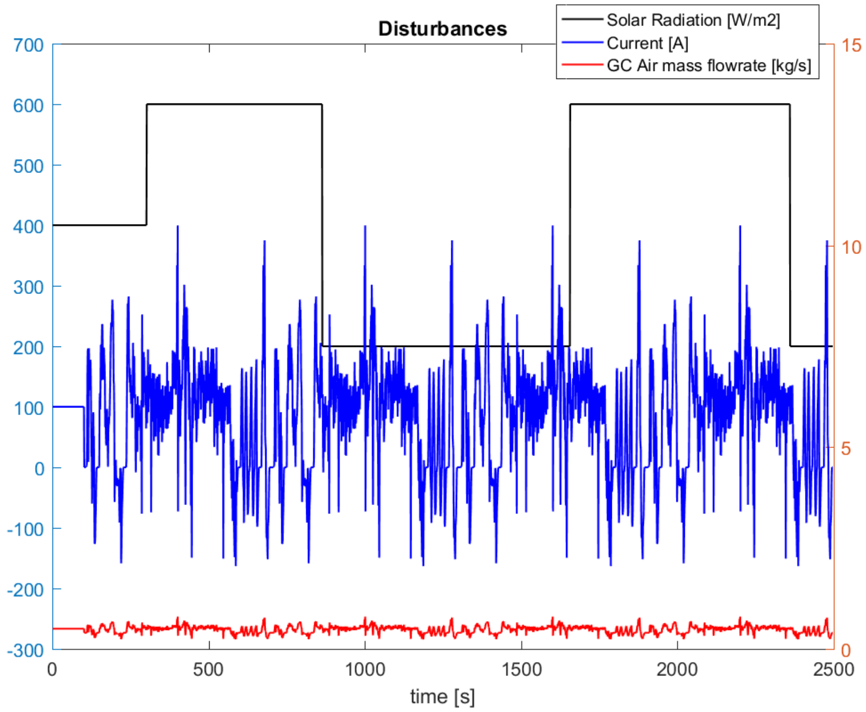

Figure 5.16 Disturbances applied to the plant during simulation

As described in Section 3.3.1, a current profile can be calculated from the velocity profile based on vehicle parameters. Disturbance loads are shown in Figure 5.16. The gas cooler air mass flow rate matches the changes of the current. A randomly generated solar radiation load was generated.

The MPC controller is provided preview of the traction current and gas cooler air mass flow rate. The controller receives imperfect current preview but perfect gas cooler air flow rate preview. The current previewed is solely the traction power and does not include the real-time VCS power consumption. The solar radiation disturbance is considered unknown to both the MPC and baseline controllers. The states of interest, actuator commands and ranges, and power metrics of each controller are shown in Figures 5.17-5.22. Recall, that Baseline 1 uses the compressor and evaporator fan to track cabin temperature and the valve to maintain the high side pressure within a desired operating range. Baseline 2 uses the compressor to track cabin temperature, the evaporator fan to track evaporator refrigerant superheat, and the valve to track an optimized pressure reference.

A summary of the relative performance of the controllers is provided by Table 5.9 and is explained in the following sections.

5.4.2.1 Temperature Regulation

Baseline 1 and the MPC are successful in managing temperature and pressure bounds for the entire simulation (Figure 5.17 and 5.18). Baseline 2 exceeds the upper bound for desired cabin temperature from about 100-300 seconds. This is likely caused by the decrease in evaporator fan speed to manage evaporator superheat. At approximately 1200-1500 seconds, Baseline 2 cabin temperature falls below the desired lower bound as a result of the decrease in solar radiation. Outside of those two regions, Baseline 2 is successful in managing temperatures and pressures. Degradation and reduced performance is mitigated by all of the controllers by keeping the battery temperature between 20-35 C. However, the MPC maintains the battery temperature closer to the maximum constraint. As mentioned in Chapter 1, battery packs operating at higher temperatures have lower internal resistance. As a result of maintaining a higher battery temperature, the MPC battery pack is operating at a slightly higher voltage than the Baseline controllers. This higher voltage, shown in Figure 5.19, provides improved performance because less current is drawn for the same power demanded.

5.4.2.2 Actuator Commands

Figure 5.20 shows time plots of the actuator commands determined by each controller. The baseline controllers often command the actuators across a greater range as compared to the MPC. Figure 5.21 provides the actuator operated ranges for each controller. The MPC operates within a smaller range with respect to the compressor and battery fan, and operates within a similar size range with respect to the evaporator fan and valve. Additionally, the Baseline controllers' actuation is more transient and aggressive. This is most evident when observing the battery fan speed for both Baseline controllers, the valve for Baseline 1, and the evaporator fan for Baseline 2. The main cause is that the baseline controllers are responding to error and attempting to track a specific set point. They are also unable to see upcoming changes in disturbances and understand the impact on the outputs. An additional cause of the aggressive actuation of Baseline 2 is the on-line pressure correction formula. The high-side pressure reference is updated every 300 seconds which causes a response in the valve, thus causing a response of the compressor and evaporator fan. The negative impact of this behavior is the accumulated wear and degradation of the actuators over time, in addition to excess system noise.

5.4.2.3 Power Consumption

The baseline controllers apply more control effort in the attempt to regulate to set points. The MPC is able to achieve the state objectives while consuming less power by using its knowledge of the system dynamics and disturbances. It also responds to unknown disturbances, such as the solar radiation, that are communicated through the updated states. When the solar radiation load changes, the cabin temperature deviates further from the setpoint and closer to the constraining bounds. Therefore, the MPC responds by providing more or less cooling. Additionally, it actuates the battery fan much less and holds the battery temperature closer to its upper bound to conserve energy. Table 5.8 provides a comparison of the integral of the power consumption (compressor power + evaporator fan power + battery fan power). Baseline 1 and Baseline 2 controllers consume approximately 27% and 18% more energy than the MPC, respectively. Of the two baselines, Baseline 2 exhibits improved efficiency, consuming about 7% less energy than Baseline 1.

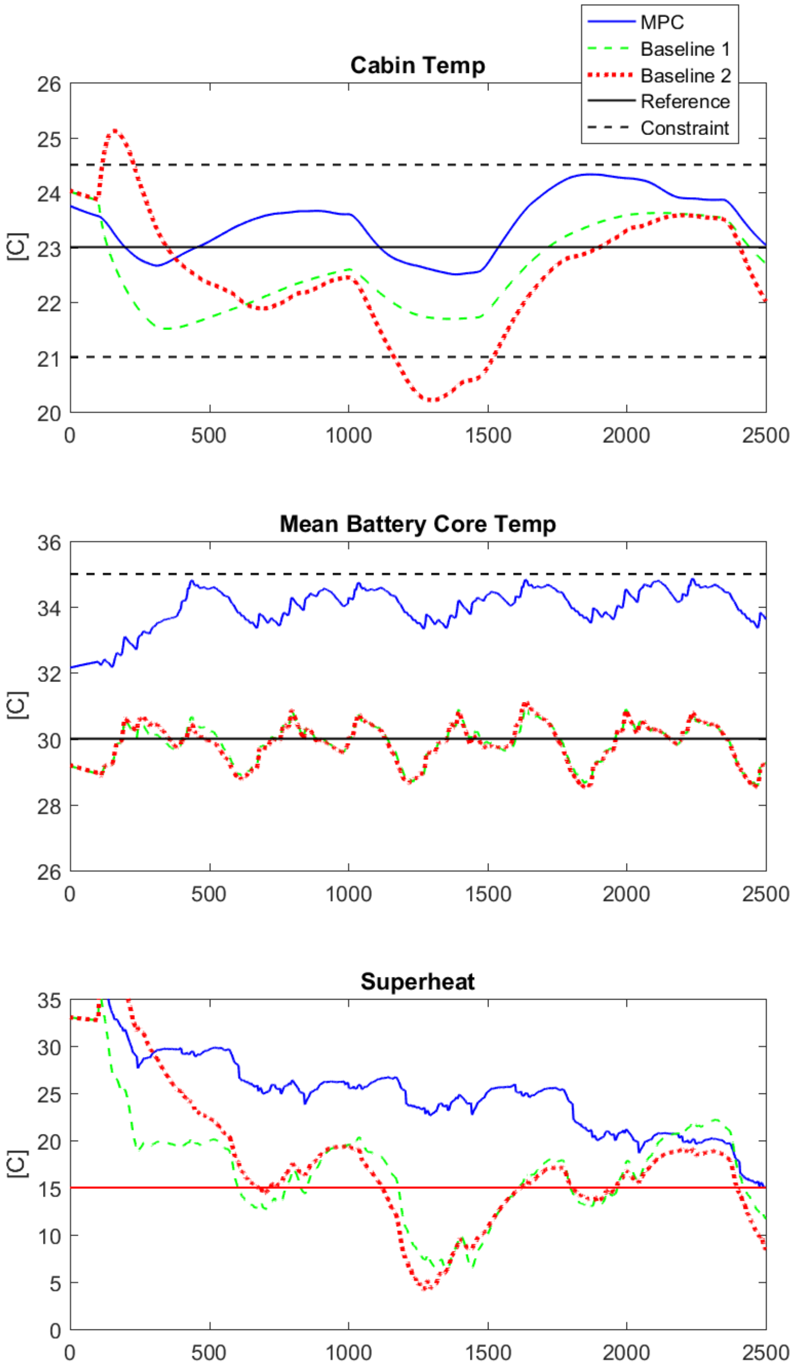

Figure 5.17 Temperature state outputs of MPC and Baseline controller drive cycle test

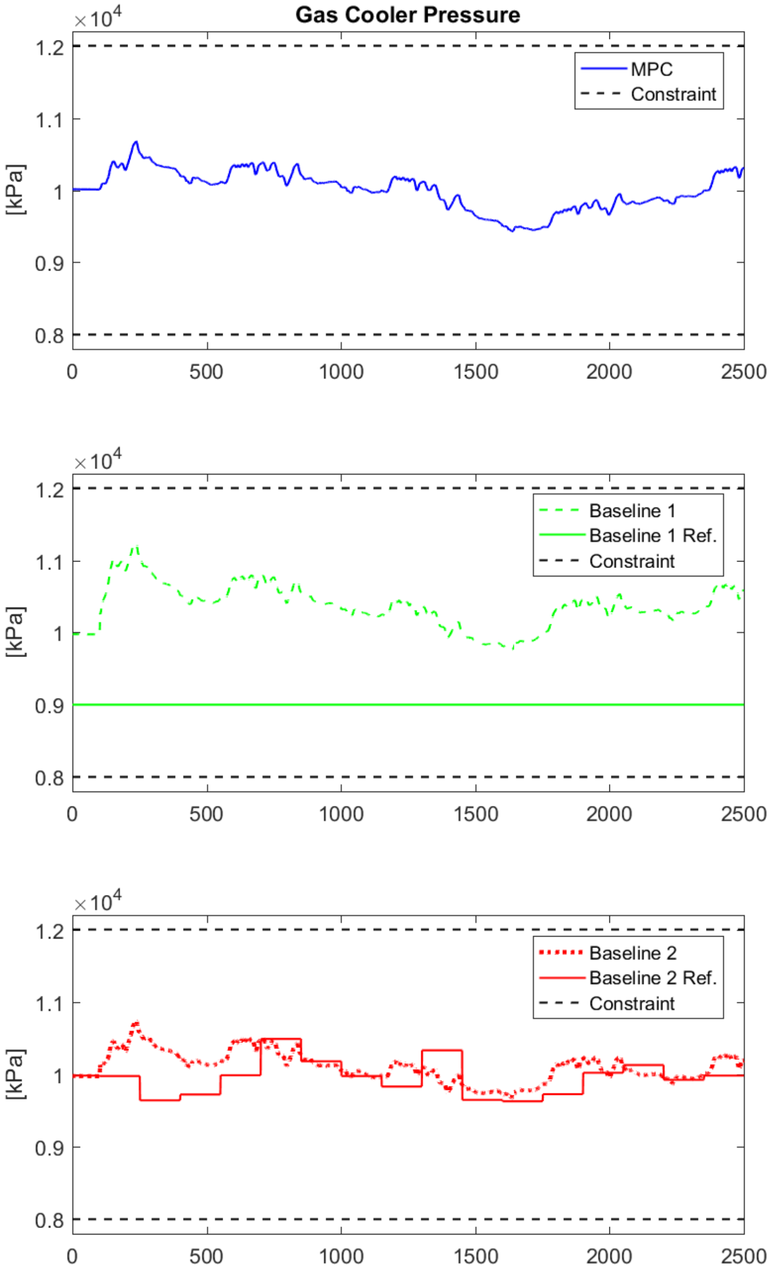

Figure 5.18 Pressure state outputs of MPC and Baseline controller drive cycle test

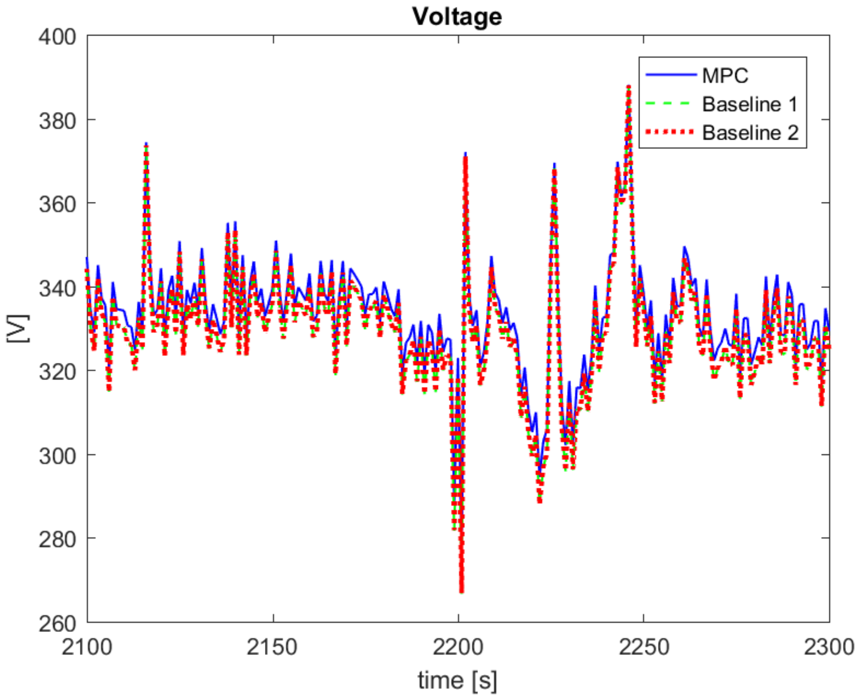

Figure 5.19 Pack voltage from portion of MPC and Baseline controllers drive cyle test

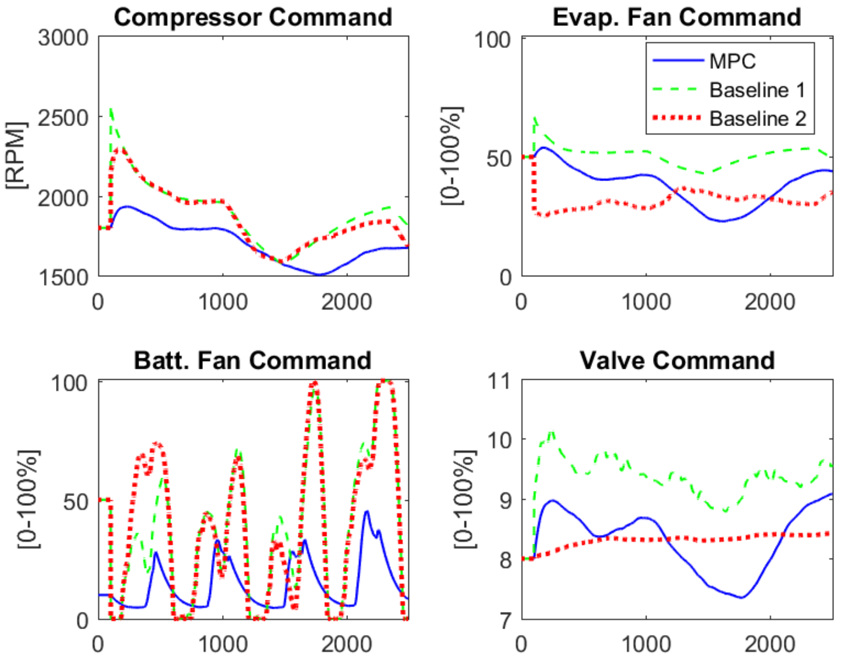

Figure 5.20 Input commands from MPC and Baseline controllers for drive cycle test

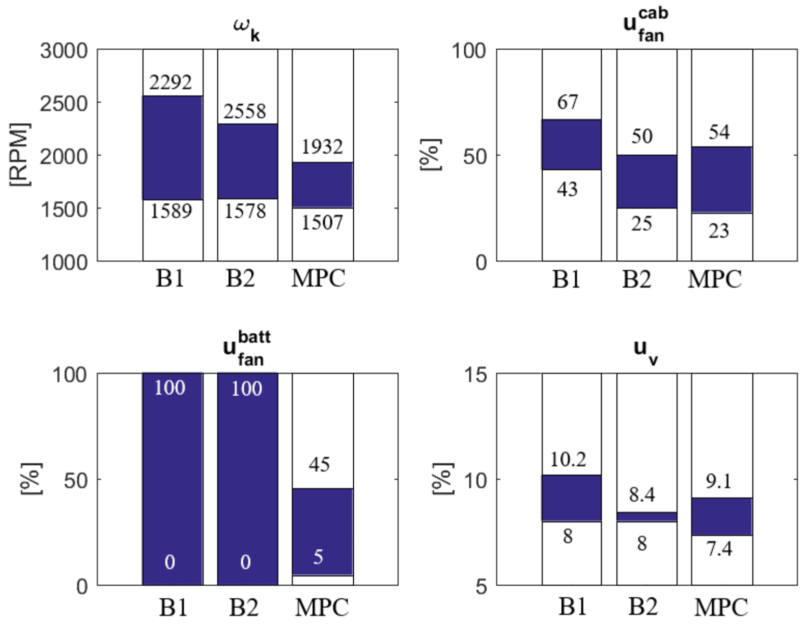

Figure 5.21 Range of actuator commands for Baseline 1 'B1', Baseline 2 'B2', and MPC in drive cycle test

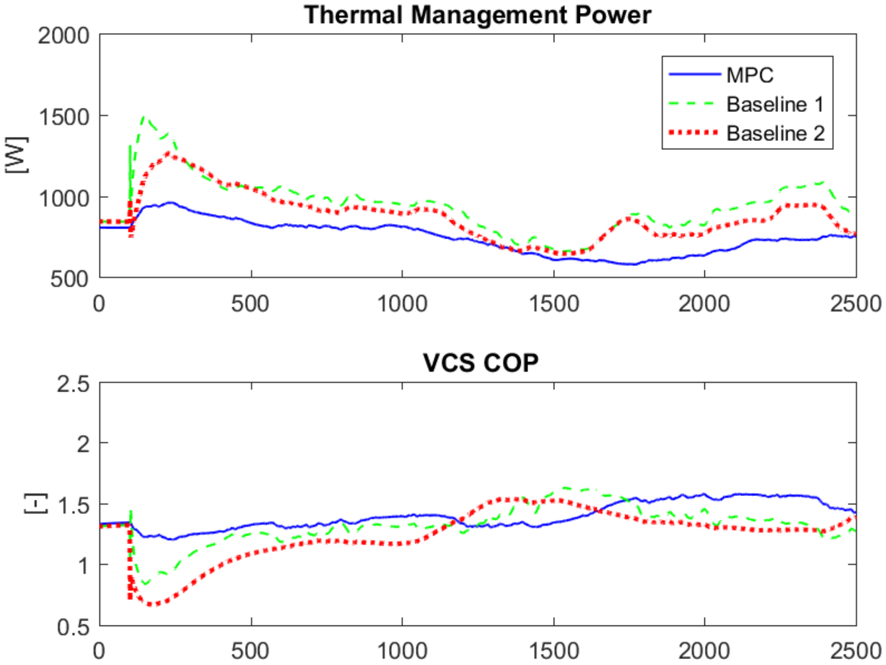

Figure 5.22 Power consumption of transcritical VCS and cycle COP from MPC and Baseline controllers drive cycle test

Table 5.8 Total work [J] of thermal management system – drive cycle test

Baseline 1	**Baseline 2**	**MPC**
2.3649 E06	2.2001 E06	1.8665 E06

Table 5.9 Peformance comparison of Baseline 1, Baseline 2 and MPC

Performance Metric	**Baseline 1**	**Baseline 2**	**MPC**
Power consumption	Poor	Ok	Good
Actuator Wear	Poor/Ok	Ok	Good
Disturbance Attenuation	Good	Ok	Good
Constraints Regulation	Good	Ok	Good

Chapter 6 Conclusion

6.1 Summary of Research Contributions

This thesis developed a modeling framework for multi-domain modeling of battery electric vehicle thermal and electrical subsystems. Furthermore, the modeling was used as the foundation for control integration to achieve temperature regulation of the cabin and battery pack, with consideration to power consumption. The outcomes are a two-fold impact for improving the performance of battery electric vehicles. The first is reduced power consumption of the thermal management system results in increased range of the vehicle. The second outcome is that effective thermal management of the battery pack within the optimal temperature range reduces degradation of the battery pack (affecting battery life) and improves performance (power limit).

This work focused on modeling three primary thermal systems; namely a transcritical vapor compression system, passenger cabin, and the battery pack. The modeling approaches capture the dominant system dynamics and the coupling within and between systems. The models are dynamic, modular and scalable. The dynamic behavior is essential for understanding transient systems. Vehicles experience frequently changing loads and disturbances which affects the operation of their electrical and thermal systems. The modularity and scalability enables rapid design and testing of vehicle systems and thermal management architectures. This work demonstrated these capabilities by building up two full systems: System 1) air-cooled cabin and air-cooled battery pack, and System 2) air –cooled cabin and liquid-cooled battery pack. Both systems were verified in open-loop simulation and System 1 was used for closed-loop design and analysis.

The open-loop simulations verified that the modeling methods capture the dominant dynamics of the systems individually and combined. Intuition was developed for system operation and dynamic variable interactions by testing various inputs and disturbances. It was demonstrated that the battery thermal regulation for System 1 is highly dependent on the cooling applied to the cabin. However, in System 2 the battery pack is less dependent on the cabin because both loads (cabin and battery pack) are on separate loops of the transcritical VCS. This required greater actuation of the compressor to provide cooling to both loads, but in return the battery pack temperature could be reduced independent of the cabin.

Closed-loop control was explored for thermal management of the cabin and battery pack, separately and then unified. The separate closed-loop control provided the understanding of the cabin system and battery system response with less complexity. The combined system was the before mentioned air-cooled cabin and air-cooled battery pack, where the air supplied to the battery pack is the cabin air. The controllers were designed for temperature regulation of the cabin and battery pack, and for minimal power consumption. The performance of two decentralized controllers and a centralized model predictive controller were evaluated with regards to the US06 drive cycle. This work showed that the MPC was able to regulate the cabin and battery pack within a desired region while consuming 21% less power than the lesser performing decentralized approach. The MPC was able to adjust the cabin temperature when necessary to meet the thermal management needs of the battery pack because it was not restricted to strict temperature set points. In the case that MPC is too costly, this work proposed a promising decentralized approach that uses the three available actuators (evaporator fan, compressor and valve) to control three degrees of freedom of the VCS cycle.

6.2 Future Work

Next steps include experimental validation of the models and controllers. Experimental data from a transcritical VCS should be obtained to validate the behaviors of the model. The baseline controllers for the transcritical VCS, without the battery pack, should also be validated with a physical system. Testing the entire controller of the combined system (VCS, cabin and battery pack) may be challenging without access to an entire vehicle, and should be done in stages. An intermediate step may be a hardware-in-the-loop configuration in which there is a physical transcritical vapor compression system with a simulated cabin, battery pack and other components.

Future modeling work should include integration of models of additional electrical components, such as motors, inverters, etc. These components also generate heat and have an efficiency associated with temperature. Additionally, the location of the electrical components should be used to capture thermal interactions between electrical components that are in close proximity. The battery models could be improved by capturing the degradation of the battery pack with time.

Finally, a variety of thermal management designs should be developed to compare their relative performances in open and closed-loop simulation. These designs should include air-cooled and liquid-cooled battery pack systems.

References

[1] "Climate Change Indicators in the United States." [Online]. Available: www.epa.gov/climate-indicators.

[2] D. L. Greene, H. H. Baker, and S. E. Plotkin, "Reducing Greenhouse Gas Emissions from U.S. Transportation," p. 122, 2011.

[3] "Regulations for Emissions form Vehicles and Engines." [Online]. Available: www.epa.gov/regulations-emissions-vehicles-and-engines.

[4] IEA International Energy Agency, "Global EV Outlook 2017: Two million and counting," *IEA Publ.*, pp. 1–71, 2017.

[5] "Refrigerant Transition and Environmental Impacts." [Online]. Available: www.epa.gov/mvac/refrigerant-transition-environmental-impacts.

[6] J. P. Rugh, A. Pesaran, and K. Smith, "Electric Vehicle Battery Thermal Issues and Thermal Management Techniques," *Altern. Refrig. Syst. Effic. Symp.*, pp. 1–40, 2011.

[7] T. Waldmann, M. Wilka, M. Kasper, M. Fleischhammer, and M. Wohlfahrt-Mehrens, "Temperature dependent ageing mechanisms in Lithium-ion batteries – A Post-Mortem study," *J. Power Sources*, vol. 262, pp. 129–135, Sep. 2014.

[8] J. Vetter *et al.*, "Ageing mechanisms in lithium-ion batteries," *J. Power Sources*, vol. 147, no. 1–2, pp. 269–281, Sep. 2005.

[9] B. Mebarki, B. Draoui, B. Allaou, L. Rahmani, and E. Benachour, "Impact of the air-conditioning system on the power consumption of an electric vehicle powered by lithium-ion battery," *Model. Simul. Eng.*, vol. 2013, 2013.

[10] W. Li, P. Stanula, P. Egede, S. Kara, and C. Herrmann, "Determining the Main Factors Influencing the Energy Consumption of Electric Vehicles in the Usage Phase," *Procedia CIRP*, vol. 48, pp. 352–357, 2016.

[11] M.-H. Kim, J. Pettersen, and C. W. Bullard, "Fundamental process and system design issues in CO2 vapor compression systems," *Prog. Energy Combust. Sci.*, vol. 30, no. 2, pp. 119–174, 2004.

[12] R. P. Mcenaney, D. E. Boewe, J. M. Yin, Y. C. Park, and C. W. Bullard, "Experimental

Comparison of Mobile A / C Systems When Operated With Transcritical CO2 Versus Conventional R134A," *Refrig. Air Cond.*, 1998.

[13] M. Y. Lee and D. Y. Lee, "Review on conventional air conditioning, alternative refrigerants, and CO2 heat pumps for vehicles," *Adv. Mech. Eng.*, vol. 2013, 2013.

[14] C. W. Bullard, J. M. Yin, P. S. Hrnjak, and A. Conditioning, "Transcritical Co 2 Mobile Heat Pump and A/C System Experimental and Model Results," *Elements*, pp. 1–10.

[15] Z. Qi, "Advances on air conditioning and heat pump system in electric vehicles - A review," *Renew. Sustain. Energy Rev.*, vol. 38, pp. 754–764, 2014.

[16] D. Boewe, J. Yin, Y. C. Park, C. W. Bullard, and P. S. Hrnjak, "The role of suction line heat exchanger in transcritical R744 Mobile A/C systems," *SAE Tech. Pap.*, no. 724, 1999.

[17] B. P. Rasmussen, "Dynamic modeling for vapor compression systems-Part I: Literature review," *HVAC R Res.*, vol. 18, no. 5, pp. 934–955, 2012.

[18] B. P. Rasmussen and A. G. Alleyne, "Control-Oriented Modeling of Transcritical Vapor Compression Systems," *ASME J. Dyn. Syst. Meas. Control*, vol. 126, no. March 2004, pp. 54–64, 2004.

[19] S. C. Kim, J. P. Won, and M. S. Kim, "Effects of operating parameters on the performance of a CO2 air conditioning system for vehicles," *Appl. Therm. Eng.*, vol. 29, no. 11, pp. 2408–2416, 2009.

[20] M. Ab and S. Karim, "Controller Development for an Automotive Ac-system using R744 as Refrigerant," pp. 477–485, 2008.

[21] S. . Liao, T. . Zhao, and A. Jakobsen, "A correlation of optimal heat rejection pressures in transcritical carbon dioxide cycles," *Appl. Therm. Eng.*, vol. 20, no. 9, pp. 831–841, 2000.

[22] Y. Hou, J. Ma, C. Liu, J. Cao, and X. Liu, "Experimental investigation on the influence of EEV opening on the performance of transcritical CO2 refrigeration system," *Appl. Therm. Eng.*, vol. 65, no. 1, pp. 51–56, 2014.

[23] C. Baek, J. Heo, J. Jung, H. Cho, and Y. Kim, "Optimal control of the gas-cooler pressure of a CO2 heat pump using EEV opening and outdoor fan speed in the cooling mode," *Int. J. Refrig.*, vol. 36, no. 4, 2013.

[24] H. Cho, C. Ryu, and Y. Kim, "Cooling performance of a variable speed CO2 cycle with an electronic expansion valve and internal heat exchanger," *Int. J. Refrig.*, vol. 30, no. 4,

pp. 664–671, Jun. 2007.

[25] K. Lockmahr, W. Baruschke, and A. Britsch-Laudwein, “Control System for R744 Refrigerant Circuits (German),” *ATZ Worldw.*, vol. 107, no. 9, pp. 796–799, 2005.

[26] “Thermosys.” [Online]. Available: http://www.thermosys.us/.

[27] J. M. Fasl, “Modeling and Control of Hybrid Vapor Compression Cycles,” 2013.

[28] Y. Hou, C. Liu, J. Ma, J. Cao, and S. Chen, “Mass flowrate characteristics of supercritical CO2 flowing through an electronic expansion valve,” *Int. J. Refrig.*, vol. 47, pp. 134–140, 2014.

[29] W. Li, “Simplified modeling analysis of mass flow characteristics in electronic expansion valve,” *Appl. Therm. Eng.*, vol. 53, no. 1, pp. 8–12, 2013.

[30] H. Pangborn, A. G. Alleyne, and N. Wu, “A comparison between finite volume and switched moving boundary approaches for dynamic vapor compression system modeling,” *Int. J. Refrig.*, vol. 53, pp. 101–114, 2015.

[31] B. P. Rasmussen and B. Shenoy, “Dynamic modeling for vapor compression systems-Part II: Simulation tutorial,” *HVAC R Res.*, vol. 18, no. 5, pp. 956–973, 2012.

[32] M. C. Keir and A. G. Alleyne, “Feedback structures for vapor compression cycle systems,” *Proc. Am. Control Conf.*, vol. 2, pp. 5052–5058, 2007.

[33] H. He, R. Xiong, H. Guo, and S. Li, “Comparison study on the battery models used for the energy management of batteries in electric vehicles,” *Energy Convers. Manag.*, vol. 64, pp. 113–121, 2012.

[34] H. E. Perez, J. B. Siegel, X. Lin, and A. G. Stefanopoulou, “Parameterization and Validation of an Integrated Electro-Thermal Cylindrical LFP Battery Model,” *ASME 2012 5th Annu. Dyn. Syst. Control Conf.*, pp. 1–10, 2012.

[35] L. Lam, “A Practical Circuit-based Model for State of Health Estimation of Li-ion Battery Cells in Electric Vehicles,” *IEEE*, p. 174, 2011.

[36] Q. Wang, B. Jiang, B. Li, and Y. Yan, “A critical review of thermal management models and solutions of lithium-ion batteries for the development of pure electric vehicles,” *Renewable and Sustainable Energy Reviews*. 2016.

[37] S. G. Garrow, C. T. Aksland, S. Sharma, and A. G. Alleyne, “Integrated Modeling for Battery Electric Vehicle Transcritical Thermal Management System,” in *American Control Conference*, 2018.

[38] S. Chacko and Y. M. Chung, “Thermal modelling of Li-ion polymer battery for electric vehicle drive cycles,” *J. Power Sources*, vol. 213, pp. 296–303, 2012.

[39] D. Marcos, F. J. Pino, C. Bordons, and J. J. Guerra, “The development and validation of a thermal model for the cabin of a vehicle,” *Appl. Therm. Eng.*, vol. 66, no. 1–2, pp. 646–656, 2014.

[40] S. Janarthanam, N. Burrows, and B. R. Boddakayala, “Factors Influencing Liquid over Air Cooling of High Voltage Battery Packs in an Electrified Vehicle,” 2017.

[41] K. Young, C. Wang, L. Y. Wang, and K. Strunz, *Electric Vehicle Integration into Modern Power Networks*. 2013.

[42] N. Jain, B. Li, M. Keir, B. Hencey, and A. Alleyne, “Decentralized feedback structures of a vapor compression cycle system,” *IEEE Trans. Control Syst. Technol.*, vol. 18, no. 1, pp. 185–193, 2010.

[43] R. Shah, B. P. Rasmussen, and A. G. Alleyne, “Application of a multivariable adaptive control strategy to automotive air conditioning systems,” *Int. J. Adapt. Control Signal Process.*, vol. 18, no. 2, pp. 199–221, 2004.

[44] W.-J. Zhang and C.-L. Zhang, “A correlation-free on-line optimal control method of heat rejection pressures in CO 2 transcritical systems,” *Int. J. Refrig.*, vol. 34, pp. 844–850, 2011.

[45] M. Morari and J. H. Lee, “Model predictive control: past, present and future,” *Comput. Chem. Eng.*, vol. 23, no. 4–5, pp. 667–682, May 1999.

[46] C. E. García, D. M. Prett, and M. Morari, “Model predictive control: Theory and practice—A survey,” *Automatica*, vol. 25, no. 3, pp. 335–348, May 1989.

[47] R. Kwadzogah, M. Zhou, S. Li, and S. Member, “Model Predictive Control for HVAC Systems - A Review,” *IEEE Int. Conf. Autom. Sci. Eng.*, pp. 442–447, 2013.

[48] T. Fischer, T. Kraus, C. Kirches, and F. Gauterin, “Nonlinear Model Predictive Control of a Thermal Management System for Electrified Vehicles using FMI.”

[49] J. Lopez-Sanz *et al.*, “Thermal Management in Plug-In Hybrid Electric Vehicles: A Real-Time Nonlinear Model Predictive Control Implementation,” *IEEE Trans. Veh. Technol.*, 2017.

[50] H. Esen, T. Tashiro, D. Bernardini, and A. Bemporad, “Cabin Heat Thermal Management in Hybrid Vehicles using Model Predictive Control.”

[51] L. Ljung, “System identification toolbox,” *Matlab user’s Guid.*, vol. 1, p. 237, 2011.

[52] B. P. Rasmussen, A. G. Alleyne, and A. B. Musser, “Model-driven system identification of transcritical vapor compression systems,” *IEEE Trans. Control Syst. Technol.*, vol. 13, no. 3, pp. 444–451, 2005.

[53] J. Lofberg, *YALMIP: A Toolbox for Modeling and Optimization in MATLAB*. Taipei, Taiwan, 2004.

[54] EPA, “Dynamometer Drive Schedules _ Vehicle and Fuel Emissions Testing _ US EPA.pdf.” .

Appendix A Velocity to Current Conversion

A velocity profile is converted to a current drawn from the battery pack with a force balance on the vehicle. It is assumed that the voltage of the battery pack is approximately constant. This calculation was described in Section 3.3.1. The execution for this process in Matlab is provided.

A.1 Conversion Code

```
% Define velocity and acceleration profile
V = xlsread('US06', 'Sheet1', 'C:C');    % Read drive profile from excel [m/s]
alpha = diff(V);                         % Calculate acceleration


% Define driving average parameters
V       = V(2:end);                      % Remove time 0 data point
slope   = 0;                             % Define average slope [-]
Vw      = 0;                             % Define average wind speed [m/s]
R_tire = .007;                           % Define rolling resistance [-]
Cd      = .28;                           % Define drag coefficient [-]
Af      = 2.29;                          % Define vehicle frontal area [m^2]
M       = 1600;                          % Define vehicle mass [kg]
g       = 9.81;                          % Gravitational acceleration [m/s^2]
rho_a   = 1.2;                           % Air density (assumed const)[kg/m^3]
theta   = atand(slope);                  % Convert slope to degrees
V_rel   = (V-Vw);                        % Determine relative wind speed
eta     = .7;                            % Mechanical -electrical efficiency


% Calculate forces
SigF    = M*alpha;                       % Force due to acceleration [N]
Fr      = M*R_tire*g*cosd(theta);        % Force due to rolling resistance [N]
Fd      = 1/2*rho_a*Af*Cd*(V_rel).^2;    % Drag force [N]
Fg      = M*g*sind(theta);               % Gravitational force from slope [N]
Ft      = SigF+Fr+Fd+Fg;                 % Required traction force[N]


% Calculate traction power and current
```

```
Pt     = V*Ft/eta;                          % Traction power required [W]
V_pack = 370;                               % Assumed constant batt. voltage [V]
I      = Pt/V_pack;                         % Current profile [A]
```

Appendix B High-side Pressure Optimizer Code

The high-side pressure reference for Baseline controller 2 is adjusted at discrete times when the on-line optimizer is called. The derivation for this controller is described in Chapter 4. A PI-controller adjusts the valve opening to track the reference.

B.1 Optimizer Simulink Structure

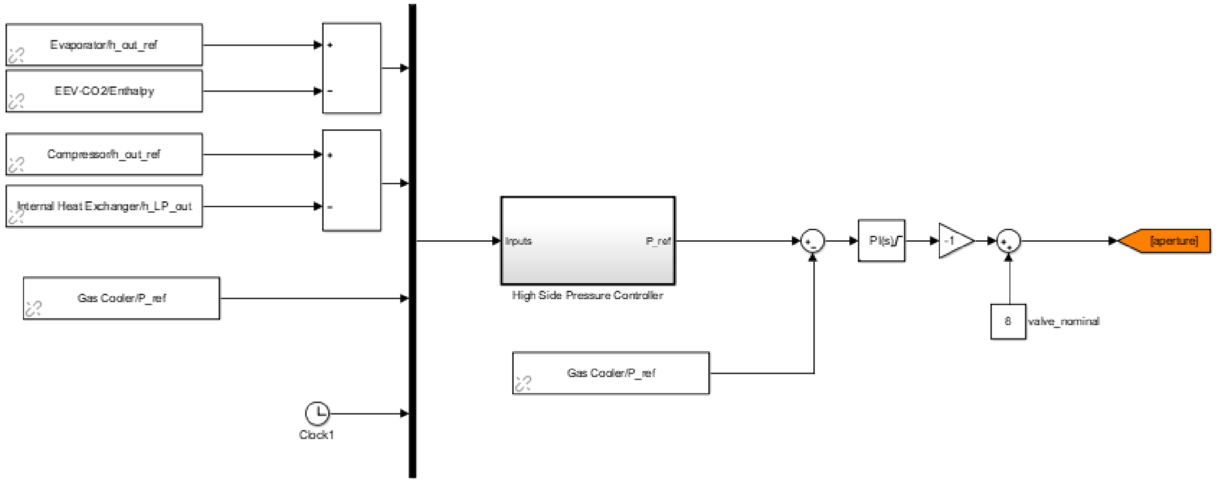

Figure B.1 Simulink diagram of high-side pressure reference optimizer and PI controller

B.2 Optimizer Call in Simulation

An Interpreted Matlab Function block calls a function ‘HPController.m’ that performs the calculation to adjust the high-side pressure reference.

Matlab Function: Controller.m

Output dimension: 1

Input dimension: 4

Sample Time: 300

The four inputs are the specific cooling capacity, specific work, gas cooler pressure and time respectively.

$$inputs = \begin{bmatrix} q_k & w_k & P_{gc,k} & t \end{bmatrix}^T \tag{C.1}$$

B.2.1 HPController.m Function

```
function [ p_ref ] = HPController( q_k, w_k, p_k, t )

persistent dPmax alpha p_k_0 q_k_0 w_k_0
if t == 0
    % Define maximum change in reference set point
    dPmax = 1000;
    % Define controller gain
    alpha = 3000;
    % Define initial conditions
    p_k_0 = 8480;
    q_k_0 = 42;
    w_k_0 = 41.3;
    % Set reference at t = 0 to initial condition
    p_ref = p_k_0;

else
    % Calculate the derivative of COP
    theta_k = (q_k-q_k_0)/q_k - (w_k-w_k_0)/w_k;
    % Calculate the change in pressure since the last time step
    dP = p_k - p_k_0;

    % Determine if COP and P are changing in same direction or opposite
    if sign(dP) == sign(theta_k)
        sn = 1;
    else
        sn = -1;
    end

    % Determine the updated pressure reference
    if abs(alpha*theta_k) > dPmax
```

```
        p_ref = p_k + sn*dPmax;
    else
        p_ref = p_k + sn*abs(alpha*theta_k);
    end

    % Set current states to [k-1] for next function call
    p_k_0 = p_k;
    q_k_0 = q_k;
    w_k_0 = w_k;
end
end
```

Appendix C Baseline Controller Tuning

C.1 High Side Pressure Controller Gain

As mentioned in Chapter 4, the impact of the valve opening on the high side pressure is coupled with the overall system refrigerant mass flow rate (Figure C.1). At lower mass flow rates, the compressor appears to dominate the high side pressure. In open-loop simulation with constant compressor speed, opening the valve increases the high side pressure. However, in closed-loop simulation there is interaction between the controllers. Recall the control design of Chapter 4, shown in Figure C.2. The controller interaction is most evident between the valve and compressor, because they both determine the refrigerant mass flow rate. In closed-loop simulation, the high side pressure decreases when the valve opens because the compressor speed is simultaneously adjusting. As the valve opens, the compressor speed decreases in response to the increased refrigerant mass flow rate (increased cabin cooling).

This closed-loop effect is shown in Figure C.3. The nominal value of the valve is 8%. When the controller gain is -1, the valve opens when the setpoint is lower than the measured pressure, and closes when the setpoint is higher than the measured pressure. When the controller gain is 0, the valve remains at 8% for the duration of the simulation. When the controller gain is 1, the valve closes when the setpoint is lower than the measured pressure, and opens when the setpoint is higher than the measured pressure. It can be seen that the controller with gain of -1, most closely tracks the pressure setpoint, and this is largely due to the fact that the compressor speed decreases in the closed loop system. At larger refrigerant mass flow rates, the valve dominates the high side pressure and the controller gain of -1 still applies to the closed loop system.

C.2 Baseline 2 High Side Pressure I-gain

Each Baseline controller was tuned to achieve desired performance objectives, including reference tracking, smoothness of actuation, and maintenance of superheat. Baseline 2 was sensitive to losing superheat and switching modes of operation. Recall that the evaporator is modeled with the moving-boundary approach. If certain controller gains were too high then Baseline 2 would cause the evaporator to switch from two zones (two-phase and superheat) to one zone (two phase) and then back. To avoid this behavior, the I-gain on the high side pressure controller was decreased by an order of magnitude.

Figure C.4 shows the results of the controller when the I-gain was 1E-5 compared to 1E-6 (as in Chapter 4). Figure C.5 shows a larger image of the gas cooler pressure. Figure C.6 shows a comparison of the power consumption of each. This one gain has a large impact on the system performance. The smaller I-gain results in less-aggressive actuation, smoother change in state variables, and less power consumption. A benefit of the larger gain is that it responds more to the changing high side pressure reference.

The last item to note is the spike in the thermal management power at about 200 seconds. This corresponds to the loss of superheat and seems to be a numerical issue caused by the moving-boundary method.

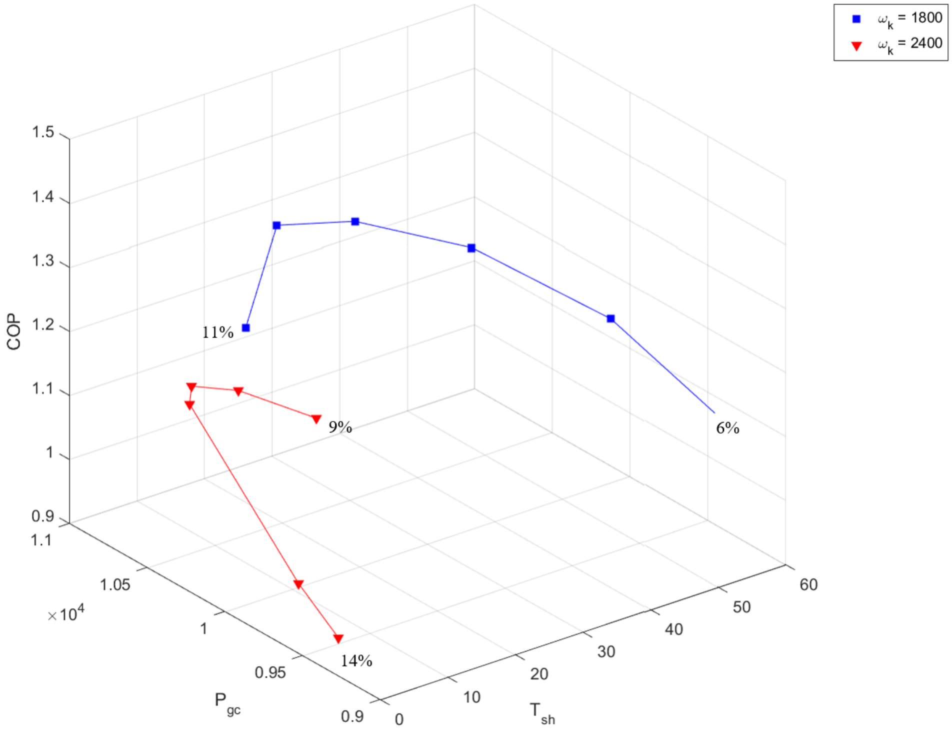

Figure C.1 Reprinted from Chapter 4. COP variance with respect to gas cooler pressure and evaporator superheat for two compressor speeds and varied valve opening

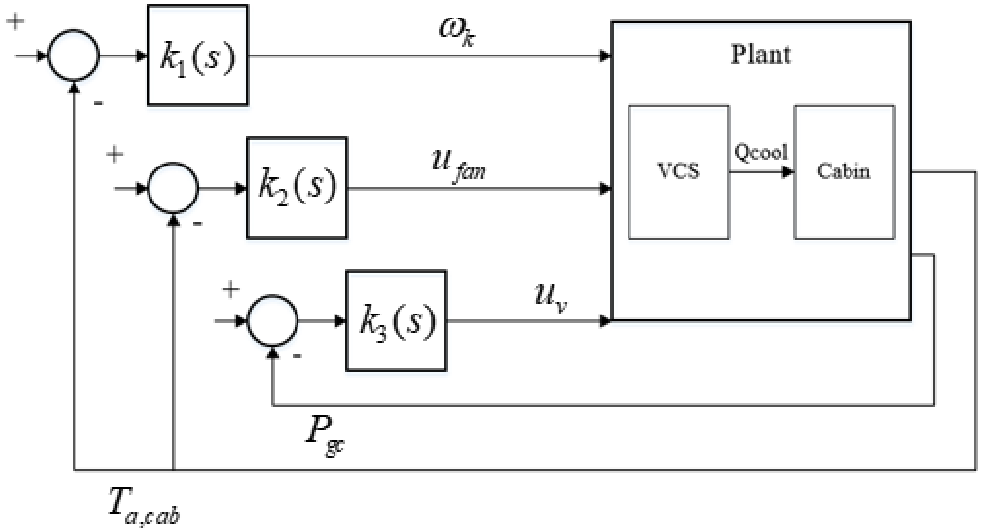

Figure C.2 Baseline 1 structure reprinted from Chapter 4. In closed loop form the compressor, fan and valve are simultaneously actuated in response to measured states

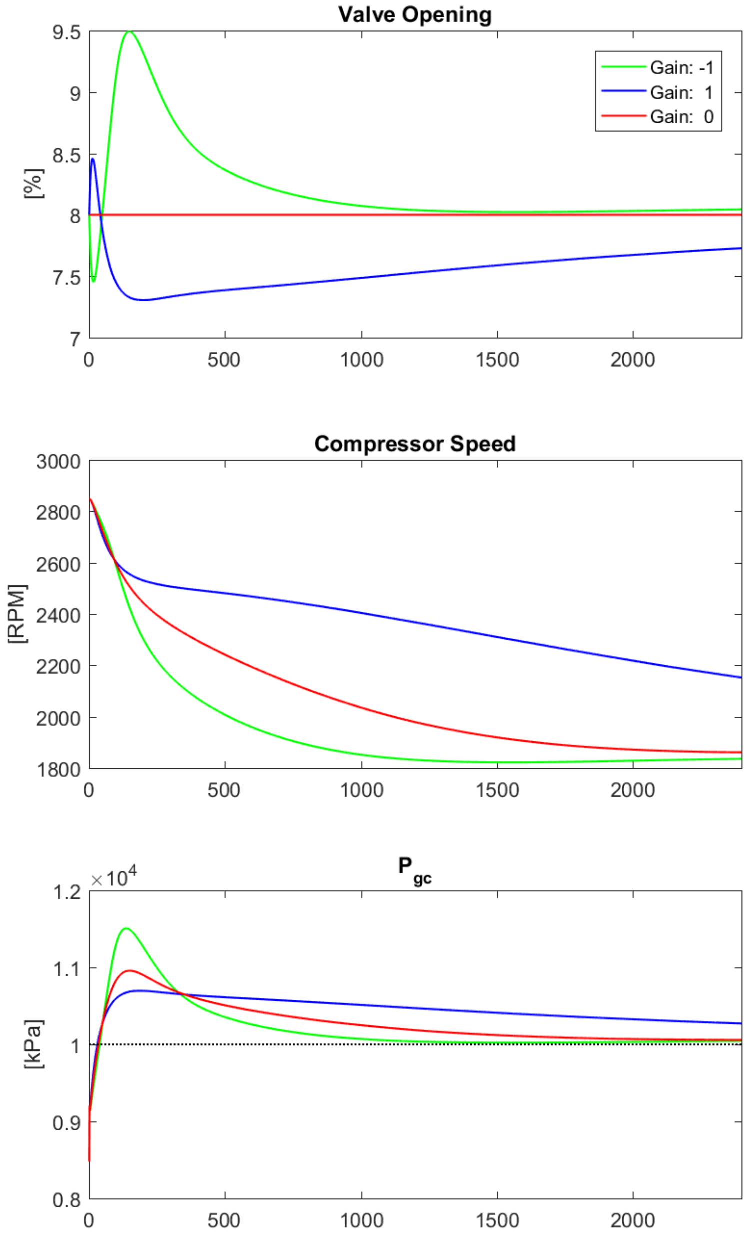

Figure C.3 High side pressure controller gain in closed-loop simulation

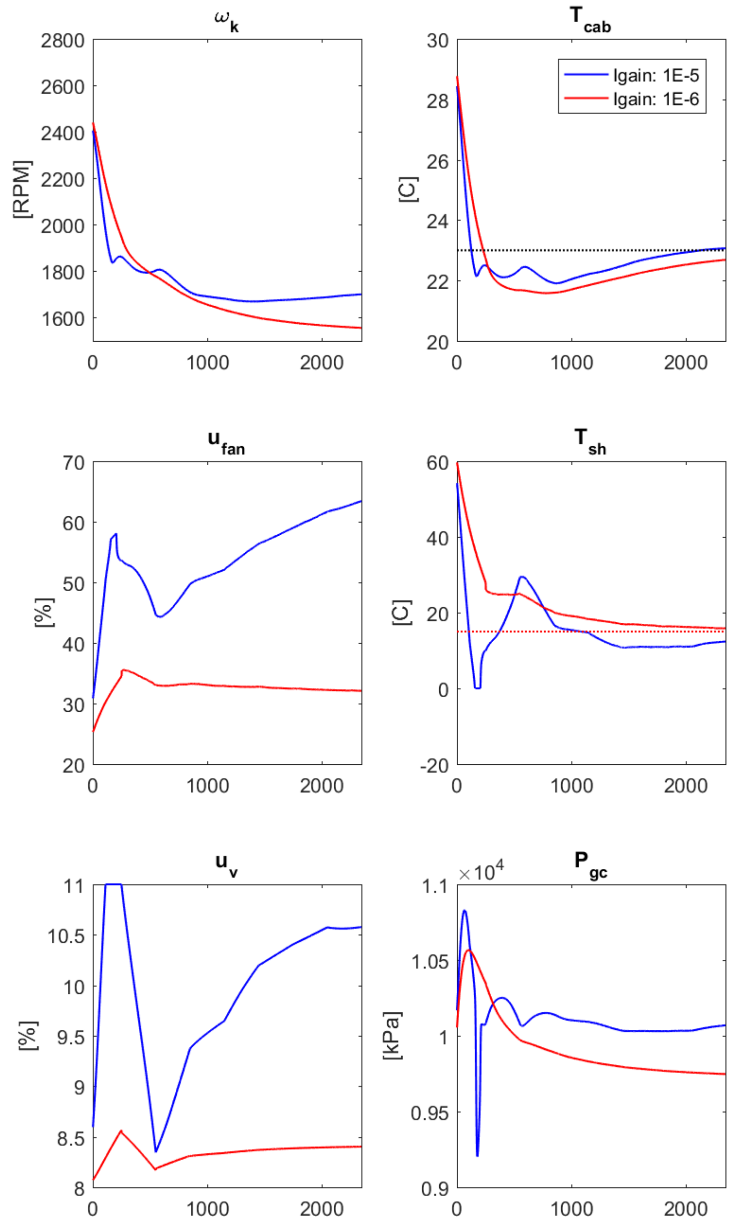

Figure C.4 Comparison of Baseline 2 system performance with different I-gain on high side pressure controller

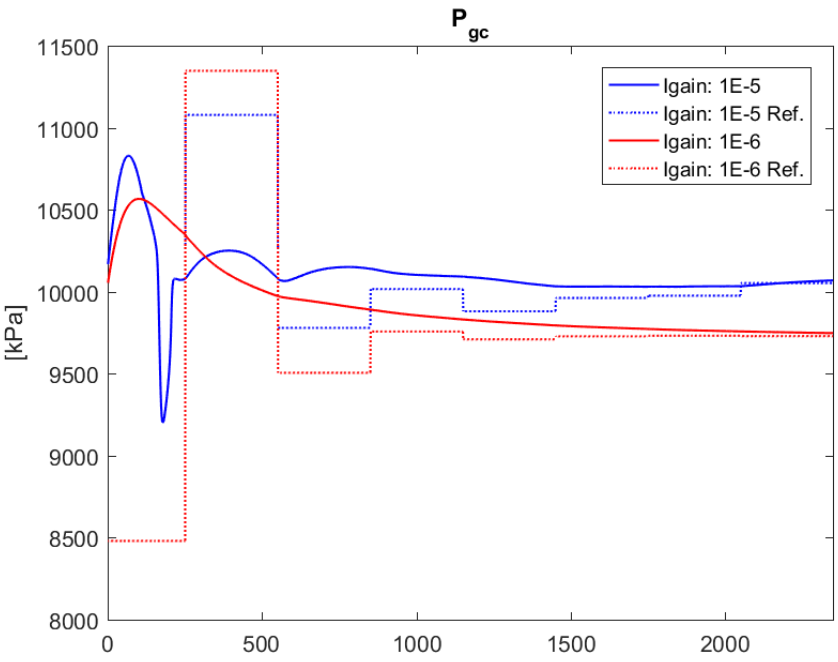

Figure C.5 Closer look at the high side pressure references and tracking of Baseline 2 with different I-gains

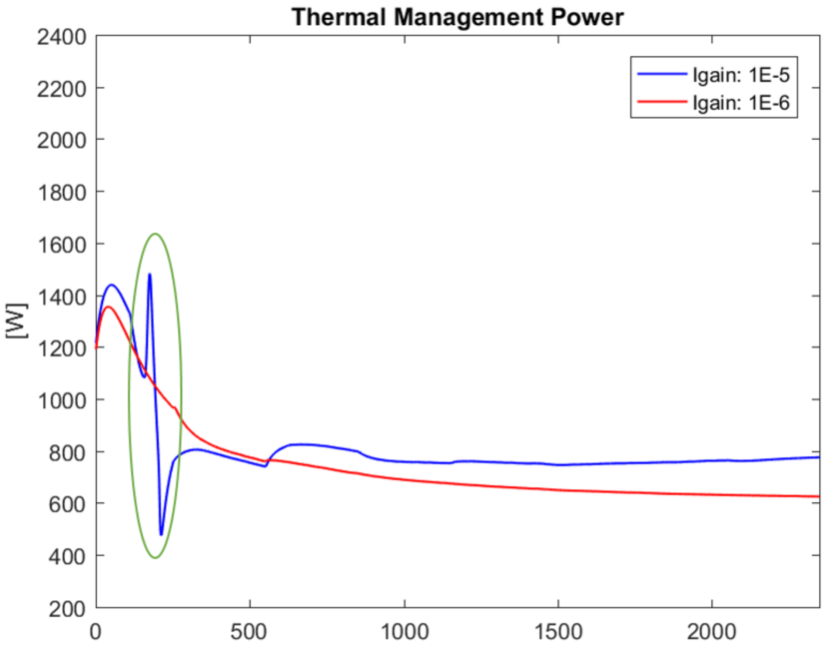

Figure C.6 Power consumption of Baseline 2 with different I-gains

Appendix D System Identification

The identification of linear models for the MPC was described in Chapter 5. The System Identification Toolbox of Matlab was used for the identification process. First, the nominal inputs were tested on the nonlinear system to collect the steady state values. Then a random binary sequence was generated using Matlab command ‘idinput’ and appended to a signal that perturbs each input individually. This method often improves the model fit by providing extra information of the system response from each input individually. The input/output data and sample time is then stroed in an object created with Matlab command ‘iddata’. An estimated state space model is generated with Matlab command ‘ssest’. This method is an iterative sub-space method, as opposed to ‘n4sid’ which is a non-iterative method. The code and Simulink diagrams for the transcritical VCS system identification is provided. The same process was applied to the battery pack and cabin.

D.1 System Identification for Transcritical VCS

D.1.1 System Identification Simulink Structure

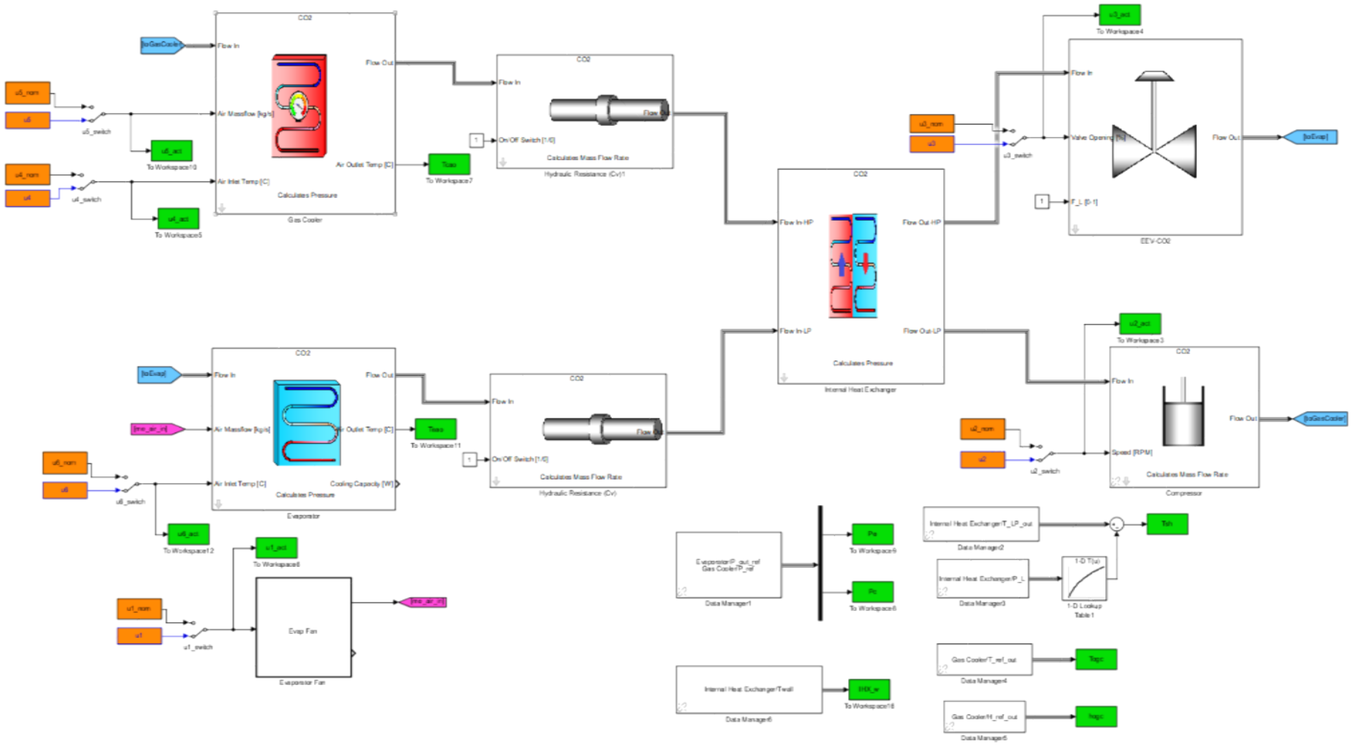

Figure D.1 Simulink diagram of nonlinear transcritical VCS

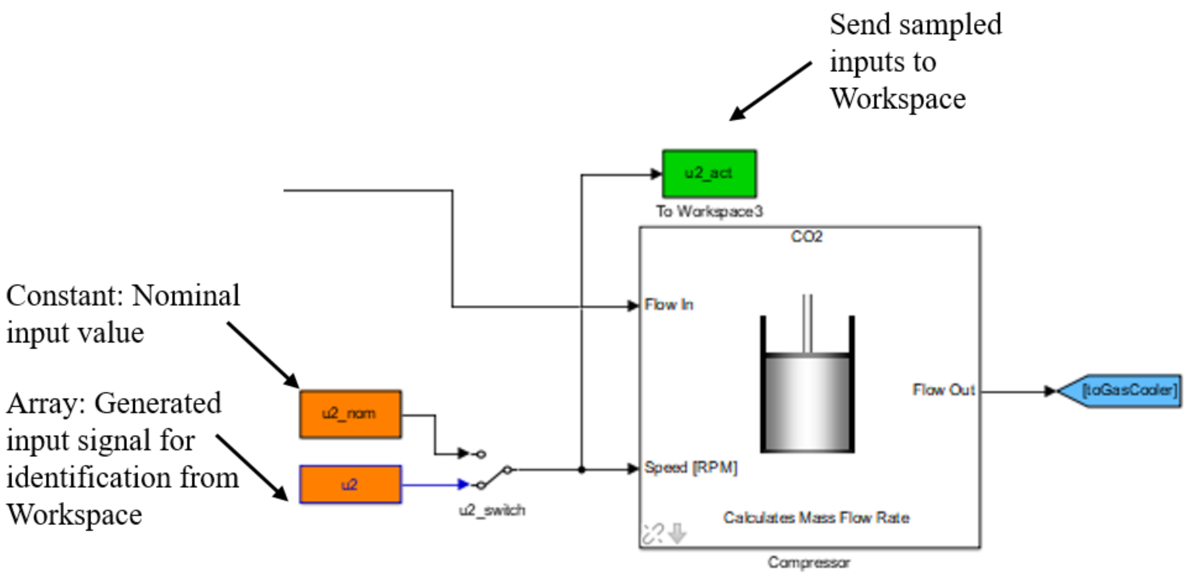

Figure D.2 Inputs into the actuators are switched between a constant nominal value and an array for the generated input signal for identification.

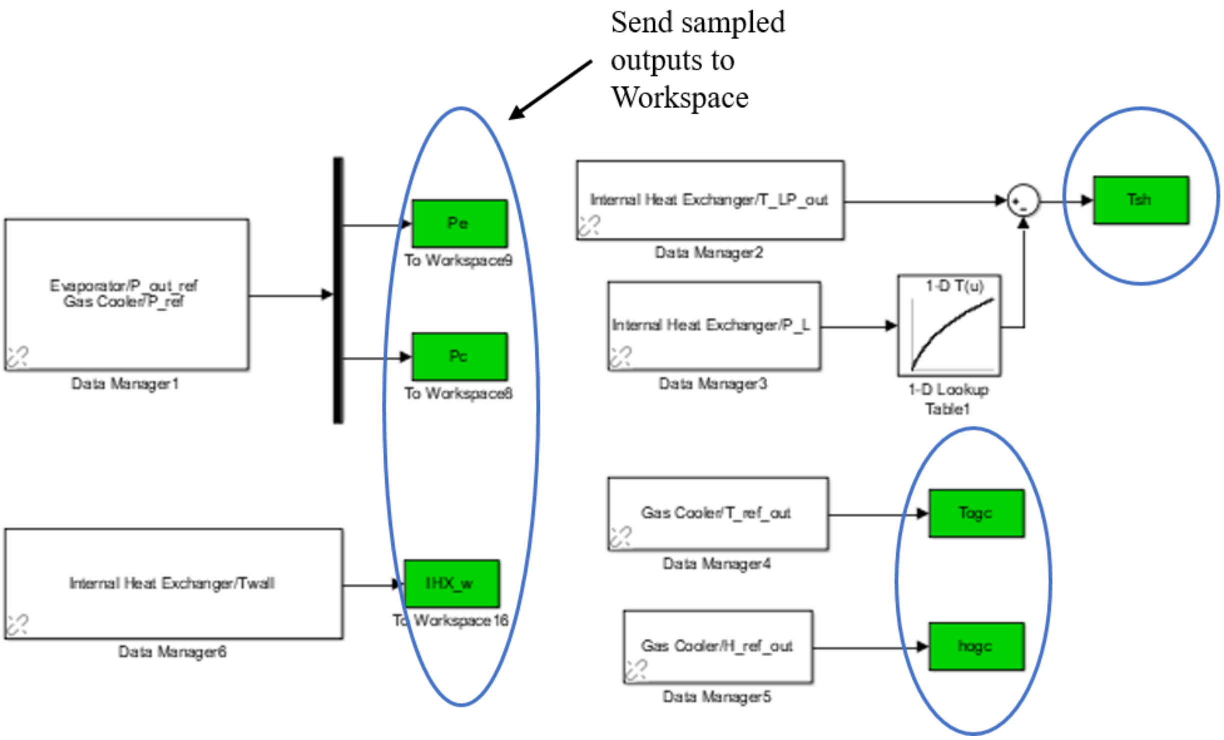

Figure D.3 System output are sampled every 'Ts' seconds and are sent to the workspace to be analyzed for the system identification

D.1.2 System Identification Script

```
%% VCS black box system ID
clear all; close all; clc;

filename = 'sysID_VCS_appendix';  % simulation file name
%% Determine steady state values for the nominal input values
% Set switches to constant inputs
set_param([filename, '/u1_switch'], 'sw', '1')
set_param([filename, '/u2_switch'], 'sw', '1')
set_param([filename, '/u3_switch'], 'sw', '1')
set_param([filename, '/u4_switch'], 'sw', '1')
set_param([filename, '/u5_switch'], 'sw', '1')
set_param([filename, '/u6_switch'], 'sw', '1')

%%%%%%%%%%%%%%%%%% Define nominal input values %%%%%%%%%%%%%%%%%%%%%
u1_nom = 50;        % Fan speed [0 100]
u2_nom = 1800;      % Compressor speed
u3_nom = 8;         % Valve aperture [0 100]
u4_nom = 35;        % Ambient temperature
u5_nom = .5;        % Gas cooler air mass flow rate
u6_nom = 30;        % Evaporator air inlet temperature
%%%%%%%%%%%%%%%%%%%%%%%%%%%%%%%%%%%%%%%%%%%%%%%%%%%%%%%%%%%%%%%%%%%%%%
time   = 1200;      % Simulation time-- long enough to achieve steady state
Ts     = 1;         % Sample time
% Clear time varying inputs
u1     = [0 0]; u2     = [0 0]; u3     = [0 0];
u4     = [0 0]; u5     = [0 0]; u6     = [0 0];
sim(filename)

% Collect steady state values for nominal input values
y1ss = mean(Teao(end-50:end)); % Average of last 50 seconds
y2ss = mean(Pe(end-50:end));
y3ss = mean(Pc(end-50:end));
y4ss = mean(IHX_w(end-50:end));
% Additional outputs that were tested
% y4ss = mean(Tcao(end-50:end));
% y4ss = mean(Tsh(end-50:end));
```

```
% Set switches to time varying inputs
set_param([filename, '/u1_switch'], 'sw', '0')
set_param([filename, '/u2_switch'], 'sw', '0')
set_param([filename, '/u3_switch'], 'sw', '0')
set_param([filename, '/u4_switch'], 'sw', '0')
set_param([filename, '/u5_switch'], 'sw', '0')
set_param([filename, '/u6_switch'], 'sw', '0')
%% Gernerate random input signal and collect data for system identification
% Generate random input sequence
Band  = 30;   % frequency to how often each input can change
Nu    = 6;    % number of inputs
dev   = .05;  % percent deviation from nominal value
ss    = 1200; % time at which steady state is achieved from ICs
Tt    = 600;  % amount of time to vary inputs
Ts    = 1;    % Sample time
nom_u = [u1_nom u2_nom u3_nom u4_nom u5_nom u6_nom];

%     All inputs perturbed by same percent deviation
u     = myIDinputs( Band, Nu, dev, ss, nom_u, Tt);

% OR Inputs are perturbed by different amounts
u1    = myIDinputs( Band, Nu, .05, ss, [1 1 u3_nom 1 u5_nom 1], Tt);
u2    = myIDinputs( Band, Nu, .15, ss, ...
    [u1_nom u2_nom 1 u4_nom u5_nom u6_nom], Tt);
u     = [u2(:,1) u2(:,2) u1(:,3) u2(:,4) u1(:,5) u2(:,6)];

figure(1)
plot(u)     % plot inputs

% Setup inputs to be sent to workspace for simulation
u1   = [(0:1:(size(u,1)-1))' u(:,1)];
u2   = [(0:1:(size(u,1)-1))' u(:,2)];
u3   = [(0:1:(size(u,1)-1))' u(:,3)];
u4   = [(0:1:(size(u,1)-1))' u(:,4)];
u5   = [(0:1:(size(u,1)-1))' u(:,5)];
u6   = [(0:1:(size(u,1)-1))' u(:,6)];
```

```
% Set simulation time
time = size(u,1);

% Run simulation and collect data
sim(filename)

%% Clean and store data
% Remove steady state value from outputs
y1 = Teao-y1ss;     % Evaporator outlet temperature in C
y2 = Pe-y2ss;       % Low side pressure in kPa
y3 = Pc-y3ss;       % High side pressure in kPa
% y4 = Tsh-y4ss;    % Evaporator refrigerant superheat
% y4 = Tcao-y4ss;   % Gas cooler air outlet temperature
y4 = IHX_w-y4ss;    % Wall temperature of internal heat exchanger

% Remove nominal value from input sequence
% Beneficial to collect the time data from the simulation if the sample
% time is not 1
u_act = [u1_act-u1_nom u2_act-u2_nom u3_act-u3_nom...
    u4_act-u4_nom u5_act-u5_nom u6_act-u6_nom];

% Create iddata object with output and input data
data  = iddata([y1(ss:end), y2(ss:end), y3(ss:end), y4(ss:end)],...
    u_act(ss:end,:), Ts);

%% Estimate state-space model and compare to the data
 % Initial state is zero, 'Focus' 'stability' enforces model stability
opt = ssestOptions('InitialState', 'zero', 'Focus', 'stability');
% Noise component is not estimated - 'DisturbanceModel', 'none'
sys = ssest(data, 2:12, 'Ts', Ts, 'DisturbanceModel', 'none', opt);

% Compare data to system for fit
figure(2)
compare(data, sys)
```

D.1.2.1 myIDinputs.m Function

```
function [u ] = myIDinputs( Band, Nu, dev, ss, nom_u, Tt)
%Create input perturbation every 'Band' seconds for 'Nu' number of inputs.
%The nominal value of inputs given by row vector 'nom_u'. The deviation
%from nominal defined as a decimal 'dev'. 'ss' refers to the time for the
%simulation to reach steady state.
Range = [-1 1]; % binary input signal limits
B = [0 1/Band]; % define Band

u_rand = idinput([Tt, Nu], 'rbs', B, Range); % generate RBS

for i = 1:Nu                                % scale to nominal values
    u_rand(:,i) = (dev*nom_u(i))*u_rand(:,i)+nom_u(i);
end
clearvars i

f = Nu*4*Band+ss;
u_choose = repmat(nom_u, [f, 1]);           % perturb each input individually
for i = 0:Nu-1
    u_choose(4*Band*i+ss:4*Band*i+ss+Band,i+1) = nom_u(i+1)*(1+dev);
    u_choose(4*Band*i+ss+2*Band:4*Band*i+ss+3*Band,i+1) = nom_u(i+1)*(1-dev);
end

% combine RBS and individually perturbed signals
u = [u_choose; u_rand];

end
```

Appendix E Model Predictive Control Code

E.1 MPC Design

The MPC optimizer is generated prior to the simulation. The following code loads the linearized models and defines the parameters that are required to generate the optimizer, i.e. actuator bounds, objective function weightings, prediction horizon, discrete system dimensions, and sample time. The function ‘controllerDesign.m’ generates the optimizer.

```
%% Create model predictive controller

% Load linearized state space models
% sys1 = battery
%        inputs: batt fan speed, inlet cooling temp, current
%        controllable: fan speed
%        output: mean surface temp, mean core temp
% sys2 = cabin
%        inputs: evap fan speed, supply air temp, ambient temp
%        controllable: fan speed
%        output:cabin air temperature
% sys3 = VCS
%        inputs: evap fan speed, compressor speed, aperture, Ambient
%        temp, gas cooler air flow rate, evap inlet temp
%        controllable: fan speed, compressor speed, aperture
%        output: evap air outlet temperature, Pe, Pgc, ihx wall
%        temp
load('Batt_sys'); Controller.sys1 = sys;
load('Cab_sys') ; Controller.sys2 = sys;
load('VCS_sys') ; Controller.sys3 = sys;

% Nominal inputs and states
% System 1
Controller.nomx1 = [30     30           ]'; % nominal state values
```

```
Controller.nomu1 = [30     26.5      100]'; % nominal input values

% System 2
Controller.nomx2 =  24.5;
Controller.nomu2 = [50     16      35]';

% System 3.
Controller.nomx3 = [14.95  3478.8  10014.1 44.87]';
Controller.nomu3 = [50     1800    8       35      .5     30]';

% Variable Dimensions
% System 1
Controller.Nu1 = 1;                         % number of inputs
Controller.Nx1 = size(Controller.sys1.A,2); % number of states
Controller.Ny1 = size(Controller.sys1.C,1); % number of outputs

% System 2
Controller.Nu2 = 1;
Controller.Nx2 = size(Controller.sys2.A,2);
Controller.Ny2 = size(Controller.sys2.C,1);

% System 3
Controller.Nu3 = 2;
Controller.Nx3 = size(Controller.sys3.A,2);
Controller.Ny3 = size(Controller.sys3.C,1);

Controller.Nd = 4;               % number of disturbances to combined system

% Weightings
Controller.Qbatt    = .001;      % battery temp tracking penalty
Controller.Qcab     = .1;        % cabin temp tracking penalty
Controller.R1       = .1;        % battery fan penalty
Controller.R2       = .1;        % cabin fan penalty
Controller.R3       = .005;      % compressor penalty
Controller.gamma1   = 5000;      % compressor change penalty
Controller.gamma2   = 5000;      % valve change penalty
Controller.gamma3   = 10000;     % cabin fan change penalty
```

```
Controller.gamma4   = 1000;      % battery fan change penalty
Controller.delta_T1 = .001;      % slack penalty - battery temperature
Controller.delta_T2 = 10  ;      % slack penalty - cabin temperature
Controller.delta_P  = 1e-2;      % slack penalty - pressure

% Control Bounds
Controller.umax = [100 100  3000   12  ]'; % fan, fan, compressor, aperture
Controller.umin = [ 0  20   1000   5   ]';
Controller.offset = [Controller.nomu1(1) Controller.nomu2(1)
Controller.nomu3(2) Controller.nomu3(3)]';

% Horizon
Controller.N = 120;          % prediction horizon

% Sample Time
Controller.Ts = 1;           % Discrete sample time

% Create Controller
Controller = controllerDesign(Controller);
```

E.1.1 controllerDesign.m Function

```
function [ Output ] = controllerDesign( Input )
yalmip('clear')
Output = Input;
% Create sdpvar's
x1 = sdpvar(repmat(Output.Nx1,1,Output.N+1),ones(1,Output.N+1));
x2 = sdpvar(repmat(Output.Nx2,1,Output.N+1),ones(1,Output.N+1));
x3 = sdpvar(repmat(Output.Nx3,1,Output.N+1),ones(1,Output.N+1));
u1 = sdpvar(repmat(Output.Nu1,1,Output.N+1),ones(1,Output.N+1));
u2 = sdpvar(repmat(Output.Nu2,1,Output.N+1),ones(1,Output.N+1));
u3 = sdpvar(repmat(Output.Nu3,1,Output.N+1),ones(1,Output.N+1));
r  = sdpvar(2                              ,                 1);
% slack on battery temp, cabin temp and high side pressure
s  = sdpvar(repmat(3,1,Output.N)           ,ones(1,Output.N)  );
% ambient temp, current disturbance, evap. inlet temp,
% gas cooler air mass flow rate
d  = sdpvar(repmat(Output.Nd,1,Output.N)   ,ones(1,Output.N)  );
```

```matlab
% Create objective function
obj = 0;
for k = 1: Output.N
    % Battery mean core temp reference
    obj = obj + Output.Qbatt*norm(r(1)-(Output.sys1.C(2,:)*x1{k+1}))^2;
    % Cabin temp reference
    obj = obj + Output.Qcab*norm(r(2)-(Output.sys2.C*x2{k+1}))^2;
    % Power penalties (normalized)
    obj = obj + Output.R1*norm((u1{k+1}+Output.offset(1))...
        /Output.umax(1))^2;
    obj = obj + Output.R2*norm((u2{k+1}+Output.offset(2))/...
        Output.umax(2))^2;
    obj = obj + Output.R3*norm((u3{k+1}(1)+Output.offset(3))/...
        Output.umax(3))^2;
    % Slack variable penalties
    obj = obj + Output.delta_T1*norm(s{k}(1))^2;
    obj = obj + Output.delta_P*norm(s{k}(2))^2;
    obj = obj + Output.delta_T2*norm(s{k}(3))^2;
    % Rate of actuator change penalties
    obj = obj + Output.gamma1*norm((u3{k+1}(1)-u3{k}(1))/...
        (Output.umax(3)-Output.umin(3)))^2;
    obj = obj + Output.gamma2*norm((u3{k+1}(2)-u3{k}(2))/...
        (Output.umax(4)-Output.umin(4)))^2;
    obj = obj + Output.gamma3*norm((u2{k+1}-u2{k})/...
        (Output.umax(2)-Output.umin(2)))^2;
    obj = obj + Output.gamma4*norm((u1{k+1}-u1{k})/...
        (Output.umax(1)-Output.umin(1)))^2;
end

% Create constraints
constraints = [];
for k= 1: Output.N
    % System dynamics
    constraints = [ constraints, x1{k+1}  == Output.sys1.A*x1{k}+...
        Output.sys1.B*[u1{k+1}; Output.sys2.C*x2{k};       d{k}(2)]];
```

```
    constraints = [ constraints, x2{k+1}  == Output.sys2.A*x2{k}+...
        Output.sys2.B*[u2{k+1}; Output.sys3.C(1,:)*x3{k};  d{k}(1)]];
    constraints = [ constraints, x3{k+1}  == Output.sys3.A*x3{k}+...
        Output.sys3.B*[u2{k+1}; u3{k+1}; d{k}(1); d{k}(4); d{k}(3)]];
    % Constrain inputs
    constraints = [ constraints, Output.umin(1)   <=...
        u1{k+1} + Output.nomu1(1)       <= Output.umax(1)  ];
    constraints = [ constraints, Output.umin(2)   <=...
        u2{k+1} + Output.nomu2(1)       <= Output.umax(2)  ];
    constraints = [ constraints, Output.umin(3:4) <=...
        u3{k+1} + Output.nomu3(2:3)     <= Output.umax(3:4)];
    % Constrain battery temp, high side pressure and cabin temperature
    constraints = [ constraints, Output.sys1.C(2,:)*x1{k+1} + ...
        Output.nomx1(2) <= 35   +s{k}(1)];
    constraints = [ constraints, 9000-s{k}(2) <= ...
        Output.sys3.C(3,:)*x3{k+1} + Output.nomx3(3) <= 12000+s{k}(2)];
    constraints = [ constraints, 21  -s{k}(3) <= ...
        Output.sys2.C     *x2{k+1} + Output.nomx2(1) <= 24.5   +s{k}(3)];
end
% Create optimizer
opts = sdpsettings('solver','quadprog'); % Solve with Quadprog
Output.Controller = optimizer(constraints,obj, opts,{x1{1},x2{1},x3{1},...
    u1{1},u2{1},u3{1},r,d{:}},[x1,x2,x3,u1,u2,u3,s]);
end
```

E.1.2 MPC Weightings

The weightings for the Disturbance Preview Test of Section 5.4.1 are provided in Equation E.1 corresponding to the variables defined in Chapter 5 for the MPC formulation.

$$\begin{aligned}
q_1 &= 1E-01 \\
q_2 &= 1E-03 \\
r_1 &= 1E-02 \\
r_2 &= 1E-01 \\
r_3 &= 1E-03 \\
\delta_1 &= 1E+00 \\
\delta_2 &= 1E-03 \\
\delta_3 &= 1E-02 \\
\gamma_1 &= 1E+05 \\
\gamma_2 &= 1E+03 \\
\gamma_3 &= 1E+05 \\
\gamma_4 &= 1E+04
\end{aligned} \tag{E.1}$$

The weightings for the Drive Schedule Test of Section 5.4.2 are provided in Equation E.2.

$$\begin{aligned}
q_1 &= 1E-01 \\
q_2 &= 1E-03 \\
r_1 &= 1E-01 \\
r_2 &= 1E-01 \\
r_3 &= 5E-03 \\
\delta_1 &= 1E+01 \\
\delta_2 &= 1E-03 \\
\delta_3 &= 1E-02 \\
\gamma_1 &= 1E+04 \\
\gamma_2 &= 1E+03 \\
\gamma_3 &= 5E+03 \\
\gamma_4 &= 5E+03
\end{aligned} \tag{E.2}$$

E.2 MPC Call in Simulation

Within the simulation, an Interpreted Matlab Function block calls a function ‘Controller.m’. This function organizes the inputs and then calls a function ‘controllerCall.m’ that calls the optimizer that was previously designed. The outputs are sorted in ‘Controller.m’ and passed out of the Interpreted Matlab Function block.

Matlab Function: Controller.m

Output dimension: 4

Input dimension: 10+4*N_p

Sample Time: 1

Six inputs are reshaped into a vector of dimension 10+4*N_p. Inputs 1-3 are the current states of the battery pack, cabin and transcritical VCS, respectively. Input 4 is the temperature references for the battery pack and cabin. Input 5 is the disturbances at the current time and at every sample time for one prediction horizon into the future. Input 6 is the time.

$$\begin{aligned} inputs = \Bigg[& \left\{ \left[T_{surf}^{mean} \quad T_{c}^{mean} \right]^T \right\} \quad \left\{ \left[T_{a,cab} \right] \right\} \quad \left\{ \left[T_{e,ao} \quad P_e \quad P_{gc} \quad T_{w,IHX} \right]^T \right\} \\ & \left\{ \left[T_{batt}^{ref} \quad T_{a,cab}^{ref} \right] \right\} \quad \left\{ \begin{bmatrix} d_{1,k} & \cdots & d_{1,k+N_p} \\ d_{2,k} & \ddots & d_{2,k+N_p} \\ d_{3,k} & \ddots & d_{3,k+N_p} \\ d_{4,k} & \cdots & d_{4,k+N_p} \end{bmatrix} \right\} \quad \left\{ \left[t \right] \right\} \Bigg] \end{aligned} \tag{E.3}$$

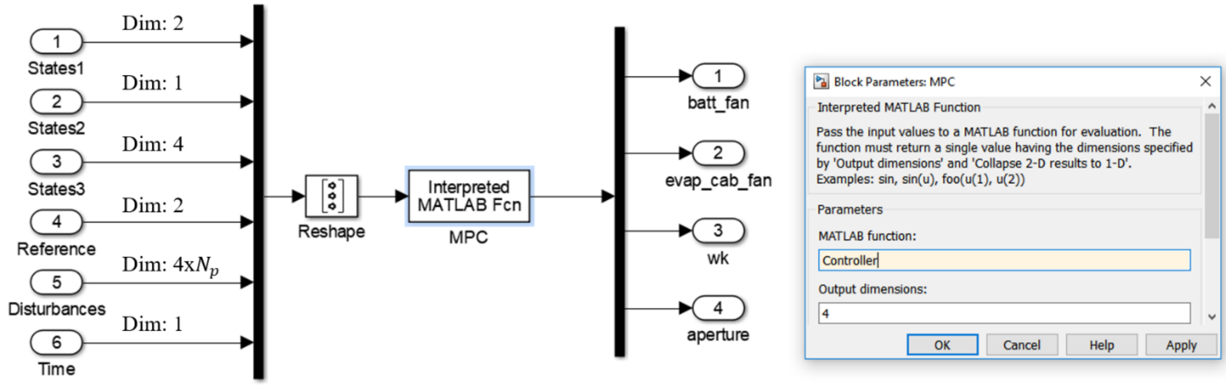

Block Parameters: MPC

Interpreted MATLAB Function

Pass the input values to a MATLAB function for evaluation. The function must return a single value having the dimensions specified by 'Output dimensions' and 'Collapse 2-D results to 1-D'.
Examples: sin, sin(u), foo(u(1), u(2))

Parameters

MATLAB function: Controller

Output dimensions: 4

Figure E.1 Interpreted Matlab function calling function ‘Controller’ to execute the optimizer

E.2.1 Controller.m Function

```
function [ out ] = Controller( in )


% Make Controller a persistant variable so that is only has to be loaded
% once at the start of the simulation
```

```
persistent Controller

t=in(end);

% At time = 0 load in Controller from the workspace and set inputs to
% nominal value
if t==0
    Controller=evalin('base','Controller');

    Controller.u0_1     = 0;
    Controller.u0_2     = 0;
    Controller.u0_3     = zeros(2,1);
    out = [0; 0; zeros(2,1)];

% At designated time implement MPC
elseif t > 600
    % Sort the inputs into the function block into their appropriate
    % varaible
    Controller.x0_1     = inv(Controller.sys1.C)*in(1:2);
    Controller.x0_2     = in(3);
    Controller.x0_3     = inv(Controller.sys3.C)*in(4:7);
    Controller.r        = in(8:9);
    Controller.d0_1     = in(10:10+  Controller.N-1)';
    Controller.d0_2     = in(10+  Controller.N:10+2*Controller.N-1)';
    Controller.d0_3     = in(10+2*Controller.N:10+3*Controller.N-1)';
    Controller.d0_4     = in(10+3*Controller.N:10+4*Controller.N-1)';

    % Call the optimizer
    Controller = controllerCall(Controller);

    % Shift current inputs to index [k-1] for the next call of the
    % controller
    Controller.u0_1     = Controller.u1(2);
    Controller.u0_2     = Controller.u2(2);
    Controller.u0_3     = Controller.u3(:,2);

    % Set output of the function block
```

```
    out = [Controller.u1(2); Controller.u2(2); Controller.u3(:,2)];
else
    Controller.u0_1     = 0;
    Controller.u0_2     = 0;
    Controller.u0_3     = zeros(2,1);
    out = [0; 0; zeros(2,1)];
end
```

end

E.2.2 controllerCall.m Function

```
function [ Output ] = controllerCall( Input )

Output = Input;
% Place optimizer inputs into appropriate cells
Controller_in = {Output.x0_1};
Controller_in = [Controller_in,{Output.x0_2}];
Controller_in = [Controller_in,{Output.x0_3}];
Controller_in = [Controller_in,{Output.u0_1}];
Controller_in = [Controller_in,{Output.u0_2}];
Controller_in = [Controller_in,{Output.u0_3}];
Controller_in = [Controller_in,{Output.r}];
Controller_in = [Controller_in,mat2cell([Output.d0_1; Output.d0_2; ...
    Output.d0_3; Output.d0_4], Output.Nd, ones(Output.N,1))];

% Call MPC optimizer
Controller_out = Output.Controller{Controller_in};

% Convert optimizer outputs into matrices
Output.x1 = cell2mat(Controller_out(:,1:Output.N+1));
Output.x2 = cell2mat(Controller_out(Output.N+2:2*Output.N+2));
Output.x3 = cell2mat(Controller_out(:,2*Output.N+3:3*Output.N+3));
Output.u1 = cell2mat(Controller_out(3*Output.N+4:4*Output.N+4));
Output.u2 = cell2mat(Controller_out(4*Output.N+5:5*Output.N+5));
Output.u3 = cell2mat(Controller_out(:,5*Output.N+6:6*Output.N+6));
Output.s  = cell2mat(Controller_out(:,6*Output.N+7:7*Output.N+6));
end
```